



January 2018

# Modeled And Observed Dynamical Characteristics Of Convective Mass Transport

Mariusz Starzec

Follow this and additional works at: <https://commons.und.edu/theses>

---

## Recommended Citation

Starzec, Mariusz, "Modeled And Observed Dynamical Characteristics Of Convective Mass Transport" (2018). *Theses and Dissertations*. 2431.

<https://commons.und.edu/theses/2431>

This Dissertation is brought to you for free and open access by the Theses, Dissertations, and Senior Projects at UND Scholarly Commons. It has been accepted for inclusion in Theses and Dissertations by an authorized administrator of UND Scholarly Commons. For more information, please contact [zeinebyousif@library.und.edu](mailto:zeinebyousif@library.und.edu).

MODELED AND OBSERVED DYNAMICAL CHARACTERISTICS  
OF CONVECTIVE MASS TRANSPORT

by

Mariusz Starzec

Bachelor of Science, University of North Dakota, 2013

Master of Science, University of North Dakota, 2014

A Dissertation

Submitted to the Graduate Faculty

of the

University of North Dakota

in partial fulfillment of the requirements

for the degree of

Doctor of Philosophy

Grand Forks, North Dakota

December

2018

This dissertation, submitted by Mariusz Starzec in partial fulfillment of the requirements for the Degree of Doctor of Philosophy from the University of North Dakota, has been read by the Faculty Advisory Committee under whom the work has been done and is hereby approved.



\_\_\_\_\_  
Gretchen Mullendore



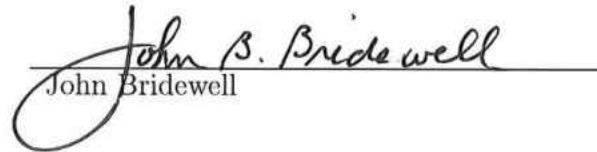
\_\_\_\_\_  
Mark Askelson



\_\_\_\_\_  
Aaron Kennedy

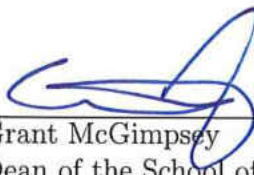


\_\_\_\_\_  
Paul Kucera



\_\_\_\_\_  
John Bridewell

This dissertation is being submitted by the appointed advisory committee as having met all of the requirements of the School of Graduate Studies at the University of North Dakota and is hereby approved.



\_\_\_\_\_  
Grant McGimpsey  
Dean of the School of Graduate Studies



\_\_\_\_\_  
DATE

PERMISSION

Title            Modeled and Observed Dynamical Characteristics of  
                    Convective Mass Transport

Department     Atmospheric Sciences

Degree          Doctor of Philosophy

In presenting this dissertation in partial fulfillment of the requirements for a graduate degree from the University of North Dakota, I agree that the library of this University shall make it freely available for inspection. I further agree that permission for extensive copying for scholarly purposes may be granted by the professor who supervised my dissertation work or, in her absence, by the Chairperson of the department or the dean of the School of Graduate Studies. It is understood that any copying or publication or other use of this dissertation or part thereof for financial gain shall not be allowed without my written permission. It is also understood that due recognition shall be given to me and to the University of North Dakota in any scholarly use which may be made of any material in my dissertation.

Mariusz Starzec  
December 13, 2018

## TABLE OF CONTENTS

LIST OF FIGURES . . . . .	<b>vi</b>
LIST OF TABLES . . . . .	<b>xii</b>
ACKNOWLEDGMENTS . . . . .	<b>xiii</b>
ABSTRACT . . . . .	<b>xv</b>
 CHAPTER	
1 INTRODUCTION . . . . .	<b>1</b>
2 USING RADAR REFLECTIVITY TO EVALUATE THE VERTICAL STRUCTURE OF FORECASTED CONVECTION . . . . .	<b>6</b>
2.1 Introduction . . . . .	6
2.2 Data . . . . .	9
2.2.1 Model Forecasts . . . . .	9
2.2.2 Radar Observations . . . . .	11
2.3 Evaluation of Model Forecasts . . . . .	15
2.3.1 Comparison Procedure . . . . .	15
2.3.2 Forecast Assessment . . . . .	17
2.4 Sensitivity to Simulated Reflectivity Calculation . . . . .	19
2.5 Summary and Conclusions . . . . .	24
3 STORM LABELING IN 3 DIMENSIONS (SL3D): A VOLUMETRIC RADAR ECHO AND DUAL-POLARIZATION UPDRAFT CLASSIFICATION ALGORITHM . . . . .	<b>39</b>
3.1 Introduction . . . . .	39
3.2 Radar Data . . . . .	42
3.3 SL3D algorithm . . . . .	44
3.3.1 Convection and Stratiform . . . . .	45
3.3.2 Anvil . . . . .	50
3.3.3 Convective Updraft . . . . .	51

3.4	Example SL3D Classifications and Convective Updraft Val- idation . . . . .	53
3.5	Comparisons of SL3D with Traditional Methods . . . . .	55
3.6	Importance of the Polarimetric Updraft Classification . . . . .	60
3.7	Limitations of the SL3D Algorithm . . . . .	61
3.8	Summary and Discussion . . . . .	63
4	<b>RETRIEVALS OF CONVECTIVE DETRAINMENT HEIGHTS USING GROUND- BASED RADAR OBSERVATIONS . . . . .</b>	<b>77</b>
4.1	Introduction . . . . .	77
4.2	Data . . . . .	80
4.2.1	Radar Composites . . . . .	80
4.2.2	Model Reanalysis . . . . .	81
4.3	Determining Radar-based LMD . . . . .	81
4.3.1	Anvil Proxy Method . . . . .	81
4.3.2	Radar Echo Stratification . . . . .	82
4.3.3	Classification of Storm Morphology . . . . .	83
4.3.4	Identification of Tropopause Height . . . . .	84
4.4	Results . . . . .	85
4.4.1	Applications of Anvil-based Methodology . . . . .	85
4.4.2	LMD Height Retrievals . . . . .	86
4.5	Discussion . . . . .	89
4.5.1	Limitations . . . . .	92
4.6	Summary and Conclusions . . . . .	94
5	<b>FRACTIONAL ENTRAINMENT RATE RETRIEVALS USING A BOUYANCY- BASED PLUME FRAMEWORK . . . . .</b>	<b>108</b>
5.1	Introduction . . . . .	108
5.2	Entraining Plume Model . . . . .	111
5.2.1	Mixed Temperature Retrieval . . . . .	112
5.2.2	Fractional Entrainment Rate . . . . .	114
5.2.3	Ideal Parcel Ascent . . . . .	116
5.3	Application of Entraining Model to Convection . . . . .	119
5.3.1	Weakly-forced Shallow Convection . . . . .	120
5.3.2	Deep Convective Cluster . . . . .	122
5.4	Comparison to Traditional Plume Theory . . . . .	124
5.5	Discussion . . . . .	126
5.6	Conclusions . . . . .	128
6	<b>SUMMARY AND CONCLUSIONS . . . . .</b>	<b>141</b>
	<b>REFERENCES . . . . .</b>	<b>146</b>

## LIST OF FIGURES

Figure	Page
1	The (blue) WRF model domains and (red) 126 km radar range from the KMBX and KBIS WSR-88D radars where the forecast analysis is performed. 28
2	The (left column) raw and (right column) quality controlled composite reflectivity fields as observed by the KBIS radar on a, b) 1 October, 2015 at 2305 UTC and c, d) 22 September, 2015 at 0417 UTC , respectively. . 29
3	The a) total number, b) area coverage, and c) mean object area of $\geq 45$ dBZ objects with height. The blue lines represent forecasts using the WSM6 microphysical scheme, red lines represent the Thompson microphysical scheme, and the black lines represent radar observations. The solid lines in panel (c) represent the mean object area and the dashed lines are the mean $\pm$ one standard deviation (Note that the dashed lines are not plotted when negative). . . . . 30
4	Contoured frequency by altitude diagrams (CFADs) of reflectivity within convective cores identified at the 2 km height for a) radar observations, b) WSM6 forecasts, and c) Thompson forecasts across the entire analysis period. The differences between CFADs are shown for d) WSM6 and radar observations and e) Thompson and radar observations, where the blue shading indicates under-representation by the model and red shading indicates over-representation by the model. The observed and simulated reflectivity values are binned in 5 dBZ bins. . . . . 31
5	The frequency of convective cores identified at 2 km height surpassing certain reflectivity thresholds with height for a) WSM6 forecasts, b) radar observations, and c) Thompson forecasts. The percentage of objects that surpass certain reflectivity thresholds normalized by the amount of convective cores identified at each height are shown for d) WSM6 forecasts, e) radar observations, and f) Thompson forecasts. . . . . 32

6	As in Figure 3, except using the K05 method. The dashed lines in panels a) and b) present the WRF method for reference (from Figure 3). . . . .	33
7	As in Figure 4, except using the K05 simulated reflectivity calculation. . . . .	34
8	As in Figure 5, except using the K05 simulated reflectivity calculation. . . . .	35
9	The Thompson scheme’s simulated reflectivity field on the native model grid using the (top) K05 method and (bottom) WRF method at a, d) 2 km, b ,e) 6 km, and c, f) 10 km for a 25-hour forecast valid on 2 June, 2015 at 01 UTC. Panels (g), (h), and (i) are the absolute difference between the K05 and WRF simulated reflectivity magnitudes in (a, d), (b, e), and (c, f) respectively, where red denotes higher reflectivity magnitudes in the K05 method and blue denotes higher reflectivity magnitudes in the WRF method. . . . .	36
10	A vertical cross-section of the Thompson scheme’s simulated reflectivity field on the native model grid using the a, b) K05 method and c, d) WRF method following the black line from a, c) point A to point B and b, d) point C to point D in Figure 9. Panels (e) and (f) are the absolute difference between the K05 and WRF simulated reflectivity magnitudes in (a, c) and (b, d), respectively, where red denotes higher reflectivity magnitudes in the K05 method and blue denotes higher reflectivity magnitudes in the WRF method. . . . .	37
11	The WSM6 scheme’s a) 2 km, b) 6 km, and c) 10 km simulated reflectivity field on the native model grid using the WRF method for a 25-hour forecast, valid on 2 June, 2015 at 01 UTC and the d) vertical cross-section of reflectivity from point A to B. . . . .	38
12	Maps of (a) $Z_H$ at 3 km altitude, (b) column-maximum $Z_H$ , and (c) SL3D classification for a supercell located in northeast Texas on 18 May 2013 at 0055 UTC. The thick lines labeled A–B on each map show the location of the vertical cross-sections in Fig. 13. . . . .	66
13	Vertical cross-sections of (a) $Z_H$ , (b) $Z_{DR}$ , and (c) $K_{DP}$ following the thick line in Fig. 12, from A (left) to B (right). The thick colored line at the base of each cross-section shows the corresponding SL3D classification. . . . .	67



14	Maps of (a) $Z_H$ at 3 km altitude, (b) column-maximum $Z_H$ , (c) the SL3D classification, and (d) dual-Doppler derived mean vertical velocity in the vertical column from a storm observed during the Severe Thunderstorm Electrification and Precipitation Study (STEPS) on 30 June 2000 at 0030 UTC. The black lines denotes the SL3D updraft classification using WER identification alone. . . . .	68
15	Maps of (a) $Z_H$ at 3 km altitude, (b) column-maximum $Z_H$ , (c) $Z_{DR}$ at 5 km altitude, (d) $K_{DP}$ at 5 km altitude, (e) the SL3D classification, and (f) maximum dual-Doppler derived vertical velocity on 06 June 2012 at 2230 UTC. The black lines denote the SL3D updraft classification using WER identification alone and the white lines denote the SL3D updraft classification using polarimetric variables alone. . . . .	69
16	Maps of (a) column-maximum $Z_H$ , (b) SL3D classification, (c) SHY classification and a vertical cross-section of $Z_H$ following the thick line labeled A–B for a collection of deep quasi-linear convective storms over Oklahoma and southeast Kansas on 14 May 2009 at 0125 UTC. The thick colored lines at the base of the cross-section show the corresponding SL3D and SHY classifications. . . . .	70
17	Maps of (a) column-maximum $Z_H$ , (b) $Z_H$ at 3 km altitude, (c) SL3D classification, and (d) SHY classification for a collection of supercell storms and an MCS over Oklahoma on 23 May 2011 at 2325 UTC. The white ellipse in (a) encloses weaker convection that is discussed in the text. . .	71
18	Maps of (a) column-maximum $Z_H$ , (b) SL3D classification, (c) SHY classification and vertical cross-sections of $Z_H$ following the thick lines labeled A–B and C–D for Tropical Storm Bill in southeast Texas and additional nearby precipitation in Arkansas, Louisiana, Oklahoma, and Texas on 17 June 2015 at 0000 UTC. The thick colored lines at the base of each cross-section show the corresponding SL3D and SHY classifications. . . . .	72
19	Maps of (a) column-maximum $Z_H$ , (b) SL3D classification, (c) SHY classification and a vertical cross-section of $Z_H$ following the thick line labeled A–B for an MCS located over Alabama, Florida, and Georgia on 24 July 2013 at 0000 UTC. The thick colored lines at the base of the cross-section show the corresponding SL3D and SHY classifications. . . . .	73
20	As in Figure 19, but for scattered weak convection and an MCS located primarily over New York and Pennsylvania on 25 June 2014 at 2300 UTC.	74

21	Maps of (a) column-maximum $Z_H$ , (b) $Z_{DR}$ at 5 km altitude, (c) $K_{DP}$ at 5 km altitude, (d) SL3D classification, (e) SL3D classification with $Z_{DR}$ -only updraft classification, and (f) SL3D classification with $K_{DP}$ -only updraft classification for an MCS located in northern Indiana and Ohio on 13 June 2013 at 0330 UTC. The thick lines on each map show the location of the vertical cross-sections in Fig. 22. . . . .	75
22	Vertical cross-sections of (a) $Z_H$ , (b) $Z_{DR}$ , and (c) $K_{DP}$ along the line in Fig. 21, from A (left) to B (right). The thick horizontal line in each cross-section represents the altitude of the environmental melting level and the thick colored line at the base of each cross-section shows the corresponding SL3D classification. . . . .	76
23	The four analysis regions demarcated by the $37^\circ\text{N}$ parallel and $87.5^\circ\text{W}$ meridian. . . . .	98
24	The a) composite reflectivity, b) SL3D classification, c) vertical cross-section of reflectivity following A to B, and d) horizontally integrated IWC for a supercell located in Nebraska on 13 July 2004 at 00 UTC. The yellow lines in b) denote identified precipitating objects, where the thick yellow lines are the objects that match the LMD retrieval criteria. The black line in c) and d) denotes the height of the radar-derived LMD using the anvil-proxy method and the red line denotes the tropopause height. . . . .	99
25	The boxplot distribution of a) retrieved LMD heights and b) tropopause-relative LMD heights across the entire analysis period for the months of May and July. The black asterisk is the mean, the horizontal red line is the median, top and bottom of the boxes are the 75th and 25th percentiles, respectively, the whiskers are three standard deviations from the mean, and the outliers are red crosses. . . . .	100
26	As in Figure 25, except categorized by morphology. . . . .	101
27	The tropopause-relative LMD height categorized by the four analysis regions: North-Central (NC), South-Central (SC), Northeast (NE), and Southeast (SE). The black asterisk is the mean, the horizontal red line is the median, top and bottom of the boxes are the 75th and 25th percentiles, respectively, the whiskers are three standard deviations from the mean, and the outliers are red crosses. . . . .	102

28	The tropopause-relative LMD height categorized by the months of a) May and b) July for the four analysis regions. The black asterisk is the mean, the horizontal red line is the median, top and bottom of the boxplots are the 75th and 25th percentiles, respectively, the whiskers are three standard deviations from the mean, and the outliers are red crosses. . . . .	103
29	As in Figure 28, except categorized by morphology. . . . .	104
30	As in Figure 28, except for the anvil-top height and not the LMD height.	105
31	As in Figure 29, except for the anvil-top heights and not the LMD heights.	106
32	The a) composite reflectivity, b) SL3D classification, and vertical cross-sections of reflectivity following c) A to B and d) C to D in panels (a) and (b) for an MCS located primarily over southeastern Iowa on 18 July 2006 at 01 UTC. The gradient fill in panel (a) denotes the tropopause height and the black line in panels (c) and (d) denotes the LMD height retrieved for the storm. . . . .	107
33	A illustrative overview of the fractional entrainment rate retrieval process, where a deep convective updraft is sampled by multiple Doppler radars with environmental profiles taken by a sounding. The blue line depicts a hypothetical observed vertical velocity while the orange line depicts a hypothetical idealized parcel ascending between levels. . . . .	131
34	The composite simulated reflectivity for a) several weak convective cells forecasted at 18 UTC July 2018 and b) a deep convective cluster forecasted at 21 UTC on August 2012. The red circles denote the locations of the environmental soundings. . . . .	132
35	A vertical cross-section of a) simulated reflectivity and b) vertical velocity across the analysis cell from point A to point B in Figure 34a. . . . .	133
36	The environmental sounding used for the shallow convective cell. The red and light green lines depict the environmental temperature and dew point, respectively. The black and dark green lines depict the ascent path of a surface-based parcel assuming irreversible and reversible ascent, respectively.	134

37	The a) vertical velocity, b) virtual potential temperature, and c) effective entrainment rate profiles for the shallow convective case. Blue lines depict the profile from the model, the black and dark green lines depict mixing parcels assuming irreversible and reversible ascent, respectively, and the red lines depict an ideal (non-mixing) irreversible parcel ascent. The stars in panel b) denote the mixed parcel virtual potential temperature. . . . .	135
38	A vertical cross-section of a) simulated reflectivity and b) vertical velocity across the analysis cell from point C to point D in Figure 34b. . . . .	136
39	As in Fig. 36 except for the deep convective cell. The cyan line denotes a reversible process with ice-phase processes included. . . . .	137
40	The a, c) vertical velocity, b, d) virtual potential temperature, and e) effective entrainment rate profiles for the deep convective case. Panels c) and d) are the same as panels a) and b), respectively, but are shown close-up to better illustrate the mixing parcel ascent paths. Blue lines depict the profile from the model, the black and cyan lines depict mixing parcels assuming irreversible liquid-only and reversible mixed-phase ascent, respectively, and the red lines depict an ideal (non-mixing) irreversible parcel ascent. The stars in b) and d) denote the mixed parcel virtual potential temperature. . . . .	138
41	The environmental (blue) $\theta_E$ and (red) $\theta_{ES}$ and (black dashed lines) the parcel ascent paths from the surface and top of the boundary layer for the shallow convective case. Parcels ascend assuming a constant entrainment rate until the parcels reach the storm's LMD height (denoted by a horizontal solid black line). . . . .	139
42	As in Figure 41 except for the deep convective case. . . . .	140

## LIST OF TABLES

Table		Page
1	The WRF model configuration used to generated forecasts over the region depicted in Figure 1. The cumulus parameterization scheme was only used for the 9- and 27-km domains. . . . .	27
2	The criteria required for classification into the five SL3D categories, where $Z_H$ is horizontally-polarized reflectivity, $Z_{Hmax}$ is the column-maximum $Z_H$ , and $Z_{Melt}$ is the height of the melting layer. . . . .	65
3	The total number of storms sampled (i.e, LMD retrievals performed) for each year of the analysis period categorized by region, month, and morphology. . . . .	97

## ACKNOWLEDGMENTS

First, and most of all, I would like to offer my sincerest gratitude to Dr. Gretchen Mullendore for all her expertise, guidance, and patience. I have learned more from her than I could ever imagine and she has been a great role model that was instrumental to my success. Gretchen has always given me excellent advice, both professional and personal, and has now become a great colleague and great friend. I would also like to thank my committee members, Dr. Mark Askelson, Dr. Aaron Kennedy, Dr. Paul Kucera, and Dr. John Bridewell for all their helpful suggestions, thought-provoking discussions, and feedback.

I am indebted to all the faculty and staff in the Atmospheric Sciences Department for providing me with invaluable knowledge and guidance throughout my entire student career. Similarly I would like to thank all my fellow students and friends for their support and friendship throughout the years.

I would also like to thank several organizations and collaborators for supporting this work, both financially and intellectually. The Developmental Testbed Center Visitor Project allowed for me to travel to the National Center for Atmospheric Research and work with all the scientists there and at the Research Applications Laboratory. Specifically, I would like to thank Tara Jensen for being a fantastic and gracious host. The Department of Energy Science Graduate Student Research Program made it possible for me to travel to Brookhaven National Laboratory and collaborate with the superb scientists in the Cloud Processes Group. I would like to specifically thank my mentor Dr. Michael Jensen for taking the time to work with me and for all the support he has showed me during and after the end

of the program. I would also like to offer my thanks to Dr. Cameron Homeyer for collaborating on several projects and being involved with a large portion of this work. The North Dakota Atmospheric Resource Board and Darin Langerud were very encouraging of this work and supported years of model simulations and model development. Finally, much of this work would have not been possible without support from the National Science Foundation (Grant No. AGS-1432930).

Last but certainly not least, I would like to thank my parents, Krystyna and Jozef, for continuing to support me unconditionally throughout my entire life. This accomplishment would not be possible without them, and any success I will ever achieve is due to their support, caring, and love.

Chapters 2 and 3 are copyrighted 2018 and 2017, respectively, by the American Meteorological Society (AMS). Permission to use figures, tables, and brief excerpts from this work in scientific and educational works is hereby granted provided that the source is acknowledged. Any use of material in this work that is determined to be fair use under Section 107 of the U.S. Copyright Act or that satisfies the conditions specified in Section 108 of the U.S. Copyright Act (17 USC 108) does not require the AMSs permission. Republication, systematic reproduction, posting in electronic form, such as on a website or in a searchable database, or other uses of this material, except as exempted by the above statement, requires written permission or a license from the AMS. All AMS journals and monograph publications are registered with the Copyright Clearance Center (<http://www.copyright.com>). Questions about permission to use materials for which AMS holds the copyright can also be directed to [permissions@ametsoc.org](mailto:permissions@ametsoc.org). Additional details are provided in the AMS Copyright Policy statement, available on the AMS website (<http://www.ametsoc.org/CopyrightInformation>).



## ABSTRACT

Convection can rapidly and efficiently transport polluted boundary layer air to the upper troposphere and lower stratosphere, thereby influencing the chemical composition and distribution of greenhouse gases in the atmosphere. Whether mass detrains into the upper troposphere or lower stratosphere has differing impacts on the radiative budget and hence, on climate. Currently, there have been only a few observing platforms capable of studying convective mass transport, which have significant limitations and are frequently restricted to field campaigns resulting in a small number of case studies. Outside of these case studies, little is known about the actual heights that convection detrains mass to or how much dilution a parcel rising in the updraft experiences due to processes such as entrainment. Entrainment not only reduces updraft buoyancy resulting in lower mass detrainment altitudes, but also dilutes updrafts that may be vertically transporting polluted boundary layer air, changing the chemistry of the detrained air aloft. To account for many of the limitations in observations, model simulations are commonly utilized; however, these models are unconstrained and need to correctly depict both the chemistry and dynamics. To improve our understanding of convective mass transport and help constrain model simulations, this study focuses on 1) identifying whether convection-allowing models can accurately depict the dynamics of mass transport, 2) building a large database of observed convective detrainment heights to determine the heights that convection detrains mass to, and 3) developing a methodology to retrieve observed fractional entrainment rates for deep convection that can be used to determine how much dilution is experienced by rising parcels.

These three objectives were researched as follows. First, biases within high-resolution convection-allowing model forecasts were identified with focus on the vertical structure and depth of deep moist convection. The object-based validation revealed that while the models performed well near the surface, there were large biases aloft. Overall, model forecasts generated too many convective elements that were individually too large and contained convection that reached the mid-troposphere twice as often as observations, leading to an over-estimation of the amount of mass being transported. Second, to determine the heights that convection actually detrains mass to, a large observational database of convective detrainment heights for the midlatitudes was built using ground-based radar observations. A newly developed radar echo stratification scheme was combined with high-resolution radar composites and an anvil-proxy methodology to retrieve the level of maximum detrainment (LMD) for convection across seven years for the months of May and July. Results showed that on average the LMD height was around 4.3 km below the tropopause, but can be as high as 2 km above the tropopause, with at least some mass transport occurring up to 6 km above the tropopause. May storms had a slightly higher mean tropopause-relative LMD height but July contained storms with the deepest transport. An analysis focusing on morphology found that quasi-isolated strong convection had higher LMD heights than mesoscale convective systems, with the highest LMD heights belonging to supercells. When subset by region, the southern regions of the United States were found to have lower mean LMD heights due to a large amount of diurnally-driven convection. Third and finally, to better understand why storms detrain mass to certain altitudes and to investigate the dilution of parcels with updrafts,

a buoyancy-based methodology was developed that builds upon and constrains plume theory with observations. The methodology works on the principles of comparing the buoyancy of an ideal parcel to that of a mixed parcel with attributes derived from observations of vertical velocity and environmental temperature and moisture. The method was applied to a case of weaker, mid-level convection and a case of a deep convective cluster. The deep convective cluster was found to have mean fractional entrainment rates of around  $0.26 \text{ km}^{-1}$ , which was about half of the mean rate found for the weaker, mid-level convective cell. The entrainment results also illustrated the importance of accounting for processes such as hydrometeor drag and the ice phase within the rising plume.

Overall, this study demonstrates the importance of including vertical information in analysis of both models and observations. The identified model biases in convective structure showcase where the convection-allowing models still need improvement and can be used to investigate where biases in precipitation fields originate. The LMD height retrievals depict the heights of mass detrainment and can be used to constrain chemical transport models in order to get more accurate approximations of transport heights for radiative and climate models. The statistical distribution of detrainment heights can also be used to estimate the amount of mass transport that occurs into the troposphere and stratosphere. The entrainment retrieval methodology can be applied to several observational datasets to retrieve fractional entrainment rates for convection of various morphologies and depths as long as vertical velocity and environmental temperature and moisture information is present. By incorporating observations, the entrainment rate retrievals can be used to constrain cumulus

parameterizations and theoretical parcel models. Furthermore, the LMD and detrainment envelope retrievals can be coupled with the entrainment retrieval methodology to determine how much dilution parcels experience before being detrained. Lastly, further study is required to investigate why supercells detrain mass to higher altitudes than other forms of convection.

## CHAPTER 1

### INTRODUCTION

Mass exchange between the upper troposphere and lower stratosphere (UTLS) changes the chemical composition, radiative properties, and distribution of greenhouse gases in the atmosphere, which has significant implication for climate studies (e.g., Ramaswamy et al., 1992; Holton et al., 1995; Stohl et al., 2003). The stratosphere contains dry, ozone-rich air while free tropospheric air is moist and contains relatively little ozone except in regions of biomass burning (Pan et al., 2010). Exchanges of mass between the two regions occurs in both directions (i.e., stratosphere-to-troposphere and troposphere-to-stratosphere). Downward transport of air from the stratosphere is a major contributor to the ozone concentrations in the free troposphere while upward transport of certain chemical species from the troposphere can lead to destruction of ozone (Fabian and Pruchniewicz, 1977). Since ozone is a potent greenhouse gas, the long lifetime of ozone in the UTLS (approximately one month; Liu et al., 1987) impacts the radiative balance.

Large-scale mass exchange mechanisms between the stratosphere and troposphere have been extensively studied (e.g., Holton et al., 1995; Plumb, 1996; Mote et al., 1996; Waugh, 1996; Stohl et al., 2003). In the tropics, the majority of transport occurs from the troposphere to the stratosphere. The Brewer-Dobson circulation is responsible for upwelling air from the tropical troposphere into the tropical stratosphere, horizontally transporting mass to the extratropical stratosphere, and downwelling air into the middle and high latitudes of the troposphere (Holton et al.,

1995). Nevertheless, transport from the stratosphere into the troposphere does occasionally occur in the tropics due to cyclones (Baray et al., 1999) and breaking Kelvin and Rossby waves (Fujiwara et al., 1998; Zachariasse et al., 2001). In the extratropics, large-scale processes primarily involve stratosphere-to-troposphere directed transport. The major source of mass transport into the extratropical troposphere occurs via isentropic transport from the tropical troposphere and diabatic descent from the upper stratosphere associated with the Brewer-Dobson circulation (Hintsa et al., 1998). Significant transport into the extratropics has also been observed in synoptic-scale features such tropical folds and cut-off lows (e.g., Ebel et al., 1991; Pan et al., 2010; Homeyer et al., 2011; Lin et al., 2012). These tropical folds and cut-off lows are associated with stratospheric intrusions that cause a large displacement of the tropopause, enabling a large exchange of mass (Stohl et al., 2003).

It is generally accepted that large-scale transport mechanisms are responsible for the majority of mass exchange, with small-scale features such as deep convection contributing substantially less overall mass. Nevertheless, deep moist convection is able to rapidly and efficiently transport boundary layer mass to the upper atmosphere. Convection can transport mass from the near surface to the UTLS in minutes to hours, as compared to days for extratropical cyclones and weeks or months for other turbulent diffusive processes (Dickerson et al., 1987; Sigmond and Siegmund, 2000). Unlike mass injected through large-scale ascent, convectively-transported mass has also been shown to be relatively undiluted by both in-situ aircraft measurements and model simulations (e.g., Dickerson et al., 1987; Pickering et al., 1988; Ström et al., 1999; Mullendore et al., 2005). Therefore, convective injections of polluted boundary layer air directly into the UTLS result in a significant chemical impact as boundary layer air has a markedly different chemical composition than the free troposphere (with the difference being amplified if mass is injected into the stratosphere).

Changes in chemical properties (and hence radiative and climatic effects) associated with deep convective transport are predominately driven by mechanisms of ozone destruction and production, as ozone is described as one of the most important greenhouse gases by the IPCC (2013). Ozone precursors (e.g., carbon monoxide, methane, volatile organic compounds) are found in large concentrations in the boundary layer but have relatively sparse concentrations in the free troposphere (Jiang et al., 2007); therefore, ozone has been heavily focused on by studies of convective transport as ozone precursors are readily transported by convection (e.g., Thompson et al., 1994; Barth et al., 2015; Huntrieser et al., 2016). Enhanced regions of ozone have also been found downwind of convection, with modeling and observational studies estimating the rate of ozone production anywhere between 3 to 17 ppbv day<sup>-1</sup> (Thompson et al., 1997; DeCaria et al., 2005; Cooper et al., 2006; Ott et al., 2007) and increases of up to 40 ppbv of ozone have been found within convective clouds (Winterrath et al., 1999). Global analysis performed by Lawrence et al. (2003) found that tropospheric ozone concentrations due to convection increased by 12%, and simulations performed by Jacob et al. (1993) show that up to 50% of ozone off the Northeastern coast of the United States results from post-convective reactions, indicating the importance of convective transport. Convective injection of water vapor into the UTLS has also been shown by in-situ measurements (Homeyer et al., 2014), which induces cooling at the UTLS and warming at the surface and acts as a catalyst for several heterogeneous reactions that promote ozone loss, which may be considerable if present in the lower stratosphere (e.g., Forster and Shine, 1999; Kirk-Davidoff et al., 1999; Drdla and Müller, 2012; Anderson et al., 2012).

Convection is theorized to transport majority of mass into the free troposphere; however, convection has been shown to penetrate the tropopause to directly inject mass into the stratosphere (e.g., Poulida et al., 1996; Wang, 2003; Hegglin et al.,

2004; Homeyer et al., 2014; Solomon et al., 2016). Whether transported mass is able to detrain directly into the stratosphere has implications on climate and health factors. In the troposphere, the presence of hydrogen and nitrogen oxide radicals in combination with volatile organic compounds transported by convection result in a net production of ozone. In the lower stratosphere, these hydrogen radicals (and other transported species) can result in a rapid destruction of ozone (e.g., Huntrieser et al., 2016); which has been shown to increase the amount of UV radiation reaching the surface (Anderson et al., 2012). Along with stratospheric ozone being transported downward along anvil edges, any ozone produced in the free troposphere can be transported downwards by large-scale subsidence and downward convective motions, where it acts as a lung irritant that can lead to acute lung inflammation, damage of the respiratory system, and has been linked with premature mortality (e.g., Silverman, 1979; Ghude et al., 2016). Furthermore, the residence times of transported species vary significantly between the stratosphere and troposphere; therefore, knowing the height of convective mass transport is crucial to determine what impacts convection has on the radiative and climatic balance.

Polluted air is transported upwards via the updraft until it dynamically detrains out of the updraft or mixes with environmental air to become neutrally buoyant. Overshooting tops have recently received a lot of attention with regards to convective transport due to the proximity of polluted air to pristine stratospheric environment. Nevertheless, the air within the overshooting top is negatively buoyant and relies solely on mixing processes (such as gravity wave breaking) to eject mass into UTLS; otherwise, even though the overshoot penetrates the tropopause it may not be ejecting a large amount mass into the stratosphere. The greatest amount of convective mass detrainment occurs in the convectively-generated anvil and thus cannot be neglected (e.g., Mullendore et al., 2013; Carletta et al., 2016). Air from the anvil can



also be directly injected into the lower stratosphere (e.g., Poulida et al., 1996; Hegglin et al., 2004; Mullendore et al., 2005) or can be mixed via processes such as gravity wave breaking aloft (e.g., Hassim and Lane, 2010). While there are several observing platforms that can be used to retrieve detrainment heights, such as aircraft, they have large spatial and/or temporal limitations that significantly limit our understanding of mass detrainment.

The purpose of this study is to improve our understanding of modeled and observed convective transport by (1) validating simulated convective structure, (2) building a large database of retrieved convective detrainment heights from radar observations, and (3) developing a methodology to retrieve deep convective entrainment rates from observations. Evaluating simulated convective structure provides insight into whether models are correctly depicting the dynamics of convective transport and helps identify regions of uncertainty in simulating mass transport (Chapter 2). A new radar echo stratification scheme is developed to distinguish between different parts of the storm in a dynamically and physically-oriented manner (Chapter 3). The radar echo stratification scheme is utilized to further help constrain model simulations and to get a quantitative understanding of observed convective mass detrainment heights. The convective detrainment heights are retrieved by building upon prior research and using several summers of composited radar observations across CONUS (Continental United States; Chapter 4). Lastly, one of the most important and least understood processes affecting the convective detrainment heights for deep convection is entrainment (which has to be parameterized in model simulations). Entrainment acts to dilute the chemical composition of a parcel and also reduces the rising parcels buoyancy. A method is developed that uses observations to constrain a modified plume model in order to retrieve fractional entrainment rates for deep convection (Chapter 5).

## CHAPTER 2

### USING RADAR REFLECTIVITY TO EVALUATE THE VERTICAL STRUCTURE OF FORECASTED CONVECTION

#### 2.1 Introduction

Model simulations are commonly used for both operational forecasting and to investigate processes in the atmosphere when inadequate observations exist or are hard to obtain, such as involving deep moist convection. In particular, the height, depth, and internal characteristics of deep moist convection are important storm factors for the operational and research communities. Storm height can be an indicator of convective strength, severity, and potential for lightning and hail generation (e.g., Held, 1978; Ushio et al., 2001; Donavon and Jungbluth, 2007; Pessi and Businger, 2009; Yang and King, 2010). The depth and internal structure also influences the generation location and magnitude of convectively-induced turbulence which impacts aviation (e.g., Lane et al., 2003; Barber et al., 2018). The internal storm dynamics and microphysics are closely tied together and affect attributes such as precipitation intensity, latent heat release, and mass transport (e.g., Adler and Mack, 1984; Houze, 1989; Mullendore et al., 2005; Powell and Houze, 2015). For example, modeling studies of convective mass transport rely on atmospheric chemical models to simulate tracer and chemical transport, reactions, and dilution. While atmospheric chemical models provide three-dimensional detail into transport processes, these models need to first properly simulate internal dynamics of deep convection in order to accurately disperse such tracers. Knowledge of the height of the upper-level storm detrainment, as dictated by storm

dynamics, is crucial as transported boundary layer air has different radiative and climatic effects depending on the altitude of mass transported (e.g., Dickerson et al., 1987; Barth et al., 2007; Anderson et al., 2012). Unfortunately, convection-allowing simulations are largely unconstrained with regards to storm height and internal characteristics; therefore, modeling studies typically have to subjectively compare the simulated convection to its observed counterpart to see whether the simulated storm depicts similar storm features. Furthermore, as regional convection-permitting climate model simulations and down-scaling of simulations become more utilized, it is increasingly important to correctly simulate the three-dimensional storm structure to accurately balance the atmospheric energy budget. Objective methods are needed to evaluate the three-dimensional structure of simulated storms.

A form of evaluation that accounts for spatial differences is necessary in high-resolution forecasts as traditional skill scores have limited usefulness when spatial anomalies exist between forecasts and observations (e.g., Mass et al., 2002). It is known that the exact timing and location of convective initiation is very difficult to predict due to the chaotic nature of the boundary layer. Consequently, using traditional point-to-point verification often leads to a subjectively good forecast being deemed objectively bad (e.g., Baldwin and Kain, 2006; Mittermaier, 2014). Therefore, to evaluate the representation of convection within convection-allowing simulations, the procedure should not be focused on precise location but should focus on evaluating convective characteristics, such as intensity, depth, and size. One methodology that does not emphasize precise locations and focuses more on such features is an object-based framework (e.g., Ebert and McBride, 2000; Davis et al., 2006; Ebert and Gallus, 2009). An advantage of object-based methods is that they focus on features within the analysis field rather than the entire field itself, meaning that regions of interest (i.e., objects) are defined based on the criteria specified by the user performing the

analysis. The object-based methodology enables a comparison of similar objects and their attributes in both model simulations and observations.

At convection-allowing scales, object-based methods have been used to investigate various parameters such as updraft helicity (Clark et al., 2012), brightness-temperature (Griffin et al., 2017), and convective initiation (Burghardt et al., 2014), but the predominant focus has been on the evaluation of precipitation fields (e.g., Davis et al., 2009; Ebert and Gallus, 2009; Gallus, 2010; Johnson and Wang, 2013; Johnson et al., 2013; Clark et al., 2014; Cai and Dumais, 2015). The general consensus from the aforementioned studies indicates that high-resolution model simulations commonly over-forecast the number of precipitating objects, precipitating objects are frequently too large horizontally, and precipitation tends to have a high intensity bias. While knowledge of biases in the simulated precipitation fields provides important insights for operational forecasting, it is also important to determine what processes may lead to those biases. Since the precipitation field is temporally averaged, potentially important features and details may be smoothed out. As a result of temporal smoothing, different forms of convection can produce a similar precipitation field while being dynamically and/or microphysically distinct from each other. In contrast, the simulated reflectivity field is not temporally averaged and provides an instantaneous representation of convective processes enabling a more direct comparison of storm features.

Comparisons of the simulated and observed reflectivity fields have been successfully used to investigate several model characteristics in the past; however, studies have evaluated the composite reflectivity field or the reflectivity field at one level, limiting the usage of vertical information (e.g., Kain et al., 2008; Schwartz et al., 2009; Jensen et al., 2010; Kain et al., 2010). Analyses that evaluated vertical convective structure have typically been limited to case studies or short periods of time (e.g.,

Rogers et al., 2007; Van Weverberg et al., 2011; Caine et al., 2013; Min et al., 2015); nevertheless, these studies have revealed important model biases. For example, Caine et al. (2013) analyzed several days of model simulations and found that simulations tended to have higher storm tops than observations. Similarly, Van Weverberg et al. (2011) found simulated reflectivity values that were too high in their simulations of supercell and multicell cases.

In this study, the observed reflectivity field at multiple heights is utilized to evaluate several months of daily convection-allowing forecasts over the Northern Great Plains region focusing on North Dakota. The purpose of this study is to demonstrate the usefulness of using three-dimensional reflectivity for model evaluation, investigate the accuracy of forecasted convective depth and internal vertical convective structure, and illustrate how convective biases change with height. Two different microphysical schemes are analyzed to investigate the variability generated in convective forecasts by switching schemes. Additionally, since simulated reflectivity calculations contain considerable uncertainty, a sensitivity study is performed by varying the simulated reflectivity calculation.

## **2.2 Data**

### **2.2.1 Model Forecasts**

Two Weather Research and Forecasting (WRF; Skamarock et al., 2008) Advanced Research WRF (ARW) 3-km v3.7.0 model configurations with differing microphysics are evaluated and shown in Table 1. The WRF forecasts were run operationally in support of the 2015 North Dakota Cloud Modification Project (NDCMP) to provide forecasters with daily guidance on convective morphology, intensity, and coverage. In summary, model microphysics varied between the WRF Single-Moment 6-Class

(WSM6; Hong and Lim, 2006) and Thompson (Thompson et al., 2004, 2008) schemes with all other physics held constant. The 3-km model domain where the analysis is performed is predominantly located over western North Dakota, embedded within a 9-km domain that is nested within a 27-km parent domain (Fig. 1). Forecasts had a model top of 50 hPa with 45 vertical levels on a stretched grid with an average spacing of  $\sim 215$  m in the boundary layer and  $\sim 525$  m in the free troposphere. Forecasts were initialized at 00 UTC starting 1 June 2015 through 30 September 2015 using the 40 km North American Mesoscale (NAM) model for initial and lateral boundary conditions. Forecasts were generated hourly out to 48 hours from initialization, but only forecasts hours 7 to 30 were analyzed (further discussed in section 2.3.1). The WSM6 and Thompson schemes were chosen because they are very commonly utilized single-moment microphysical schemes for both operational and research purposes, and many biases in these schemes (particularly precipitation) have been extensively investigated (such as by studies mentioned in section 3.1). The purpose of using two different microphysical schemes is not for an intercomparison of schemes, but to highlight the variability present in convective structure and depth within WRF simulations. The size of the 3-km domain and complexity of the microphysical schemes used was also limited by computational power and operational constraints set for forecast completion times.

Determining the reflectivity of hydrometeors in model forecasts is not trivial, especially for microphysical schemes that only retain single-moment (i.e., mass) information, as at a minimum, both hydrometeor concentrations and sizes are required. Both the WSM6 and Thompson schemes provide mixing ratios of cloud water, rain, cloud ice, snow, and graupel hydrometeors. Unlike the single-moment WSM6 scheme, the Thompson scheme is a hybrid scheme that also provides the number concentrations of cloud ice and rain. The simulated reflectivity is calculated internally within

WRF (i.e., the “do\_radar\_ref” option) as in Morrison et al. (2009) and is hereafter referred to as the WRF method. The radar reflectivity factor is determined in a microphysically-specific manner, meaning the method utilizes necessary constants and distributions directly from each microphysical scheme. The radar reflectivity factor is determined assuming Rayleigh scattering, which is appropriate for a 10-cm wavelength radar. In effort to account for some of the uncertainty in simulated reflectivity calculations, a second commonly used method is utilized and discussed in section 2.4 in order to determine the sensitivity to the simulated reflectivity calculation.

### 2.2.2 Radar Observations

Radar observations were taken by the 10-cm wavelength Next Generation Weather Radar (NEXRAD) Weather Surveillance Radar-1988 Doppler (WSR-88D) network (Crum and Alberty, 1993) radars located at Bismarck, ND (i.e., KBIS) and Minot, ND (i.e., KMBX). Radar data for each radar are initially transformed from the native polar coordinates to a uniform grid with a grid spacing of 0.01 degree ( $\sim 1$  km) in the horizontal and 1 km in the vertical, extending up from 2 km to 13 km in height above ground level (AGL; herein, all heights are in reference to AGL) using Radx software (Dixon, 2010). Data are mapped out to 126 km from each radar (red circles; Fig. 1), which is the furthest distance where the lowest elevation angle radar beam still samples the primary 2 km analysis height (further discussed in section 2.3.1) assuming standard atmospheric refraction. The relatively short maximum range of 126 km also limits potential issues with radar beam broadening at long distances and loses in detectability. Only radar data nearest to the top of each hour ( $\pm 10$  minutes) are used in order to match the hourly output of the model simulations. When data are present from both radars for a specific hour (and within 6 minutes

of each other), data are spatially composited using a simple distance-weighted mean. No temporal interpolation is performed when compositing radar observations.

The three-dimensional horizontally-polarized radar reflectivity data are used for evaluation of the model simulated radar reflectivity. Radar reflectivity is the measure of the backscattered power returned to the receiver by meteorological and non-meteorological targets and is primarily dependent on the concentration and cross-sectional area of the targets. The observed reflectivity field frequently contains many non-meteorological artifacts such as ground clutter and biological targets (i.e., birds and bugs) that can have magnitudes equaling or surpassing meteorological echo (e.g., Steiner and Smith, 2002; Lakshmanan et al., 2010). Large “blooms” of reflectivity frequently occur in the evening and overnight hours due to the presence of large amounts of bugs and enhanced ducting of the radar beam. These artifacts need to be removed prior to the analysis in order ensure that only active meteorological targets remain; therefore, radar data undergo simplistic quality control filtering to eliminate non-meteorological echo.

Dual-polarization data, in particular the cross-correlation coefficient ( $\rho_{HV}$ ) and differential reflectivity ( $Z_{DR}$ ), are utilized along with reflectivity to filter out non-meteorological echo. The  $\rho_{HV}$  parameter is a measure of the correlation or similarity between the returned power of the horizontally and vertically polarized pulses. Values of  $\rho_{HV}$  close to 1.0 typically indicate meteorological scatters with near uniform particle phases. Reductions in  $\rho_{HV}$  are often seen in mixed-phase regions, reaching values lower than 0.8 in regions of large hail and rain-hail mixtures. Similarly, the melting of snow hydrometers such as in stratiform regions of mesoscale convective systems (MCSs) can also reduce values of  $\rho_{HV}$  to  $< 0.7$ . Non-meteorological scatters typically have low  $\rho_{HV}$  values of  $< 0.7$ ; however, under certain conditions,  $\rho_{HV}$  values of non-meteorological scatters can be high and even approach 1.0 (Tang et al., 2014).  $Z_{DR}$  is the ratio



of the horizontally-polarized and vertically-polarized backscattered power from the radar pulses. Meteorological values of  $Z_{DR}$  near 0 dB typically indicate near spherical drops or tumbling hail. Values of  $Z_{DR} > 2.0$  dB indicate hydrometeors with a large horizontal cross-sectional area such as large drops, while negative values typically indicate vertically oriented ice crystals and conical graupel. More information on the polarimetric variables can be found in Doviak and Zrnić (1993), Ryzhkov et al. (2005b), and Kumjian (2013a,b,c).

The quality control steps performed follow many of the individual procedures outlined in Tang et al. (2014). Tang et al. (2014) filter radar echo by performing quality control procedures on radar bins along the radial. Since the radar data used in this study is gridded and only simplistic control procedures are needed, the quality control procedures are adjusted to work with the gridded dataset. Although the purpose of any quality control procedures is to remove as much non-meteorological echo as possible while retaining all meteorological echo, for this study more emphasis is placed on removing non-meteorological echo with reflectivity values that rival that of convection in order to prevent misidentification of convective cores (following section 2.3.1). Initially, as in Tang et al. (2014), all pixels with  $\rho_{HV} < 0.95$  are removed unless they are identified as being possible hail cores or regions of melting. Hail cores are identified as pixels containing reflectivity  $\geq 45$  dBZ and 18 dBZ echo tops  $> 8.0$  km. While Tang et al. (2014) correlated reductions in  $\rho_{HV}$  with temperature data to identify the melting layer, in this study the reductions in  $\rho_{HV}$  are correlated with enhanced reflectivity regions near the height of the typical melting level to avoid including additional uncertainty associated with temperature data from soundings (such as spatial and temporal representativeness). The melting level is identified as pixels containing  $\rho_{HV} < 0.7$  and reflectivity  $> 30$  dBZ in the lowest 5 km, where reflectivity data must also be present in at least three layers of the column stretching from the surface to

5 km. Following the  $\rho_{\text{HV}}$  filter, a  $Z_{\text{DR}}$  filtering procedure (not in Tang et al. (2014)) is included to remove any non-meteorological pixel clusters that remained. Any pixel containing very high values of  $Z_{\text{DR}} > 5$  dB coupled with low values of reflectivity  $< 10$  dBZ are removed as these high  $Z_{\text{DR}}$  signals are typically present from biological scatterers such as insects (e.g., Browning et al., 2011). Meteorological echoes with  $Z_{\text{DR}} > 5$  dB are largely found in regions of heavy rain or regions containing large drops, which will typically have reflectivity values  $> 10$  dBZ. Lastly, additional reflectivity filters are applied to the data. Columns are filtered if the rate of change of reflectivity in the lowest two heights is  $> 50$  dBZ or the reflectivity of the lowest level pixel is  $> 30$  dBZ with no echo above. These reflectivity filters enable the removal of any ground clutter with strong reflectivity signals. Once all filters are applied, a nearest neighborhood method is employed to filter out clutter that contains high  $\rho_{\text{HV}}$  and was not removed by the  $\rho_{\text{HV}}$  or reflectivity filters. For a given pixel containing reflectivity data, if more than half of the neighboring pixels have no or missing reflectivity data, the pixel is filtered and any remaining echoes comprised of less than three pixels (i.e.,  $3 \text{ km}^2$ ) are removed (similar to the speckle filter in Tang et al. (2014)). After the data has been filtered, any pixel-sized gaps created by the initial  $\rho_{\text{HV}}$  filter that are enclosed by meteorological echo are returned to their original reflectivity value. Examples applying the filters are shown for composite reflectivity observations taken by KBIS for typical ground clutter present during active convection (Fig. 2a, b) and during the overnight bloom (Fig. 2c, d). Other than the reflectivity threshold associated with the melting layer identification, the quality control procedures have low sensitivity to the exact reflectivity thresholds chosen. For the melting layer identification, reducing the reflectivity threshold below 30 dBZ results in retaining too much radar echo as regions that are not the melting level are identified as such and do not get removed

by the  $\rho_{\text{HV}}$  filter. Raising the threshold results in too much echo being removed, especially when the melting layer consists of a broad layer of lower reflectivity values.

Although there is uncertainty associated with the observed reflectivity, such as differences in calibration between the two radars, it is assumed this uncertainty is small and no corrections are made to observations. The largest uncertainties are likely aloft at the furthest distances away from the radars due to a combination of beam broadening, non-uniform beam filling, and potential attenuation in cores containing hail or losses in minimum signal detectability at range; however, these are partially mitigated by only using data within a 126 km range of the radars, limiting the magnitude of uncertainty.

## 2.3 Evaluation of Model Forecasts

### 2.3.1 Comparison Procedure

To enable a direct comparison, the radar and model data are evaluated on the same grid. Since the radar grid contains lower horizontal grid spacing as compared to the model grid (1-km vs 3-km, respectively), the radar domain may contain objects smaller than the grid spacing of the model. Since the model cannot generate objects smaller than 9 km<sup>2</sup>, it would unfairly penalize forecasts when such objects are present in observations; therefore, the radar data is interpolated to the model grid. Furthermore, while the radar has 1-km vertical grid spacing the model grid spacing is variable; therefore, the simulated reflectivity field is linearly interpolated in the vertical to match the radar vertical grid.

For an unbiased comparison, the model data is further constrained temporally and spatially. While the WRF model forecasts had no downtime, there were periods when either the KBIS, KMBX, or both radars were down. Forecasts were evaluated

hourly when data were present from either or both radars, starting at forecast valid hour 7 to hour 30 (i.e., 07 UTC to 07 UTC), giving the forecast a 7-hour spin-up time. Similarly, since the model domain covers more area than is observable by the radars, the forecasts are spatially constrained to the area with radar coverage at that time. Although the radar data is composited between two radars, the ‘cone of silence’ is still present at low levels and will influence the model evaluation. The cone of silence is the lack of coverage directly above the radar that results from the WSR-88D radars only being able to scan up to a maximum elevation angle of 19.5 degrees. The area covered by the cone of silence is filtered out to 30 km from both radar locations at each height for both the model data and radar data. The 30-km range is approximately the radius of the cone of silence at the highest evaluation height of 13 km using the elevation angle of 19.5 degrees.

In the subsequent analysis, forecasted objects are evaluated in two ways. First, observed and forecasted convective objects are identified at each height, ranging from 2 km to 13 km. Convective objects are defined as continuous reflectivity regions surpassing 45 dBZ (e.g., Caine et al., 2013). This first method treats each altitude level separately and there is no check on vertical extent of a particular high-reflectivity area. The second method includes vertical extent and focuses on convective cores. Convective cores are identified as  $\geq 45$  dBZ at the 2-km height; this area is then extended across all heights to form a column. Note that while the 1-km height is ideal due to the proximity of echo to the surface and frequent use by forecasters, the 2-km height is chosen to expand the area of analysis. The 1-km height significantly limits the horizontal area of analysis enough to produce detrimental effects on the analysis. For example, even small spatial offsets in forecasted convection could locate the convection outside the radar range, reducing the sample size.

### 2.3.2 Forecast Assessment

To assess the general performance of forecasts in terms of predictability of  $\geq 45$  dBZ objects, the number of objects, object areal coverage, and mean object sizes with height are aggregated across the entire forecast period and are presented in Figure 3. At the base 2-km height, both WSM6 and Thompson forecasts perform well when compared to observations, generating only 2.9% and 9.1% more objects, respectively (Fig. 3a). Above 2-km, the differences become much more pronounced. At the typical melting level height (i.e., 3 km), the reflectivity magnitudes are expected to increase due to the bright band. While the bias in over-producing objects increases to 23.4% for Thompson forecasts at the melting level, WSM6 forecasts under-predict object counts by 17.7%. Between 5 and 10 km, both schemes consistently contain almost double the number of observed objects, with Thompson forecasts over-predicting objects at all heights.

The profile of the total areal coverage of objects (Fig. 3b) follows a similar trend as Fig. 3a; however, the over-prediction of areal coverage is more pronounced than the number of objects. In general, other than the decrease in area at the melting level for WSM6 forecasts (discussed further in section 2.4), both forecasts considerably over-predict the area covered by objects through all heights. At the 2-km height, WSM6 and Thompson forecasted objects cover 91% and 51.7% more area than observations, respectively. This over-prediction of areal coverage is in-part due to more forecast objects, but also from individual objects being too large (Fig. 3c). For Thompson forecasts, both the over-prediction of object counts and larger mean object sizes contribute to the bias in areal coverage. For WSM6, the bias in areal coverage in the lower troposphere is primarily due to over-prediction of object sizes, as the number of objects is predicted well. In the upper troposphere, the WSM6 object sizes are consistent with observations (especially above 8 km), but the object counts are too

high. This indicates that the primary cause of the areal coverage bias transitions from object size to object count as one goes to higher altitudes.

To investigate the internal structure of convection, contoured frequency by altitude diagrams (CFADS; Yuter and Houze, 1995) are generated for the entire forecast period. CFADs of the reflectivity field with height are found by identifying the convective cores at 2-km height and mapping the area covered by the cores vertically; therefore, the reflectivity of each grid square with height within the column of the 2-km core is included. It is apparent from the CFADs that the forecasts contain a wider spread of reflectivity values within convective cores (Fig. 4). The WSM6 CFAD also contains a different slope in maximum frequencies than observations (Fig. 4a, b). The frequency of  $\geq 45$  dBZ reflectivity values within WSM6 convection remain relatively similar between 2 km and 8 km and does not decrease with height as in observations. Directly comparing the frequency distributions, WSM6 simulated convection is frequently too weak by 5 to 10 dBZ up to 31% of the time below 5 km; however, simulated convection is generally too intense between 5 and 8 km 26% of the time (Fig. 4c). WSM6 is missing the most intense (i.e.,  $> 55$  dBZ) convection. The Thompson CFAD slope and reflectivity distribution are more similar to observations but contain notably more spread than observations (Fig. 4a, d). The wider distribution is caused by Thompson forecasts containing more intense convection than observations throughout all heights (Fig. 4e). Thompson and WSM6 perform differently near the melting level, where WSM6 forecasts are frequently too weak by at least 10 dBZ 33% of the time and Thompson forecasts are too strong by at least 10 dBZ 26% of the time (Fig. 4c, e).

To gain additional insight, the likelihood of individual convective cores surpassing certain depths and intensities is analyzed (Fig. 5). Of all convective cores at 2 km, 20%, 35.7%, and 44.6% of cores retain reflectivity magnitudes above 45 dBZ

at 6 km and 3.3%, 5%, and 6.9% reach 10 km, for observations, WSM6, and Thompson, respectively. These results show that forecasts contain more cores that extend deeper into the troposphere than observations, with Thompson forecasts containing more than double the number of cores reaching 6 and 10 km. At the 2-km height, only 11.8% of observed cores contain reflectivity values surpassing 55 dBZ and 1.6% surpass 60 dBZ (Fig. 5b), while only a few cores surpassed 65 dBZ and none were observed above 70 dBZ. WSM6 has only 2.8% of cores reaching 55 dBZ, and no cores reach 60 dBZ, indicating the forecasted convective cores are too weak (Fig. 5a). Conversely, Thompson convective cores are overly intense and have 52.5% and 30.8% of cores reaching 55 and 60 dBZ, respectively, with a few cores even surpassing 75 dBZ (Fig. 5c). The same trends are visible throughout the vertical. To further highlight the intensity biases, the profiles are normalized by the number of identified cores ( $\geq 45$  dBZ objects) at each height and shown in Figure 5d-f. In total, while 4% of all observed cores surpass 55 dBZ at 10 km, none surpass 50 dBZ in WSM6 forecasts, and 2% of Thompson forecasted cores manage to surpass 65 dBZ at the same height (Fig. 5d-f). The highest reflectivity regions in Thompson extend far into the upper troposphere, while in WSM6 the intensity rapidly decreases with height. To summarize, while both microphysical schemes generate more convective cores with height, the strongest cores are too weak in WSM6 and too strong in Thompson.

## 2.4 Sensitivity to Simulated Reflectivity Calculation

Since there is a great deal of uncertainty in deriving the simulated reflectivity field, a second, commonly utilized method is used to determine the sensitivity of the results to reflectivity calculation. For the second method, the radar reflectivity factor is computed following the procedure outlined in (Koch et al., 2005, herein referred to K05), where the radar reflectivity factor is determined using fixed assumptions about the

distributions of hydrometeor size and shape for rain, snow, and graupel and primarily relies on their mixing ratios. These assumptions include using a fixed y-intercept and single-moment representation of hydrometeor distributions (even though the Thompson scheme has double-moment information for rain). The K05 method was previously used by a multitude of studies (e.g., Kain et al., 2008; Weisman et al., 2008; Kain et al., 2010; Clark et al., 2012; Pinto et al., 2015) and versions of this method are found in many widely-used post-processing packages such as Read/Interpolate/Plot (RIP) version 4 and NCAR Command Language (NCL). The K05 method constants (e.g., graupel density) were adjusted to match the constants within the WSM6 and Thompson schemes during calculation.

The aggregated evaluation of objects across the forecast period using the K05 method is presented in Figure 6. While WSM6 had nearly identical object counts to observations at 2 km with the WRF method (dashed lines), the K05 method (solid lines) contains 45% more objects that nearly doubles the areal coverage bias that was already present with the WRF method. At the 3-km melting level height, the under-forecasting of object counts and areal coverage found with the WRF method is no longer present, with object counts nearly doubling and the areal coverage being over three times more than observations with the K05 method. The increase in object counts and areal coverage with the K05 method (relative to the WRF method) is visible across all heights for WSM6. Contrary to the WSM6 K05 results, the Thompson biases in over-predicting the number and areal coverage of objects that were present with the WRF method are similar or substantially reduced throughout all heights with the K05 method. The object count bias is reduced by around half above the melting level height by using the K05 method; however, the greatest differences are in the areal coverage values. For example, for Thompson forecasts at 4 km, the WRF method areal coverage was 160% greater than observations, which is reduced to only



25% with the K05 method (Fig. 6b). While Thompson mean object sizes were typically around  $30 \text{ km}^2$  larger than observations with the WRF method, the K05 method generates objects that have very similar mean sizes (and standard deviations) to observations, from 2 km up to 9 km. For many heights and parameters, the variability in switching simulated reflectivity calculations results in equal if not larger differences than by retaining the same calculation but switching microphysical schemes.

Analysis of the vertical reflectivity distribution within convective cores using the K05 method reveals that WSM6 CFADs have only minor differences between the two methods (Fig. 7b compared to Fig. 4b). The 5 to 10 dBZ weak bias at the height of the melting level visible in the WRF method is not present using the K05 methodology and only a slight increase in the strong bias is visible above 8 km (Fig. 7c). The Thompson CFAD changed more noticeably and contains less spread with the K05 method (Fig. 7d compared to Fig. 4d), resulting in the forecast CFAD looking more similar to the observed CFAD. The reduced spread in the reflectivity distributions is due to a lack of the high intensity bias that was present in the WRF method (Fig. 7e). These reductions in core intensity with the K05 method are also visible in Figure 8. The high bias in the frequency of WSM6 convective cores reaching higher altitudes is relatively unchanged between the K05 and WRF methods, but the weak bias in reflectivity magnitudes is lessened (Fig. 8a). The amount of WSM6 cores surpassing 50 dBZ at the 2 km height increases from 24.5% in the WRF method to 42.2% in the K05 method, better matching observations; however, the greatest changes in intensity are limited to below the melting level as the K05 and WRF profiles have marginal differences aloft (Fig. 8a, d). The high bias in Thompson core depths improves, reducing from 44.6% of cores reaching 6 km to 28% (as compared to 20% in observations). The difference is further improved at 10 km, where only 3.5% of K05 Thompson cores reach 10 km as compared to 6.9% with the WRF method, where

the observed frequency is 3.3% (Fig. 8c). The high intensity bias in the Thompson simulated reflectivity is also improved throughout all heights, although forecasted cores are still too intense, particularly near the surface (Fig. 8c, f). In general, the normalized frequency of Thompson cores match the observed cores very well above 6 km, except the strongest cores still contain higher reflectivity values than observations (Fig. 8f).

While the objective evaluation across the entire period shows differences statistically, a subjective analysis is necessary to see how physically consistent storm systems are and to investigate the entirety of the simulated storm structure. A case representative of the biases found in the analysis is displayed for Thompson forecasts on the native model grid in Figure 9. The 01 UTC 2 June 2015 (25-hour) forecast includes a mesoscale convective system and scattered isolated deep convection. At all heights, it is apparent that high reflectivity regions cover more area using the WRF method than the K05 method, which agrees with the overall findings that convective cores are larger and more intense using the WRF method (Fig. 9a, d). Performance between the two methods is most similar at 6 km, especially in coverage (Fig. 9b, e). Although not the main focus of this study, large differences in anvil intensity exist at 10 km, with the K05 anvils being 5 to almost 15 dBZ more intense than the WRF method and seemingly containing larger anvils (when considering  $> 0$  dBZ regions; Fig. 9c, f, i).

A cross-section through one of the intense storm cells following from point A to B in Fig. 9 reveals major differences between the two methods (Fig. 10). The differences noted in the statistical analysis between the two reflectivity calculations are clearly visible in the cross-sections. The maximum reflectivity in the K05 convective core is nearly 10 dBZ weaker than in the WRF method core (Fig. 10a, c, e). The general higher intensity of cores using the WRF method results in wider and taller

cores as the 45 dBZ isoline (i.e., the definition of convective core in this study) extends to  $\sim 11$  km (as compared to  $\sim 9$  km in the K05 method). The same higher intensity associated with the WRF method is seen for shallower convection (e.g., cell at 49.5 degrees N in Fig. 10b, d, f). There is also a complete lack of a stratiform precipitation region in the K05 method that is present in the WRF method. Based on the reflectivity field, the ( $> 0$  dBZ) anvil appears to be longer, and wider in the K05 method (Fig. 10a, c). Interpretation of these simulated reflectivity fields may be misleading, as one may draw the conclusion that there is little snow aggregation present in the anvil of the K05 storm; however, the opposite conclusion may be reached when analyzing the storm using the WRF method yet the snow hydrometeor fields are identical for both (the differences stem from K05 using the same fixed size distribution regardless of scheme). The reflectivity field generated by the WRF method and associated with the stratiform region covers almost twice the area of the corresponding K05 field (Fig. 10b, d). The differences between the K05 and WRF methods are likely caused by K05 assuming a fixed distribution of hydrometeors; however, more detailed analysis investigating individual hydrometeor fields is required to better understand where the differences stem from.

Figure 11 shows the same case as Figures 9 and 10, except for the WSM6 scheme using the WRF method to determine the simulated reflectivity field only. While the forecasted convection has different characteristics than those depicted in Figure 9 because of the variation in microphysical schemes, it is easy to identify the corresponding convective elements. The cross-section across this storm system reveals an artificial decrease in the reflectivity magnitude at the 3-km melting level by around 10 dBZ (Fig. 11d), which is commonly present in the WRF method for WSM6. This misrepresentation of reflectivity intensity at the melting level causes WSM6 forecasts to contain a sharp decrease in objects and area at that height (Fig.

3a, b) and was depicted well in the aggregated CFADs (Fig. 4c). It was also noted that WSM6 contained more small, cellular elements than Thompson (which was observed throughout the forecast period); however, these cells are typically weaker (i.e.,  $< 40$  dBZ) and did not have a pronounced impact on the evaluated convective cores. While the cores for this case were visible extending to the same height in Thompson and WSM6 forecasts, the anvil regions are also much less pronounced in the WSM6 scheme (Fig. 11c, d as compared to Fig. 9 and Fig. 10), which is likely caused by the single-moment representation of rain and snow hydrometeors (e.g., Morrison et al., 2009).

## 2.5 Summary and Conclusions

Four months of daily summertime forecasts generated by two models with differing microphysics (WSM6 and Thompson) were evaluated to determine the accuracy in depicting the vertical structure and depth of convection. Forecasts were evaluated by comparing the simulated reflectivity field as internally generated within the WRF model to observations taken by two S-band radars. An analysis of convective objects aggregated over the entire forecast period identified several differences between observed and forecasted reflectivity objects. At 2-km both forecasts performed reasonably well; however very large differences were found at higher altitudes. Forecasts were found to over-predict the number of convective objects above the melting layer. Mean forecasted object sizes were also too large, resulting in convective objects that covered double the amount of area relative to observations. Simulated convective cores were also deeper than in observations, with forecasts generating between 1.4 and 2.2 times as many observed cores reaching 6 and 10 km. While the number, depth, and coverage of simulated convective cores was greater than observations, the intensities varied according to microphysics scheme. WSM6 cores were generally too weak, and

regions of high reflectivity did not extend far enough vertically. Furthermore, the vertical reflectivity distribution did not follow the same slope as observations. Thompson cores were significantly stronger, with 13.5% of all cores containing reflectivity values that surpassed the highest observed reflectivity value. Thompson CFADs had a similar slope to observations, but they contained considerably more spread. The results showcase the importance of expanding forecast evaluation into multiple levels, as evaluation at one level may lead to conclusions that are not representative for the entire three-dimensional system. Further development and implementation of three-dimensional evaluation techniques are needed to ensure identification of, and subsequent improvement of, forecast biases. Future precipitation evaluation studies should consider integrating three-dimensional reflectivity data into their evaluation, as analysis of the convective vertical structure can be useful in helping to identify where biases in the precipitation field originate from.

In order to assess the uncertainty introduced by variations in reflectivity calculation, a sensitivity study was performed comparing the WRF simulated reflectivity field against a commonly utilized methodology (K05 method). While the results using both methods led to the same overall conclusions, there were a number of major differences between the two methods. For some analyses, the differences introduced by changing reflectivity calculation method were of the same magnitude as differences generated by changing microphysical schemes. While the simulated reflectivity field provides a way to evaluate model forecasts in a three-dimensional manner and can reveal a plethora of information about convective processes, determining the radar reflectivity factor from model simulations contains substantial uncertainty, especially for single-moment schemes. Both forecasters and researchers should use the simulated reflectivity field as general guidance but be cautious when relying on it for specific storm attributes. To alleviate some of the uncertainties, development and use of for-

ward radar simulators may produce simulated variables that are more equivalent to those observable by radar, thereby allowing a more direct storm comparison.

Table 1: The WRF model configuration used to generated forecasts over the region depicted in Figure 1. The cumulus parameterization scheme was only used for the 9- and 27-km domains.

WRF Model Configuration	
Version	3.7.0
Longwave	RRTM
Shortwave	Dudhia
Land Surface	Noah
Planetary Boundary Layer	YSU
Cumulus Parameterization	Kain-Fritsch
Surface Layer	MM5 Similarity
Microphysics	WSM6 or Thompson

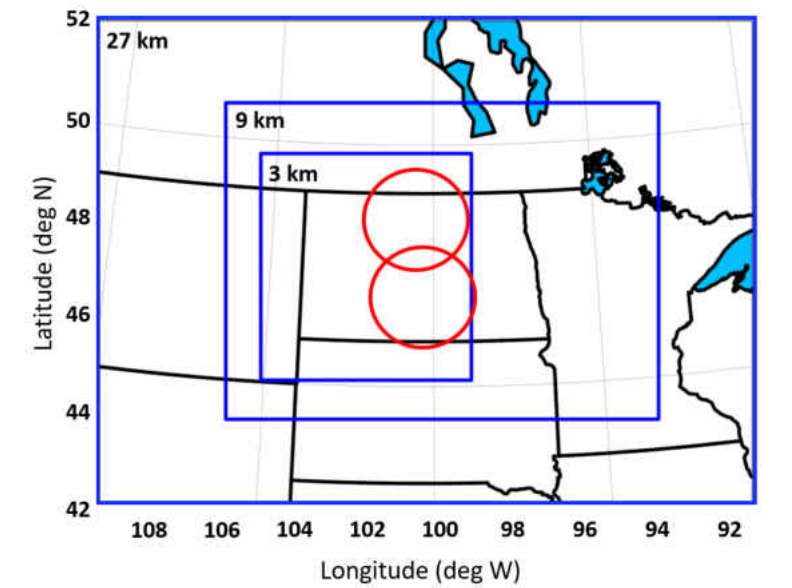


Figure 1: The (blue) WRF model domains and (red) 126 km radar range from the KMBX and KBIS WSR-88D radars where the forecast analysis is performed.



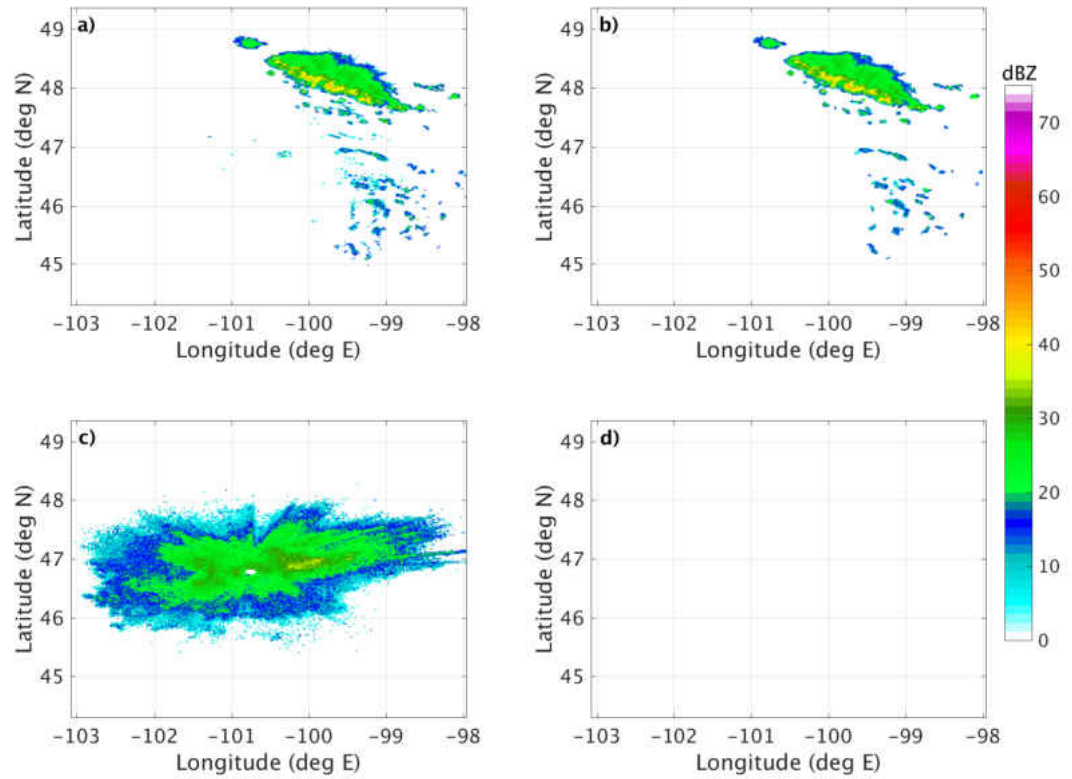


Figure 2: The (left column) raw and (right column) quality controlled composite reflectivity fields as observed by the KBIS radar on a, b) 1 October, 2015 at 2305 UTC and c, d) 22 September, 2015 at 0417 UTC , respectively.

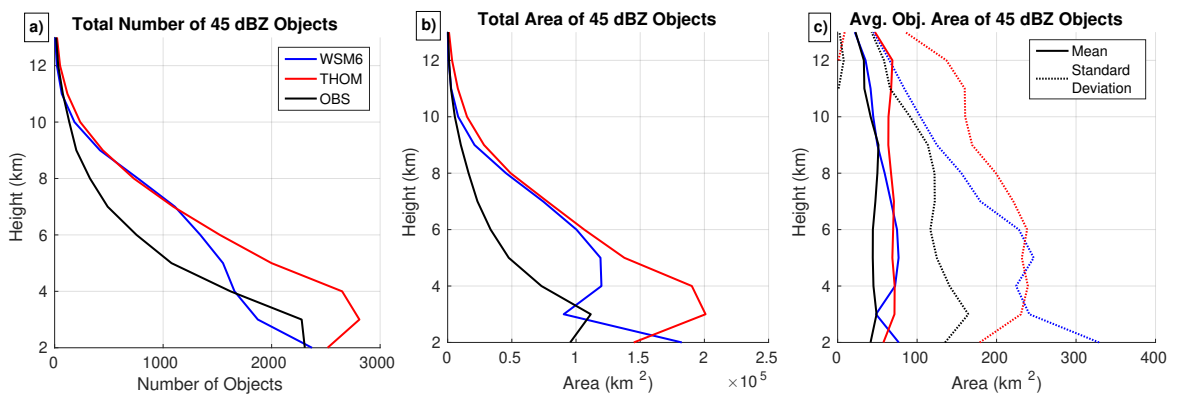


Figure 3: The a) total number, b) area coverage, and c) mean object area of  $\geq 45$  dBZ objects with height. The blue lines represent forecasts using the WSM6 microphysical scheme, red lines represent the Thompson microphysical scheme, and the black lines represent radar observations. The solid lines in panel (c) represent the mean object area and the dashed lines are the mean  $\pm$  one standard deviation (Note that the dashed lines are not plotted when negative).

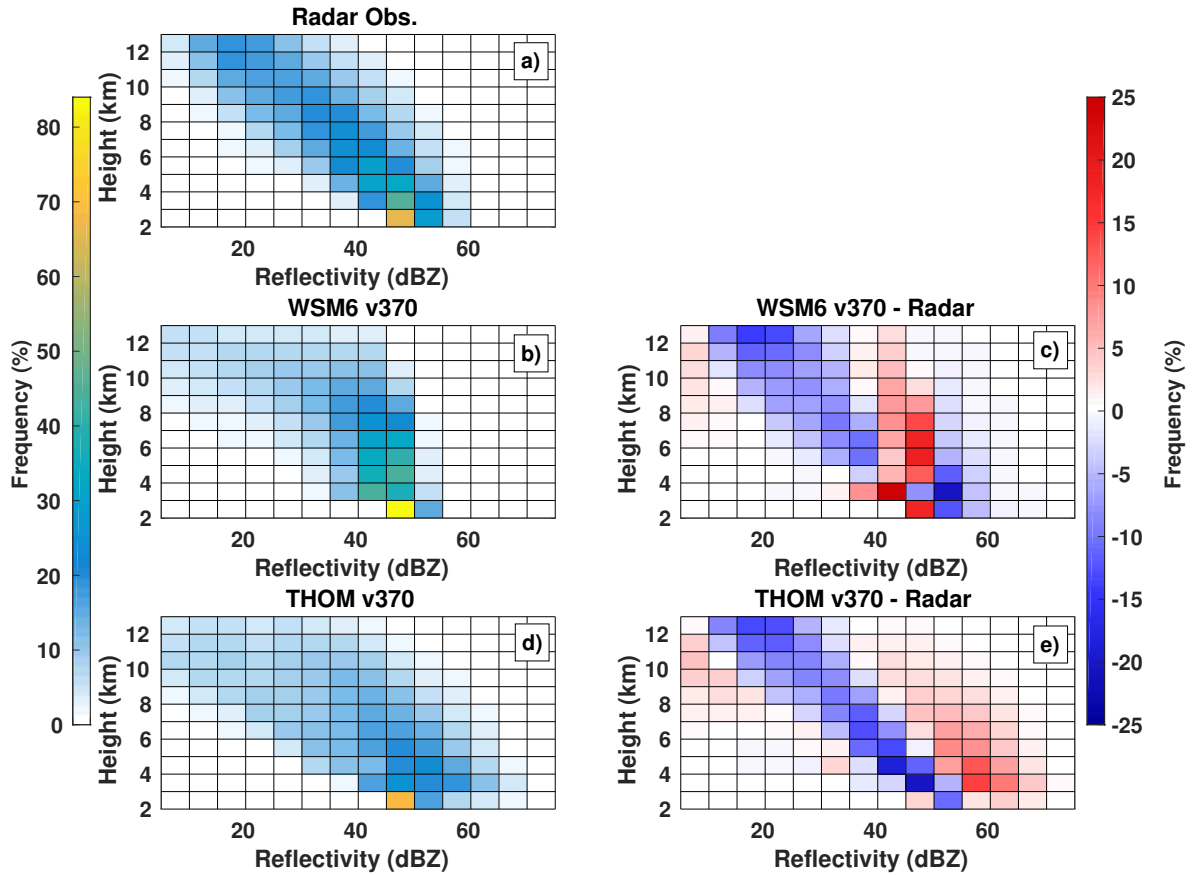


Figure 4: Contoured frequency by altitude diagrams (CFADs) of reflectivity within convective cores identified at the 2 km height for a) radar observations, b) WSM6 forecasts, and c) Thompson forecasts across the entire analysis period. The differences between CFADs are shown for d) WSM6 and radar observations and e) Thompson and radar observations, where the blue shading indicates under-representation by the model and red shading indicates over-representation by the model. The observed and simulated reflectivity values are binned in 5 dBZ bins.

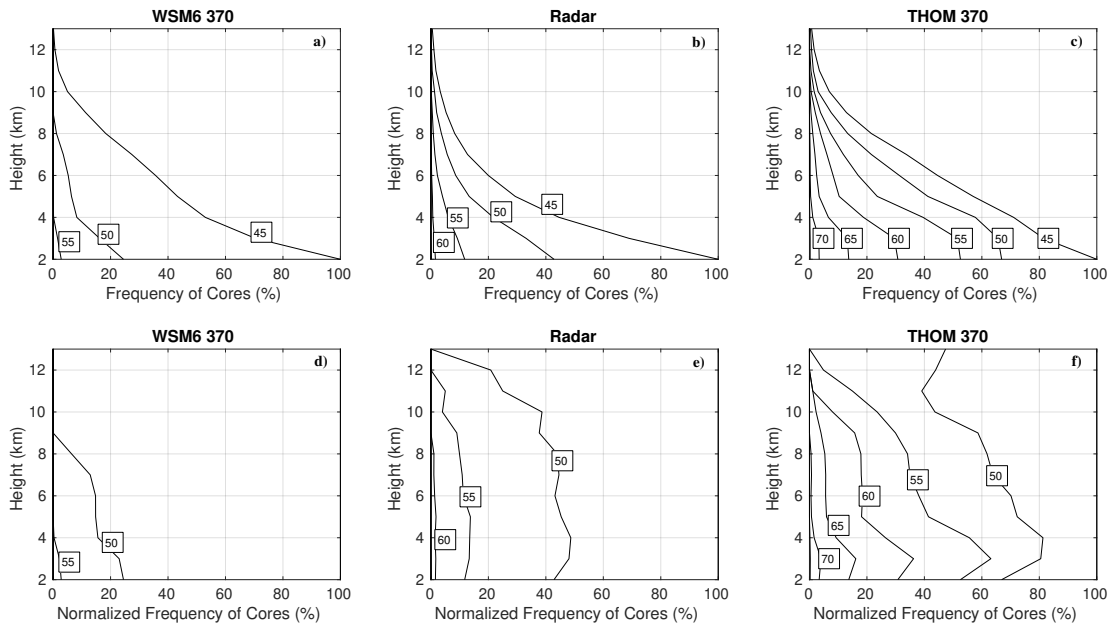


Figure 5: The frequency of convective cores identified at 2 km height surpassing certain reflectivity thresholds with height for a) WSM6 forecasts, b) radar observations, and c) Thompson forecasts. The percentage of objects that surpass certain reflectivity thresholds normalized by the amount of convective cores identified at each height are shown for d) WSM6 forecasts, e) radar observations, and f) Thompson forecasts.

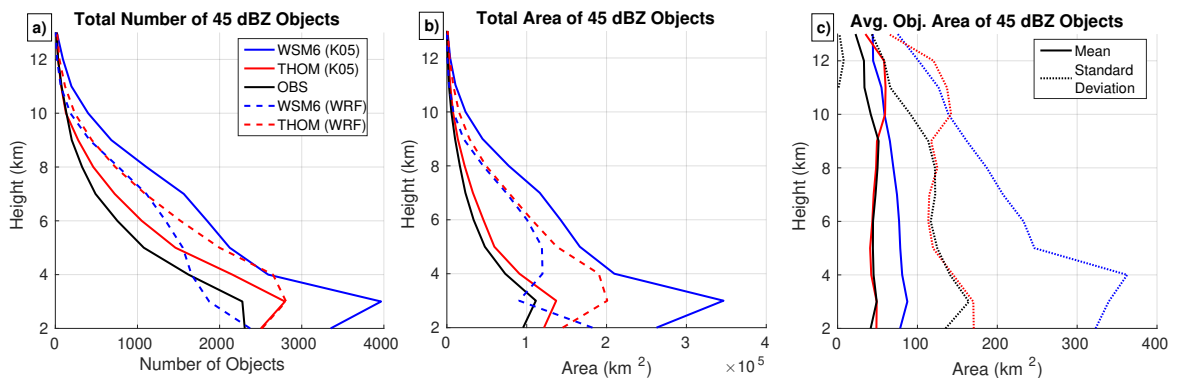


Figure 6: As in Figure 3, except using the K05 method. The dashed lines in panels a) and b) present the WRF method for reference (from Figure 3).

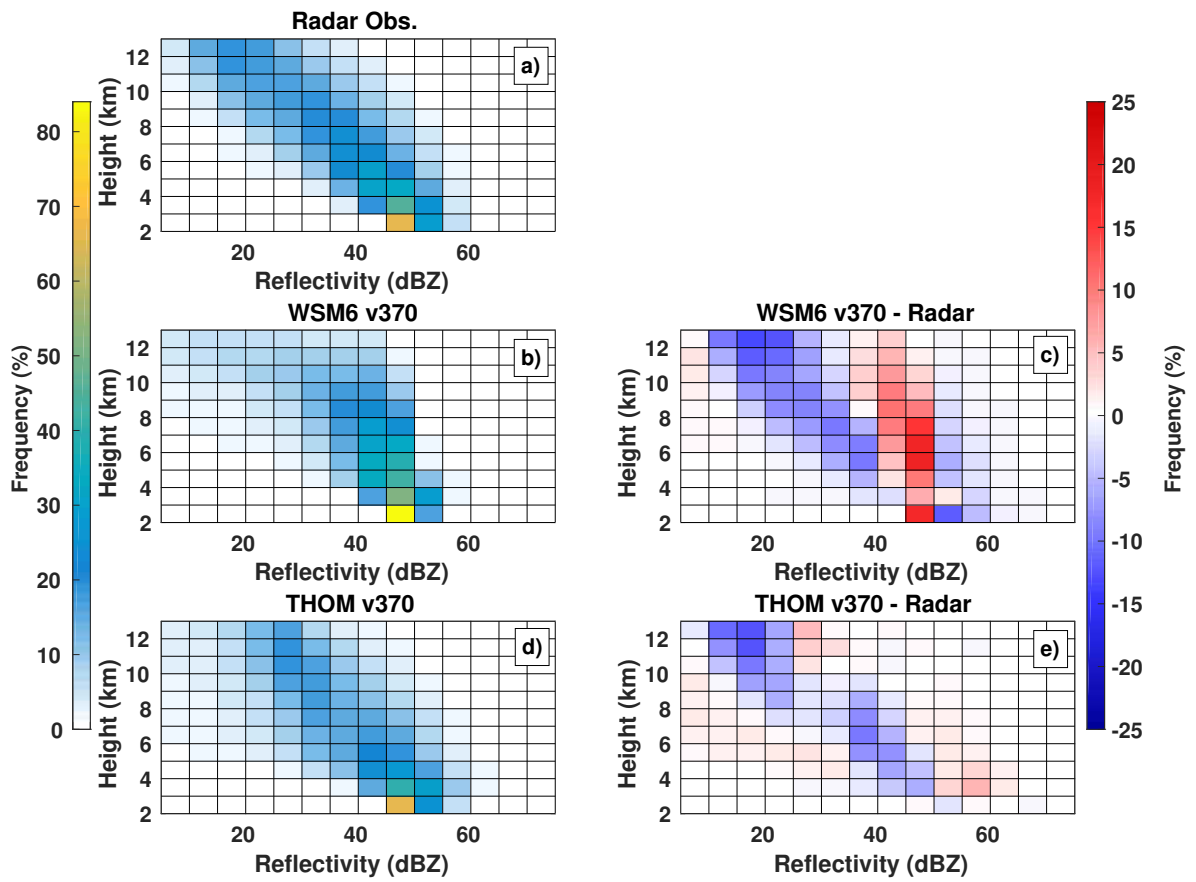


Figure 7: As in Figure 4, except using the K05 simulated reflectivity calculation.

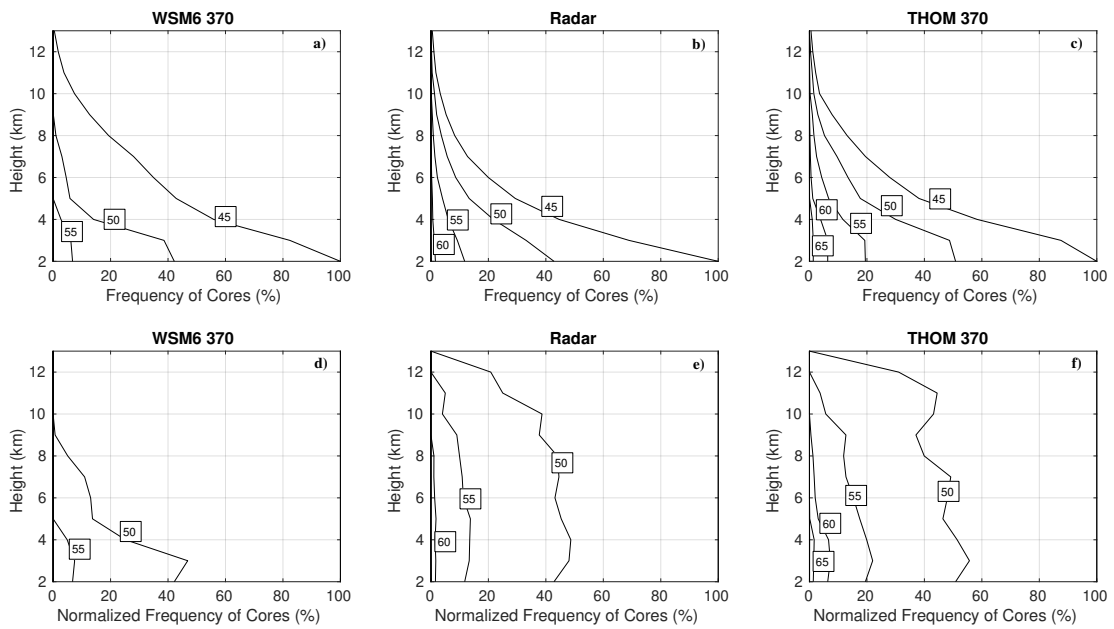


Figure 8: As in Figure 5, except using the K05 simulated reflectivity calculation.

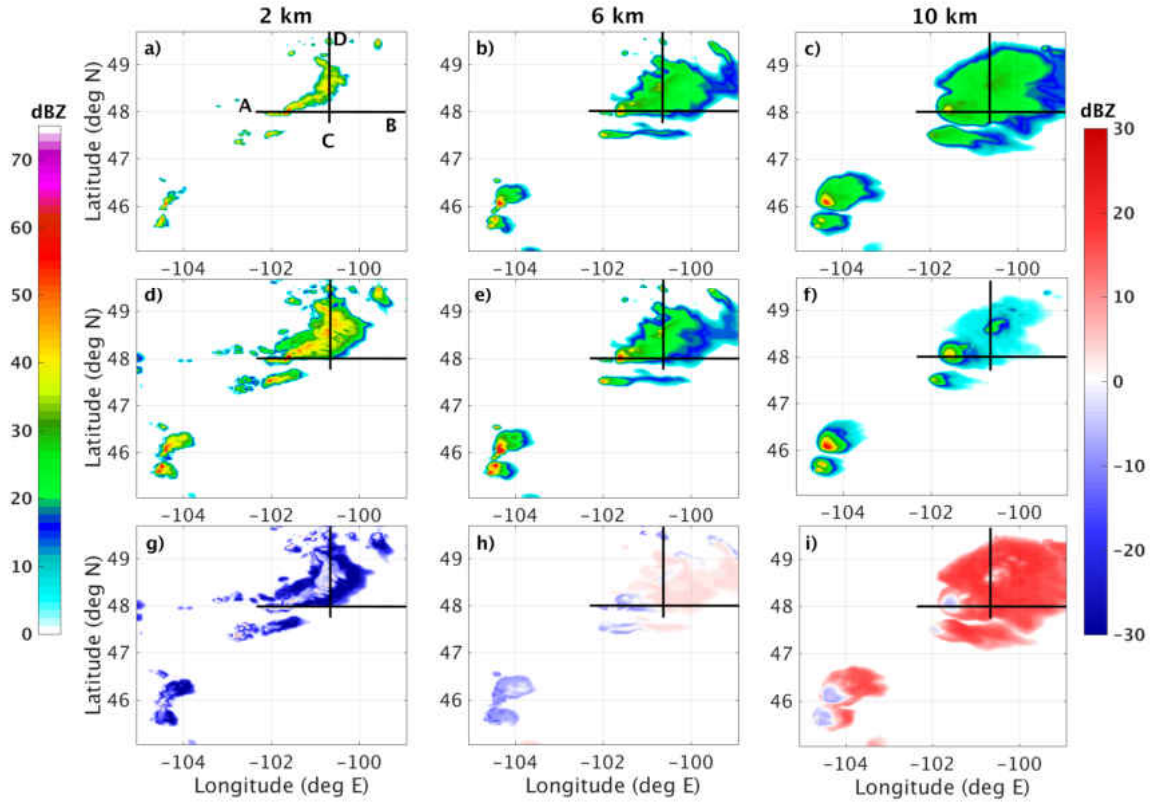


Figure 9: The Thompson scheme’s simulated reflectivity field on the native model grid using the (top) K05 method and (bottom) WRF method at a, d) 2 km, b, e) 6 km, and c, f) 10 km for a 25-hour forecast valid on 2 June, 2015 at 01 UTC. Panels (g), (h), and (i) are the absolute difference between the K05 and WRF simulated reflectivity magnitudes in (a, d), (b, e), and (c, f) respectively, where red denotes higher reflectivity magnitudes in the K05 method and blue denotes higher reflectivity magnitudes in the WRF method.



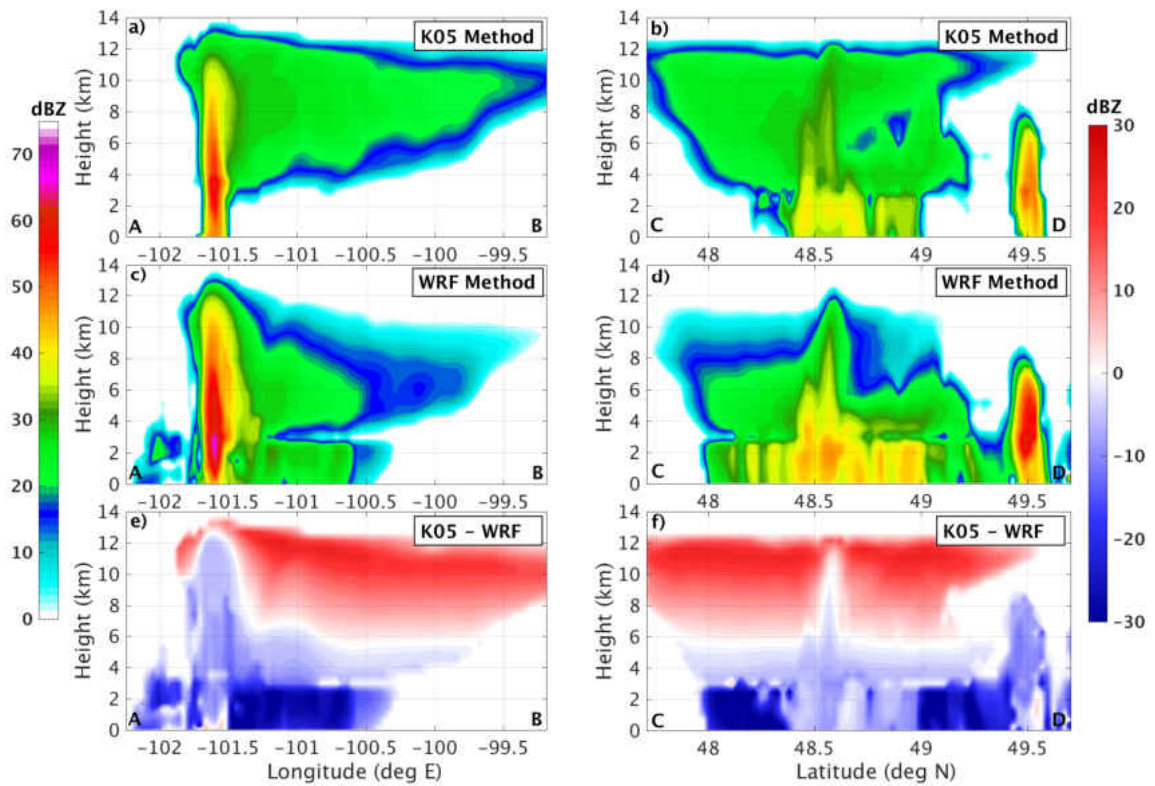


Figure 10: A vertical cross-section of the Thompson scheme’s simulated reflectivity field on the native model grid using the a, b) K05 method and c, d) WRF method following the black line from a, c) point A to point B and b, d) point C to point D in Figure 9. Panels (e) and (f) are the absolute difference between the K05 and WRF simulated reflectivity magnitudes in (a, c) and (b, d), respectively, where red denotes higher reflectivity magnitudes in the K05 method and blue denotes higher reflectivity magnitudes in the WRF method.

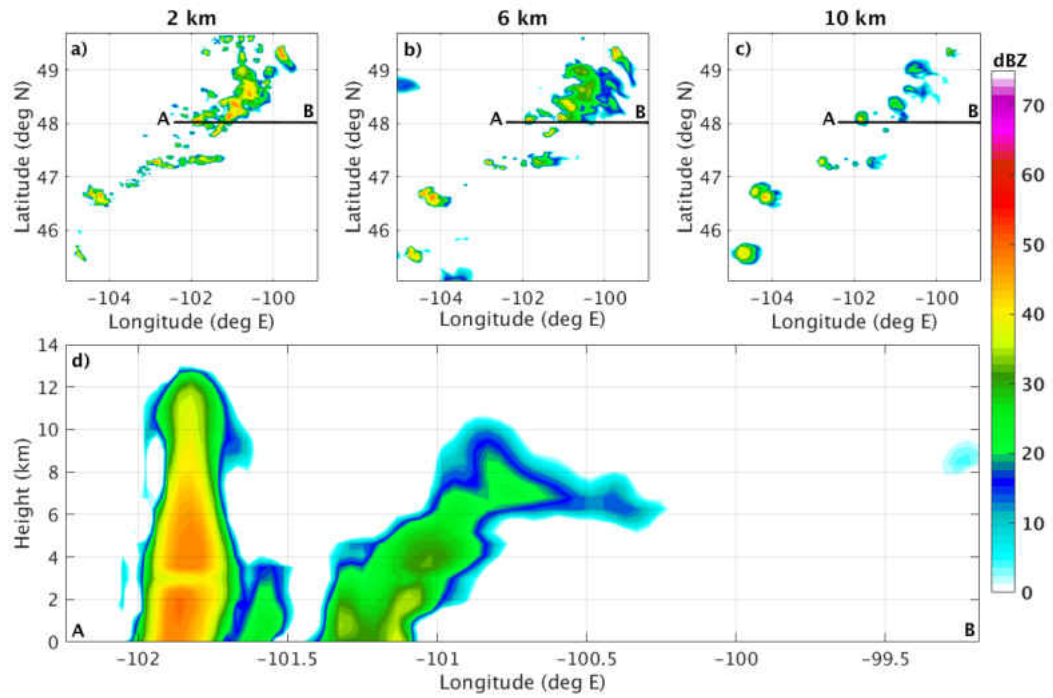


Figure 11: The WSM6 scheme's a) 2 km, b) 6 km, and c) 10 km simulated reflectivity field on the native model grid using the WRF method for a 25-hour forecast, valid on 2 June, 2015 at 01 UTC and the d) vertical cross-section of reflectivity from point A to B.

## CHAPTER 3

### STORM LABELING IN 3 DIMENSIONS (SL3D): A VOLUMETRIC RADAR ECHO AND DUAL-POLARIZATION UPDRAFT CLASSIFICATION ALGORITHM

#### 3.1 Introduction

Regions of convective and stratiform precipitation are known to differ considerably in terms of (1) microphysical composition and associated precipitation rates (e.g., Houghton, 1968), (2) thermodynamic properties including diabatic heating rates, perturbations to the altitude of the environmental melting (or freezing) level, and related storm divergence profiles (e.g., Johnson, 1984; Houze, 1989; Mapes and Houze, 1993), and (3) their relative frequency of occurrence across the globe (e.g., Schumacher and Houze, 2003). Recognition of these differences has motivated several previous studies to develop methods that objectively identify convective and stratiform precipitation in radar and satellite observations in order to enable improvements in our understanding of their differences and associated physical and dynamical processes (e.g., Adler and Negri, 1988; Williams and Ecklund, 1995; Steiner et al., 1995; DeMott et al., 1995; Anagnostou and Kummerow, 1997; Hong et al., 1999; Anagnostou, 2004; Bringi et al., 2009; Yang et al., 2013).

One of the most well-known and utilized schemes for convective-stratiform classification using ground-based radar observations is the Steiner et al. (1995, hereafter referred to as SHY) method. SHY employs a three-step procedure to distinguish between convective and stratiform precipitation using observations at the lowest elevation in a radar volume. First, any value of the radar reflectivity factor at horizontal

polarization ( $Z_H$ ) that exceeds a specified threshold is considered convective. Second, an additional exceedance threshold is used to identify previously unclassified convective elements if the  $Z_H$  at a grid point surpasses the mean background  $Z_H$  over a set radius (similar to that of Adler and Negri, 1988). Third, a convective radius of influence is applied to all identified locations of convection from steps 1 and 2 to broaden the horizontal extent of the convective classification to regions of similarly intense precipitation. In other words, depending on the magnitude of  $Z_H$  relative to the mean background value, all points within a certain radius are labeled as convective.

Many studies have built upon the SHY procedure by incorporating vertical information in the classification to improve its performance, particularly in cases where convection is weak, stratiform precipitation is intense, or convective regions are strongly tilted in the vertical (thereby inadvertently decoupling convective precipitation at low altitudes from its source aloft). Biggerstaff and Listemaa (2000) added a step to compute the vertical lapse rate of  $Z_H$  in the 3 km layer above the  $Z_H$  column-maximum value to improve the skill of the convective classification in the SHY method, and a “brightband” ( $Z_H$  maximum occurring near the melting level in stratiform precipitation) detection method to improve the stratiform classification. More recently, Powell et al. (2016) incorporated a range-dependent SHY-based classification to low elevations of single-radar observations in their native polar coordinates to better identify shallow convection and improve precipitation estimation. Feng et al. (2011) focused on the top-of-atmosphere radiation budget of convective systems and added a convectively-generated anvil (i.e., anvil resulting from direct detrainment from the convective updraft; e.g., Mullendore et al., 2009) cloud classification to the SHY scheme. Feng et al. (2011) used five constant altitude levels from three-dimensional composites of multiple ground-based radars to distinguish between convective, stratiform, and anvil clouds.

While the aforementioned studies incorporated vertical storm information in the SHY procedure, the primary classification between convective and stratiform precipitation in SHY-based algorithms and similar approaches is completed using a single low-altitude map of  $Z_H$ . For research purposes such as quantitative precipitation estimation, SHY-based methods applied to single-radar observations can be adequate. However, the reliance of SHY-based methods on low-altitude observations alone (typically at a level of 2-3 km) limits their utility for other research topics that require knowledge on the vertical structure of convection. For example, information on the extent and depth of convection are necessary elements of analysis for studies on convective mass transport, cloud microphysics, diabatic heating, and gravity wave generation (e.g., Kuo and Anthes, 1984; Nuret and Chong, 1998; Alexander, 2004; Schumacher et al., 2004; Mullendore et al., 2005; Barth et al., 2007; Park et al., 2009; Homeyer et al., 2014; Srinivasan et al., 2014). In addition, the use of stringent low-altitude  $Z_H$  thresholds may misclassify weak and/or shallow convection as stratiform rain or intense stratiform rain as convection, subsequently introducing biases in the analysis of precipitating systems. Methods that leverage the three-dimensional information widely available in ground- and satellite-based radar observations are required to overcome these limitations.

In this study, a method to classify radar echo using three-dimensional high-resolution composites of radar observations from the NEXRAD WSR-88D network is developed. The Storm Labeling in 3-Dimensions (SL3D) algorithm uses the vertical depth and echo top altitude of  $Z_H$ , additional dual-polarization (or polarimetric) radar quantities, and the altitude of the environmental melting level to stratify radar echo into five categories (described in Section 3.3 below). Several cases of varying organization, complexity, and regionality are used to demonstrate the performance of the SL3D algorithm and compare it to the traditional SHY approach. The primary

goal of SL3D is to enable new analyses on topics that require information on vertical storm structure by producing a regionally unspecific classification of precipitating systems using three-dimensional radar observations.

### 3.2 Radar Data

The radar data used in this study are three-dimensional composites of NEXRAD WSR-88D observations, where the volume data from individual radars are provided by the National Centers for Environmental Information (NCEI; NOAA National Weather Service, 1991). Radar composites are created following the methods outlined in Homeyer (2014) and updated in Homeyer and Kumjian (2015). In short, observations from each radar are binned in space and time at 5-minute intervals in a volume with 0.02 degree ( $\sim 2$  km) longitude-latitude grid spacing and 1 km grid spacing in the vertical. For binning, observations are weighted out to 300 km in range and within 5 min of the composite time using a Gaussian function. Grid volumes with large cumulative bin weights (i.e., the sum weight of all observations contributing to a grid volume) and a high fraction of echo detection in contributing radar scans are retained for analysis. The largest weights are given to observations closest to a radar location and closest in time to that of the composite. The time binning component is the only difference from the procedure outlined in Homeyer and Kumjian (2015); hence no interpolation is performed on the individual radar scans in time or space. Each composite contains up to four polarimetric variables for analysis:  $Z_H$ , differential radar reflectivity ( $Z_{DR}$ ), specific differential phase ( $K_{DP}$ ), and co-polar correlation coefficient ( $\rho_{HV}$ ). Composites in the years 2013-Present contain all four variables since the upgrade of the NEXRAD WSR-88D network to dual-polarization was completed in early 2013, while composites for cases prior to 2013 contain only  $Z_H$ .

The polarimetric variables from NEXRAD radars provide information on the size, shape and/or orientation, concentration, and phase of precipitable hydrometeors. For example,  $Z_H$  and  $Z_{DR}$  convey information about the size and shape of the largest hydrometeors in a sample volume, respectively, while  $K_{DP}$  is indicative of the presence of non-spherical hydrometeors in the beam volume. If particles are small compared to the wavelength of the radar, positive values of  $Z_{DR}$  and  $K_{DP}$  indicate scatterers with horizontal-to-vertical axis ratios greater than 1, such as rain drops, while negative values represent scatterers with horizontal-to-vertical axis ratios less than 1. Alternatively,  $\rho_{HV}$  enables discrimination between meteorological and non-meteorological echoes and detection of volumes with mixed-phase (water and ice) precipitation. Meteorological scatterers have  $\rho_{HV}$  near 1 for volumes with uniform particle phases.  $\rho_{HV}$  reduces to values as low as 0.8 in mixed-phase regions or can be even lower in the presence of large hail. Non-meteorological scatterers typically have  $\rho_{HV}$  values less than 0.5. While  $\rho_{HV}$  is not used in the SL3D classification, echo with  $\rho_{HV}$  values below the 0.5 threshold are removed from the polarimetric radar composites prior to analysis in this study. More information on the physical meaning of each polarimetric radar variable is available in textbooks (e.g., Doviak and Zrnić, 1993; Bringi and Chandrasekar, 2001) and review papers (e.g., Herzegh and Jameson, 1992; Zrnić and Ryzhkov, 1999; Straka et al., 2000; Ryzhkov et al., 2005c; Kumjian, 2013a,b,c).

The  $Z_H$  field may contain considerable bias due to beam broadening, partial or complete beam shielding, attenuation by atmosphere and hydrometeors, and sidelobe contamination.  $Z_H$  observations may also contain artifacts such as ground clutter, second-trip echoes, and three-body scatter spikes. The dual-polarization variables ( $Z_{DR}$ ,  $K_{DP}$ , and  $\rho_{HV}$ ) are subject to substantial biases and artifacts, some of which are unique compared to traditional single-polarization variables such as  $Z_H$ .  $\rho_{HV}$  is

often the least impacted by biases and/or artifacts, with many non-typical values in precipitation being microphysically informative. For example, a reduction in  $\rho_{HV}$  near the melting level in stratiform rain regions is present due to the coexistence of liquid and frozen hydrometeors in the radar volume.  $K_{DP}$  suffers from a large amount of random noise but is not affected by calibration errors and systematic biases.  $Z_{DR}$  is largely sensitive to calibration errors and is often systematically biased up to  $\pm 0.5$  dB in observations from WSR-88D radars (e.g., Cunningham et al., 2013; Homeyer and Kumjian, 2015). As a result, systematic  $Z_{DR}$  biases are corrected for in individual radar scans prior to their inclusion in the composites using a “natural scatterer” approach (e.g., Ryzhkov et al., 2005a). Well-known artifacts such as non-uniform beam filling, differential attenuation, or depolarization of the radar beam are not corrected for as these are both difficult to detect objectively and are often insignificant relative to the scale of the radar composites (see Homeyer and Kumjian (2015) for additional detail and justification).

### 3.3 SL3D algorithm

The storm classification algorithm used in this study (SL3D) stratifies radar echo into five categories: convection, convective updraft, precipitating stratiform, non-precipitating stratiform, and ice-only anvil. In summary, the objective of the SL3D convective classification is to identify precipitation that is directly generated by convective motions (i.e., strong vertical motion or “updrafts”). Precipitating (non-precipitating) stratiform encompasses any mixed-phase cloud that does not contain convective updrafts and is (is not) precipitating. Anvil is considered as ice-only cloud resulting from upper-tropospheric detrainment of ice crystals by convection or advected from a convectively-generated stratiform region. More detailed descriptions of the classification categories are defined in their corresponding sections below and a



summary of the criteria applied to the radar observations is presented in Table 2. It is important to note that the convection classification occurs first and is incrementally followed by the stratiform (precipitating and non-precipitating) and anvil classifications. Convective echo cannot be re-labeled as stratiform or anvil. Similarly, echo identified as stratiform cannot be relabeled as anvil. Once the precipitating and non-precipitating echo regions are identified, echo may be identified as convective updraft within 12 km of any echo classified as convection if one of several conditions are met, which are outlined below.

SL3D incorporates information from the atmospheric environment. Namely, the altitude of the  $0^{\circ}$  C level (i.e., the melting level) is used, which is obtained from radiosonde observations for the cases presented in this study. While it is possible to couple melting layer identification algorithms to SL3D using the radar observations alone (e.g., Giangrande et al., 2008), it is outside the scope of this study to evaluate and determine the sensitivity to each method. Since any objective classification is prone to error, it is the authors' preference to limit such error sources for the SL3D algorithm and specify the altitude of the melting level.

### **3.3.1 Convection and Stratiform**

As outlined in the Introduction, there are distinct microphysical and thermodynamic differences between convective and stratiform precipitation. Convective precipitation occurs when strong, deep mesoscale uplift and/or positive buoyancy leads to the development and growth of cloud particles. As the droplets are lofted into the middle troposphere, they freeze and grow rapidly by collection and glaciation of additional supercooled liquid water (e.g., Churchill and Houze, 1984). These updrafts can loft precipitable particles to the upper troposphere and thereby result in deep, vertically erect columns of high  $Z_H$  values observed by radar. Updrafts can eject large amounts

of ice crystals in the upper troposphere, while large, precipitation-sized particles fall out of the updraft and reach the surface as precipitation. As the particles descend, they melt, collide, and coalesce with other particles and lead to even higher  $Z_H$  near the surface.

Stratiform precipitation results from weak mesoscale ascent at altitudes typically above the freezing level that leads to the formation, growth, and fallout of ice crystals to lower altitudes. Upper-level detrainment from deep convection is often a common source of ice crystals in stratiform regions. Ice crystals can also be actively generated in the stratiform region above the melting level (e.g., Braun and Houze, 1994). The falling ice crystals in a stratiform system aggregate and lead to moderate rates of precipitation (relative to that in convection). If the aggregates descend below the melting level, they are often visible in radar observations as a shallow layer of elevated  $Z_H$  (i.e., the brightband) or reduced  $\rho_{HV}$  immediately below the melting level altitude.

While the vertical structures of convective and stratiform systems are distinct, their column-maximum  $Z_H$  (i.e., composite reflectivity) and low-level  $Z_H$  values can be similar in magnitude. For example,  $Z_H = 40$  dBZ at 3 km may just as easily be considered convective as stratiform. Thus, in order to avoid the obvious limitations of a  $Z_H$  threshold-based convective-stratiform classification at a single altitude, the SL3D algorithm uses the depth of radar echo (i.e., continuous vertical column of  $Z_H$ ), its maximum altitude (i.e., echo top), and its intensity relative to surrounding echo to distinguish between convective and stratiform regions. The SL3D convection classification utilizes height information to identify deep convection by locating enhanced regions of  $Z_H$  that extend above the melting layer. These vertical columns of enhanced  $Z_H$  are effectively used as a diagnostic, or proxy, for convective motion. Only strong vertical motions can loft large particles high enough to be able to generate the

associated continuous high  $Z_H$  in the vertical dimension, while the enhanced  $Z_H$  of stratiform precipitation is confined to the melting level and below.

The SL3D convective classification is internally partitioned into three steps to better identify convection of various extent and intensity. Radar echo in each grid square that meets any of the following three criteria is labeled as convection: (1)  $Z_H = 25$  dBZ echo top extending above 10 km, (2) horizontal layer “peakedness” that is the maximum of either 4.0 dBZ or  $10.0 - Z_H^2/337.5$  dBZ, or (3)  $Z_H \geq 45$  dBZ at any altitude above the melting level. Each of these three criteria are discussed in more detail below.

Criteria (1) uses  $Z_H = 25$  dBZ, but  $Z_H \geq 30$  dBZ is frequently used to define convection and/or the convective extent (e.g., DeMott and Rutledge, 1998). While the SL3D convective classification is relatively insensitive to the choice of  $Z_H = 30$  dBZ or  $Z_H = 25$  dBZ, the slightly lower  $Z_H = 25$  dBZ is used to better capture weaker convection where the  $Z_H = 30$  dBZ boundary may be present just below 10 km. For criteria (2), the horizontal “peakedness” of each grid point is evaluated to better locate shallow and mid-level convection that may be embedded within a deep or expansive stratiform cloud. Building upon the SHY algorithm, peakedness is considered as the difference between the  $Z_H$  of the grid point being evaluated and the median  $Z_H$  of a 12 km radius around the point. The peakedness of a grid point is determined at each height where radar echo is present in the lowest 9 km of the radar volume. A grid point is labeled as convection if at least 50% of the vertical column peakedness surpasses a threshold that varies with  $Z_H$  (i.e., 50% of the vertical radar echo surpasses the peakedness threshold). This variable threshold approach is equivalent to that outlined in SHY, but a slightly altered relationship is used: the higher of 4.0 dBZ or  $10.0 - Z_H^2/337.5$  dBZ. This alteration is based on both constant peakedness thresholds used in studies prior to SHY (e.g., Churchill and Houze, 1984)

and our intended avoidance of an absolute reflectivity limit for convective/stratiform discrimination when the variable peakedness threshold reaches zero. Lastly in criteria (3), the 45 dBZ threshold is generally considered to be indicative of the transition point from graupel to small hail at S-band and is only routinely generated by riming in convective updrafts (e.g., Straka et al., 2000). No  $Z_H$  associated with the stratiform region should approach this threshold above the melting level, but it may approach or exceed 45 dBZ below the melting level via microphysical or dynamical processes.

Once convective regions are identified using the three criteria outlined above, two quality control techniques are applied that modify the classification. Any single convective grid point that is adjacent only to non-convective grid points is removed as they are expected to be false or inconclusive based on the classification criteria. Once the single-point classifications are removed, any grid points immediately adjacent to remaining convective echo are also classified as convective if their column-maximum  $Z_H \geq 25$  dBZ. The reason for reclassifying the adjacent grid squares and expanding the convective classification is similar to that of the convective radius step of SHY. Grid squares that are marginally below the peakedness threshold but are on the periphery of identified convective regions are likely resultant from the same convective processes.

Grid points that do not meet the convective criteria undergo possible stratiform classification. The stratiform classification in SL3D is split into two mutually exclusive categories: (1) precipitating stratiform and (2) non-precipitating stratiform. While vertical velocities in stratiform regions are typically an order of magnitude smaller than those in convection, considerable differences in vertical velocities between precipitating and non-precipitating stratiform clouds have also been documented. For instance, Schumacher et al. (2015) found that mean vertical velocities in the tropics from the near surface to 10 km ranged from  $-0.1$  to  $0.2$   $\text{m s}^{-1}$  for stratiform and  $0.1$  to  $0.9$   $\text{m s}^{-1}$  for convection. The full spectra of vertical velocity measurements varied

from about  $-2$  to  $2 \text{ m s}^{-1}$  for stratiform and  $-5$  to  $18 \text{ m s}^{-1}$  for convection. For non-precipitating cloud (their transitional anvil), the mean vertical velocities were weaker than stratiform and varied from  $-0.05$  to  $0.05 \text{ m s}^{-1}$ , with minima and maxima ranging from about  $-1.25$  to  $1.5 \text{ m s}^{-1}$  (Schumacher et al., 2015). The non-precipitating stratiform region encompasses the transition between precipitating stratiform and ice-only anvil, where some stratiform growth (i.e., aggregation) has occurred but does not lead to precipitation. Ideally, regions categorized as precipitating stratiform include only those observations with non-convective precipitation at the surface. However, since radar coverage is limited near the surface, data at  $3 \text{ km}$  is used to make the primary distinction between precipitating and non-precipitating echo. The  $3 \text{ km}$  height is the lowest altitude with near-uniform coverage in the NEXRAD WSR-88D network. When available, data below  $3 \text{ km}$  is used to identify additional regions of weak precipitation. The  $3 \text{ km}$  analysis level is also used in the SHY algorithm for comparisons with SL3D in Section 3.5 below.

Precipitating stratiform is defined as that with  $Z_H \geq 20 \text{ dBZ}$  at  $3 \text{ km}$  or  $Z_H < 20 \text{ dBZ}$  present at  $3 \text{ km}$  when  $Z_H \geq 10 \text{ dBZ}$  is present at one or more of the lower altitude levels ( $1$  or  $2 \text{ km}$ ). These  $Z_H$  thresholds are similar to other studies such as Feng et al. (2011) and Schumacher et al. (2015), which generally use  $Z_H \geq 10 \text{ dBZ}$  to identify stratiform precipitation at lower altitudes. The higher  $Z_H = 20 \text{ dBZ}$  threshold at  $3 \text{ km}$  relative to the aforementioned studies was determined by analyzing several dozen cases, and is in place to ensure precipitation is reaching the surface.  $Z_H = 10 \text{ dBZ}$  at  $3 \text{ km}$  is alone not a reliable indicator of precipitation. Non-precipitating stratiform encompasses any echo that extends to altitudes at or below the melting level, but does not meet the requirements for precipitation outlined above.

As briefly outlined above, the melting level altitude in SL3D is manually specified to assist with echo classification. While some unique radar features can be used

to help identify stratiform regions (e.g.,  $Z_H$  brightband or its commonly used dual-polarization counterpart, a  $\rho_{HV}$  reduction), such techniques are not employed within SL3D. These techniques are not used because (1) not all stratiform regions contain such signatures and some dual-polarization indicators of stratiform rain can also be found in deep convection (e.g., see Houze, 1993, 1997; Steiner et al., 1995; Schumacher et al., 2015), (2) there is insufficient vertical resolution in the radar dataset used in this study for resolving such features, and (3) these techniques would include unnecessary limitations to the classification based on the availability of dual-polarization variables, which are only present in the WSR-88D data since late 2012. Fundamentally, the goal of the SL3D algorithm is to be applicable regardless of radar polarization, intrinsic vertical resolution, and region or large-scale environment.

### 3.3.2 Anvil

In previous studies, anvil regions have commonly been separated into modes thought to be representative of unique physical and/or dynamic regimes. For example, Frederick and Schumacher (2008) stratified anvil into mixed-phase and ice-only cloud due to important differences in radiative properties between the two categories. The SL3D anvil classification is designed to identify non-precipitating ice-only cloud above the melting level resulting from convective detrainment in the upper troposphere (mixed-phase non-precipitating clouds are categorized as non-precipitating stratiform). To accomplish this, SL3D identifies regions as anvil if radar echo ( $Z_H \geq 0$  dBZ) is only present above an altitude of 5 km, which is typically the maximum height of the melting level and is similar to the approach of Feng et al. (2011) and Carletta et al. (2016). Requiring the 5 km threshold prevents potential misclassifications of echo in environments where the melting level altitude approaches the surface and the likelihood of the anvil precipitating increases.

### 3.3.3 Convective Updraft

Following the convection, stratiform, and anvil classification, radar echo is evaluated to determine whether or not signatures indicative of strong convective updrafts are present. In order to identify convective updrafts, the SL3D algorithm searches for three well-known radar signatures: (1) weak echo regions (WERs; bounded or unbounded, e.g., Browning and Donaldson, 1963; Musil et al., 1986; Calhoun et al., 2013), (2)  $Z_{DR}$  columns (e.g., Caylor and Illingworth, 1987; Illingworth, 1988; Bringi et al., 1991; Conway and Zrnić, 1993; Ryzhkov et al., 1994; Brandes et al., 1995; Loney et al., 2002; Scharfenberg et al., 2005; Kumjian and Ryzhkov, 2008; Kumjian et al., 2014), and (3)  $K_{DP}$  columns (e.g., Zrnić et al., 2001; Loney et al., 2002; Kumjian and Ryzhkov, 2008; van Lier-Walqui et al., 2015). WERs are elements of a convective storm with relatively low  $Z_H$  values at lower altitudes that are at least partially bounded horizontally and above by relatively high  $Z_H$  values. Such WERs have been shown to represent a lack of large, precipitable hydrometeors due to strong (rapid) ascent of developing particles in the updraft of a convective storm. From a radar detectability perspective, the most easily identifiable WERs are bounded by regions of high reflectivity. Bounded WERs are generally indicative of a strong updraft embedded within a strongly sheared environment, and are commonly found in supercell convection (e.g., Markowski, 2002). The SL3D algorithm identifies WERs in the altitude layer below 7 km where (1) the vertical  $Z_H$  gradient  $\geq 8$  dBZ km<sup>-1</sup> in a grid volume, (2) echo is present in at least 6 of the 8 horizontally adjacent grid volumes, and (3) column-maximum  $Z_H \geq 40$  dBZ. Although some storms contain WERs extending to altitudes above 7 km, the altitude limitation and neighborhood check are necessary to limit over-identification of updraft regions in vertically tilted convection.

For radar composites that include the full suite of polarimetric variables, updraft classifications also include  $Z_{DR}$  and  $K_{DP}$  columns.  $Z_{DR}$  and  $K_{DP}$  columns are

regions of enhanced positive values (generally  $\geq 1$  dB and  $\geq 0.5$  dB km<sup>-1</sup>, respectively) extending to altitudes above the environmental freezing level. The columns represent deep lofting of liquid hydrometeors within a convective updraft. Since  $Z_{DR}$  is a size-weighted measure of particle shape,  $Z_{DR}$  columns identify updrafts capable of lofting large rain drops above the freezing level (that may also include small hail).  $K_{DP}$  columns, on the other hand, indicate updrafts that have lofted large concentrations of moderately sized (2–4 mm) rain drops above the freezing level (e.g., Loney et al., 2002). van Lier-Walqui et al. (2015) found that  $K_{DP}$  columns are not only a good indicator of the presence of an updraft, but changes in the volume of a  $K_{DP}$  column are correlated to changes in updraft mass flux.

Snyder et al. (2015) have recently developed an algorithm to objectively identify  $Z_{DR}$  columns in single-radar observations. In short, their algorithm identifies a column of  $Z_{DR} \geq 1$  dB at altitudes above the freezing level, which is consistent with the approach that is designed independently here using a slightly higher  $Z_{DR}$  threshold. In the SL3D algorithm,  $Z_{DR}$  and  $K_{DP}$  columns are identified as those with  $Z_{DR} \geq 1.5$  dB or  $K_{DP} \geq 0.5$  deg km<sup>-1</sup> extending at least 1 km above the freezing level. The slightly higher threshold of  $Z_{DR}$  compared to Snyder et al. (2015) used here accounts for calibration issues and potential broadening of polarimetric signatures when data are composited from multiple radars. The  $K_{DP}$  threshold is set to discriminate between high concentrations of rain drops above the melting level and snow (which typically occupies a  $K_{DP}$  range of  $-0.5$  to  $0.5$  deg km<sup>-1</sup>). In addition, only echo with  $Z_H \geq 15$  dBZ is considered for  $Z_{DR}$  column detection, and echo with  $Z_H \geq 30$  dBZ for  $K_{DP}$  column detection in order to avoid common biases (noise) along the periphery of radar echoes.

SL3D updrafts are identified by locating  $Z_{DR}$  and  $K_{DP}$  columns in grid volumes that lie within 12 km of any previously identified convective grid point. The 12 km



radius was chosen to enable identification of updrafts that may be displaced relative to the intense precipitation column, especially in vertically tilted storms. Based on the authors' experience, this distance is also a common scale of horizontal separation between convective cells in organized convective systems. Therefore, this radius is viewed as an upper limit for neighborhood searching, since expanding the radius to larger values may commonly enable false identifications in non-convective rain regions.

Lastly, following identification of WERs,  $Z_{DR}$  columns, and  $K_{DP}$  columns, a single quality-control step is applied. Similar to the approach for convective classification, any grid point identified as a convective updraft that is horizontally surrounded by non-convective updraft echoes (i.e., single-point classifications) is removed and the prior classification restored.

### 3.4 Example SL3D Classifications and Convective Updraft Validation

In order to demonstrate the application of the SL3D classification, a simple dual-polarization case is shown in Figure 12 that contains a large supercell storm in north Texas at 0055 UTC on 18 May 2013. The melting level for this case is  $\sim 4.75$  km. Figure 12a shows a 3-km constant altitude map of  $Z_H$ . The supercell reaches a maximum  $Z_H$  near 60 dBZ and contains a well-defined hook echo at 3 km in the southwest quadrant of the storm. An extensive anvil region is visible through contrasting regions of echo in the 3-km and column-maximum  $Z_H$  maps (Figs. 12a & 12b) and in the corresponding SL3D classification (Fig. 12c). There are three smaller and weaker convective storms to the north and northeast of the supercell.

The SL3D classification shows that the precipitating portion of the supercell is largely identified as convection, with a broad convective updraft near the location of the hook echo. In order to determine what physical characteristics are contributing to the SL3D classification of the supercell, a vertical cross-section of the polarimetric

variables is presented in Figure 13 along a path that bisects the storm’s hook echo and updraft region (the A–B line in each map of Fig. 12). The vertical sections reveal that both a deep (up to 8 km in altitude) bounded WER and  $Z_{DR}$  column contribute to the updraft classification, while there is no significant  $K_{DP}$  column signature. In addition, the supercell reaches altitudes up to 18 km (consistent with its convective classification) and SL3D convective regions correspond directly to vertically erect volumes of high  $Z_H$ . There is no apparent brightband in the  $Z_H$  section (Fig. 13a) and likewise little echo classified as stratiform rain by SL3D. Both forward and rear ice-only anvil is observed to be extending away from the storm between  $\sim 9$  and 15 km and is captured well by SL3D.

While the example using WSR-88D radar observations in Figures 12 and 13 is encouraging, validation of the performance of the echo-based updraft algorithm is desired to establish confidence in its use. In order to achieve such validation, examples of SL3D application to two multi-Doppler radar cases are included, which provide measurements of the three-dimensional wind fields within storms. The vertical velocities were retrieved using variational integration of the continuity equation (O’Brien, 1970). Figure 14 presents application of the SL3D algorithm to a supercell storm at 0030 UTC on 30 June 2000 that was observed during the Severe Thunderstorm Electrification and Precipitation Study (STEPS; Lang and Rutledge, 2002; Lang et al., 2004). Since this case includes only single-polarization radar observations (i.e.,  $Z_H$ ), updraft identification in SL3D comes from the WER algorithm alone. The WER identified in SL3D encompasses a large region of the storm extending southeast from the hook echo located on the southwestern flank of the storm at 3 km (Fig. 14a). In addition, the WER coincides with the highest vertical velocities observed in the dual-Doppler wind field (i.e., the updraft; see Fig. 14d). Despite the success of the SL3D identification, there are a couple of points worth noting: (1) while the main

updraft region is identified, another region of enhanced vertical velocity to the north is not identified by SL3D due to the lack of a WER, and (2) the WER identified in SL3D extends to regions in the southeastern portion of the storm that have weak and/or marginal upward motion.

A second validation case is provided in Figure 15. For this case, dual-Doppler radar observations are taken from a storm in northeast Colorado (Basarab et al., 2015; Basarab, 2015) observed at 2230 UTC on 6 June 2012 during the Deep Convective Clouds and Chemistry (DC3) experiment (Barth et al., 2015). In contrast to the STEPS storm, this DC3 case includes dual-polarization observations that allow for validation of the entire three-step updraft identification algorithm in SL3D. For this case, the updraft identified in both SL3D and the Doppler wind field is displaced to the south of the most intense precipitation (Figs. 15a & 15f). Although the updraft region is displaced, the updraft location in the dual-Doppler wind field and SL3D classification are nearly coincident. The WER is once again visible by comparing the 3 km and column-maximum  $Z_H$  (Fig. 15a & 15b, respectively), where the SL3D identified WER is denoted by the black line. In this case, no significant  $K_{DP}$  (Fig. 15d) columns are present so the  $Z_{DR}$  column detection element of SL3D is the primary source of the dual-polarization updraft classification step (white line), as depicted by the the regions of high  $Z_{DR}$  at  $\sim 1$  km above the melting level or a true altitude of 5 km (Fig. 15b).

### 3.5 Comparisons of SL3D with Traditional Methods

As outlined in the Introduction, traditional radar echo classification methods like the SHY algorithm are designed for precipitation estimation and use a single low-altitude map of  $Z_H$  to identify convection and stratiform rain. The SL3D algorithm incorporates the three-dimensional information of the radar observations to build upon such

classifications when information in the vertical is needed. It is therefore important to evaluate the success of this three-dimensional approach and its performance relative to the SHY method in order to determine the impacts on the classification. Several comparisons of the SL3D and SHY classifications are shown in this section for storms with varying organization, large-scale forcing, and geographic location. In order to produce comparable classifications, the SHY algorithm is applied to  $Z_H$  fields at 3 km in each case. Based on the analysis of Feng et al. (2011) using multi-radar composites, a  $Z_H$  threshold of 43 dBZ is used for the first SHY step, a background radius of 6 km for the second step, and convective radius of up to 3 km for the final step. Echo below 10 dBZ is considered to be too weak for precipitation and is not included in the stratiform classification.

Figures 16a-c show maps of column-maximum  $Z_H$ , the SL3D classification, and the SHY classification, respectively, for a collection of deep quasi-linear convective storms primarily within Oklahoma and Southeast Kansas at 0125 UTC on 14 May 2009. The melting level for this case is  $\sim 4.5$  km. Comparison of the SL3D and SHY classifications shows that the outermost boundaries of the precipitating regions are very similar, and any differences in the overall scale of precipitating regions for this case are arguably negligible. However, comparison of the SL3D and SHY classifications shows that convective regions are larger in the SL3D classification. This difference in convective classification is a direct result of the dependence of the SL3D algorithm on the vertical extent of a storm rather than a low-altitude  $Z_H$  threshold and is common across a large number of additional cases. When the SHY algorithm is applied at an altitude of 3 km, it identifies the largest  $Z_H$  values as convective, and expands the convective classification using the two-step radii thresholds. However, the SL3D method identifies a much larger convective region based on the vertical extent of the storm, regardless of the magnitude of  $Z_H$  at lower levels. These dif-

ferences in convective classification are demonstrated further in the vertical cross section labeled A–B in Figure 16a. The largest convective cell in the cross-section has a broader horizontal extent of high reflectivity ( $\geq 30$  dBZ) aloft than near the surface, which is responsible for the broader SL3D convective classification compared to SHY. For the two smaller convective cells in the cross-section, both SL3D and SHY identify the largest  $Z_H$  values as convective, but the SHY algorithm under-represents the horizontal extent of the storms as evidenced by the  $Z_H$  columns.

Figure 17 shows application of the SL3D algorithm to a case containing multiple discrete supercell storms and a Mesoscale Convective System (MCS) over central and northeastern Oklahoma, respectively, at 2325 UTC on 23 May 2011. The melting level for this case is  $\sim 4.25$  km. This case demonstrates the performance of the SL3D classification for a wide variety of convective organizations and intensities. Only single-polarization observations are available, such that updrafts are classified using WER identification alone. Both SL3D and SHY produce reasonable convective classifications within the MCS, again with noticeably larger convective regions in the SL3D classification. Differences in the scales of convective classifications between SL3D and SHY are largest in the supercell storms, which is a reflection of the dependence of SL3D on the depth of the intense reflectivity column. For the WER-only updraft classification in SL3D, this case demonstrates that unless the convection is sufficiently intense, little to no updraft regions are identified using the WER method alone. In particular, each supercell has a clearly defined updraft, demonstrating the robustness of the WER classification method in supercell storms, which (as discussed in section 3.33.3.3) typically contain large bounded WERs. The MCS in the northeastern portion of the domain, however, shows little to no area classified as convective updraft.

The cases presented thus far are largely limited to intense and/or extreme storms located in the Great Plains of the United States. In order to demonstrate the success of SL3D in other regions and environments, three additional cases here and a fourth in Section 3.3.3 below are included. First, Figure 18 shows observations centered over southeast Texas during the landfall of Tropical Storm Bill at 0000 UTC on 17 June 2015. Additional weaker convection and stratiform rain is included in the northwestern portion of the domain and moderately intense convection in the eastern portion of the domain. The melting level for this case is  $\sim 4.75$  km; however, a pronounced increase in the melting level height is noted by the height of bright band within Tropical Storm Bill (A–B, Fig. 18). While differences similar to those outlined in previous cases can be observed here, focus is shifted on differences within the tropical storm and in the broad area of weak convection surrounded by stratiform rain in the northwest portion of the domain. Specifically, the vertical cross-section labeled A–B in Figure 18a bisects Tropical Storm Bill, while the cross-section labeled C–D bisects the weaker convection.

For Tropical Storm Bill, a deep convective tower is observed to be reaching altitudes in excess of 17 km near the center of the storm, followed by a large region of weak-to-moderate stratiform rain radially outward. Both SL3D and SHY classifications correctly identify the convective region near the center of the storm, with the SL3D convective classification extending farther toward the center. The displacement of the SL3D classification relative to that from SHY corresponds to the extension of higher reflectivity aloft, capturing the weaker precipitation just below the high reflectivity column. Radially outward from the convective region, however, is a region with larger differences between the SL3D and SHY classifications. Namely, there is a region of intense stratiform rain classified by SHY as convective. Though overrepresentation of convection by the SHY algorithm is rare, such false classification is due

to the absolute  $Z_H$  threshold used for convective precipitation in the SHY algorithm (i.e., 43 dBZ).

Additional differences between the SL3D and SHY classifications are observed in the cross-section through the weaker convection in Figure 18 (labeled C–D). This cross-section demonstrates the SL3D classification capturing the horizontal extent of higher reflectivity in the weaker storms while the SHY algorithm classifies smaller regions that appear to be primarily limited to exceedances of the 43 dBZ  $Z_H$  threshold at 3 km. Leveraging of additional vertical information in the SL3D algorithm enables improved classification of weak convection for this case and the 23 May 2011 case (see Fig. 17a, white ellipse). This difference highlights that SHY was primarily designed for surface precipitation estimation and is not focused on convective motions aloft.

Further examples of improvements in the classification of weaker convection can be found in storms from the southeast United States and the northeast United States (Figures 19 and 20, respectively). The melting level for the southeast case is  $\sim 4.5$  km and for the northeast case is  $\sim 4.25$  km. For the southeast case, there are two lines of convection: one translating northwest to southeast across the Florida panhandle and the other translating southwest to northeast across central Georgia. For both convective lines, SL3D convective classifications are both more numerous and slightly broader in horizontal extent. A cross-section is presented in Figure 19 through one of the convective regions that is broad in the SL3D classification and marginally present in the SHY classification. In this cross-section, two weak-to-moderate convective cells are apparent on the southern end of the storm and reach altitudes at and slightly above the melting level. While SL3D identifies both of these convective regions well, SHY misses the deeper of the two, which has lower column-maximum  $Z_H$ . Apart from these differences in the convective regions, the two classifications are similar. For the northeast case, there is a large MCS in the

central and northeastern portions of the domain and weaker discrete convection in the western portion of the domain. The SL3D and SHY classifications are similar in the MCS where convection is deeper and  $Z_H$  is more intense, but differ considerably in the weaker convection to the west. The vertical cross-section in Figure 20 bisects both the weak discrete convection and deeper convection of the MCS. Once again, the largest differences between the SL3D and SHY classifications are observed in the weaker, shallower storms, which are marginally captured in the SHY algorithm.

### 3.6 Importance of the Polarimetric Updraft Classification

As outlined in section 3.3.3 and demonstrated using multiple cases in this study, convective updraft identification using single-polarization radar observations with the SL3D algorithm is limited to the existence of WERs in  $Z_H$ . Furthermore, while WERs are a commonly observed radar characteristic of supercell storms (e.g., Markowski and Richardson, 2010) such as in Figure 17, many storms do not contain discernible WERs. This limitation means that updraft regions within the majority of convection observed by single-polarization radar cannot be detected with this method. Fortunately, polarimetric radar observations enable updraft identification within most convective regions without WERs through the detection of rain drops lofted to altitudes above the environmental freezing level ( $Z_{DR}$  and  $K_{DP}$  columns). However, despite representing similar microphysical characteristics,  $Z_{DR}$  and  $K_{DP}$  columns do not always coexist (e.g., Loney et al., 2002). Similarly, both  $Z_{DR}$  and  $K_{DP}$  vary differently with varying sizes and concentrations of hail and hail/rain mixtures. For example, in hail/rain mixtures, the  $Z_{DR}$  signal may be dominated by the presence of large, tumbling hail.  $K_{DP}$  is affected little by hail due to the smaller dielectric constant of ice, lower concentration of hailstones, and spherical shape of hailstones (Balakrishnan and Zrnić, 1990). Thus, in order to enable classification of as many



convective updrafts as possible, it is critical to use  $Z_{DR}$  columns,  $K_{DP}$  columns, and WERs for updraft classification.

Figures 21 and 22 demonstrate the importance of identifying both  $Z_{DR}$  and  $K_{DP}$  columns for a leading-line trailing-stratiform MCS over northern Indiana and Ohio at 0330 UTC on 13 June 2013. The melting level for this case is  $\sim 4.5$  km. Figures 21a-c show maps of column-maximum  $Z_H$ ,  $Z_{DR}$  at 5 km altitude, and  $K_{DP}$  at 5 km altitude, respectively, centered on the leading convective line. The 5 km altitude level for the polarimetric variables is chosen since it lies immediately above the environmental melting (freezing) level. The convective line is clearly visible as a narrow region of large  $Z_H$  ( $> 40$  dBZ) in the column-maximum map, with corresponding updraft regions shown as distinct maxima in the polarimetric variables at 5 km. However, comparison of the  $Z_{DR}$  and  $K_{DP}$  maps reveals that the largest values of each variable generally correspond to relatively low values in the other, especially in the northeastern elements of the convective line. This behavior suggests that  $Z_{DR}$  columns are more prevalent in southwestern elements of the convective line and  $K_{DP}$  columns are more prevalent in the northeastern portion. The spatial offsets are further demonstrated in the vertical cross-sections in Figures 22a-c taken along path A-B in Figure 21, which bisect a storm with sparse  $Z_{DR}$  column detection and prevalent  $K_{DP}$  column detection. These cross-sections show that while no WERs or deep  $Z_{DR}$  columns are evident within the storm, a deep  $K_{DP}$  column extending up to  $\sim 3$  km above the melting level enables detection of the updraft in this case.

### 3.7 Limitations of the SL3D Algorithm

Although several successful applications of the SL3D algorithm were presented, there are some limitations of the method worth discussing here. While the WER updraft classification performs well in strong supercell storms and is able to identify the core

updraft region (e.g., Fig. 14), more quantitative validation is required. Additionally, there are cases where false WER-based updraft classifications are revealed in the SL3D classification. Such false WERs are typically associated with deep convection containing narrow regions of precipitation, leading to updraft classifications on both upstream and downstream sides of the storm. In reality, most updrafts are limited in space to one side of a storm (e.g., Jorgensen et al., 1997; Lang and Rutledge, 2008, and Figs. 14 and 15 here). Examples of this error can be seen for the 14 May 2009 case in Figure 16. It should be noted, however, that such WER errors typically account for  $\ll 1\%$  of the total classified area (determined by analyzing updraft classifications in several additional cases not shown here). Thus, false WER identifications are expected to be negligible in most (if not all) cases.

While the convective classification in SL3D performs well in most cases, there are times where some stratiform rain is falsely classified as convection. The thresholds used in the convective classification here were chosen in order to minimize such errors using many case studies of the NEXRAD WSR-88D composite radar observations. These errors depend strongly on the intensity of stratiform rain and melting level altitude (which may be modified significantly within a storm). Future studies are needed to examine the probability of detection and false alarm rate of the convective classification for weak convection.

Finally, there are important limitations of the SL3D algorithm related to the characteristics of the radar dataset it is applied to. Since the SL3D classifications require substantial vertical information to be successful, it may not be appropriate to apply the algorithm to data from a single NEXRAD WSR-88D radar due to both a lack of vertical coverage and resolution degradation at larger distances from the radar. However, the SL3D algorithm can be applied to any gridded volumetric radar dataset so long as the vertical resolution of the dataset is sufficient ( $\leq 1$  km grid spacing)

and the depth of the volume spans altitudes from 3 to 10 km (as required by the classification categories). In addition, one potential issue for application of the SL3D algorithm related to grid resolution is the sensitivity of the convective classification to the melting level altitude. Namely, for datasets with vertical resolution that meets or exceeds the uncertainty in the altitude of the melting level used, the  $Z_H = 45$  dBZ above the melting level criterion may be erroneously met when the melting level altitude is under-estimated. However, it is worth noting here that this criterion was rarely responsible for convective classifications beyond that identified by the peakedness and echo top criteria for the cases shown in this study. Thus, while this is a possible limitation of the algorithm, it is expected to be negligible in most cases.

### 3.8 Summary and Discussion

This study introduced a new storm classification algorithm for single and dual-polarization radar observations that leverages three-dimensional information of a volumetric dataset: the SL3D algorithm. Several cases of varying intensity, complexity, and regionality were presented to demonstrate the performance of the algorithm. Comparisons between the SL3D algorithm and a traditional storm classification method (Steiner et al., 1995) revealed that convective regions were commonly larger in scale in the SL3D classification. This difference was shown to commonly be the result of including echo top information in the classification and is dependent on the degree of vertical tilt of convection. For cases of less intense convection that traditional methods were unable to detect, the SL3D algorithm was successful in their identification (e.g., see Figs. 18, 19, & 20). Both the increased frequency of identifying convection and the larger convective regions may have an important impact on the latent heating budget of convective systems (e.g., Houze, 1989), especially for

latent heat retrievals utilizing two-dimensional methods to aid in discrimination of echo (e.g., Tao et al., 1993, 2001).

In addition, a novel three-part convective updraft identification method was introduced that leverages both single and dual-polarization radar information and enables identification of updrafts within storms of varying intensity and complexity. For single-polarization radar, a WER identification method was employed, which was shown to perform well in supercell storms but unable to routinely identify updrafts in cases with alternative convective organization. For dual-polarization radar observations, the addition of  $Z_{DR}$  and  $K_{DP}$  column detection was shown to enable updraft identification within most classified convection extending above the melting level (see Figs. 12, 13, 19, 20, 21, & 22). The updraft identification method may be useful for studies investigating the variability of convection and validation of simulated convection in numerical models (e.g., Collis et al., 2013; Varble et al., 2014).

Since SL3D enables the classification of radar echo into five dynamically and physically-based categories it allows for targeted research on individual elements of a storm. For example, previous convective transport studies have found that  $Z_H$  of ice within anvil regions can be used as a proxy for identifying the level of maximum detrainment (e.g., Mullendore et al., 2009; Carletta et al., 2016). Due to its inclusion of an ice-only anvil classification, the SL3D algorithm may enable future improvements in this research. Finally, since the SL3D classification leverages three-dimensional radar observations to classify storms, this approach can be applied globally using satellite-based radar observations from systems such as the Tropical Rainfall Measuring Mission (TRMM) Precipitation Radar (PR) or the Global Precipitation Measurement mission (GPM) Dual-Frequency Precipitation Radar (DPR) for a variety of scientific studies.

Table 2: The criteria required for classification into the five SL3D categories, where  $Z_H$  is horizontally-polarized reflectivity,  $Z_{H\max}$  is the column-maximum  $Z_H$ , and  $Z_{\text{Melt}}$  is the height of the melting layer.

Classification	Criteria
Convection	$Z_H = 25$ dBZ echo top altitude $\geq 10$ km or $Z_H$ peakedness exceeding threshold in at least 50% of echo column between surface and 9 km or $Z_H \geq 45$ dBZ above $Z_{\text{Melt}}$ $Z_H \geq 20$ dBZ at 3 km or $Z_H \geq 10$ dBZ below 3 km
Precip. Stratiform	No echo or $Z_H < 20$ dBZ at 3 km, and echo present below 5 km No echo at or below 5 km altitude, but echo present above $Z_{\text{Melt}}$
Non-Precip. Stratiform Anvil	$Z_{H\max} \geq 40$ dBZ and $\frac{\partial Z_H}{\partial z} \geq 8$ dBZ $\text{km}^{-1}$ with echo in at least 6 of 8 horizontally adjacent grid volumes or $Z_H \geq 15$ dBZ and $Z_{\text{DR}} \geq 1.5$ dBZ extending at least 1 km above $Z_{\text{Melt}}$ or $Z_H \geq 30$ dBZ and $K_{\text{DP}} \geq 0.5$ $\text{deg km}^{-1}$ extending at least 1 km above $Z_{\text{Melt}}$
Updraft	

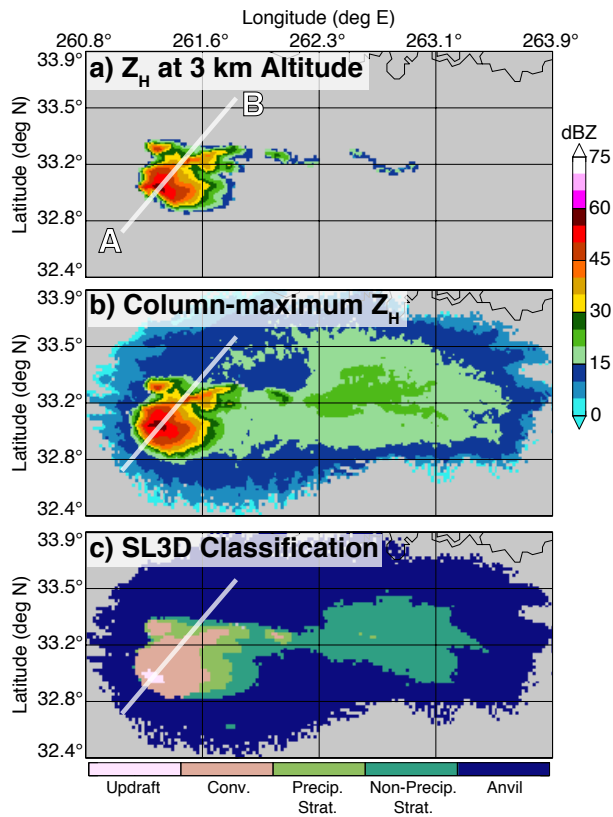


Figure 12: Maps of (a)  $Z_H$  at 3 km altitude, (b) column-maximum  $Z_H$ , and (c) SL3D classification for a supercell located in northeast Texas on 18 May 2013 at 0055 UTC. The thick lines labeled A–B on each map show the location of the vertical cross-sections in Fig. 13.

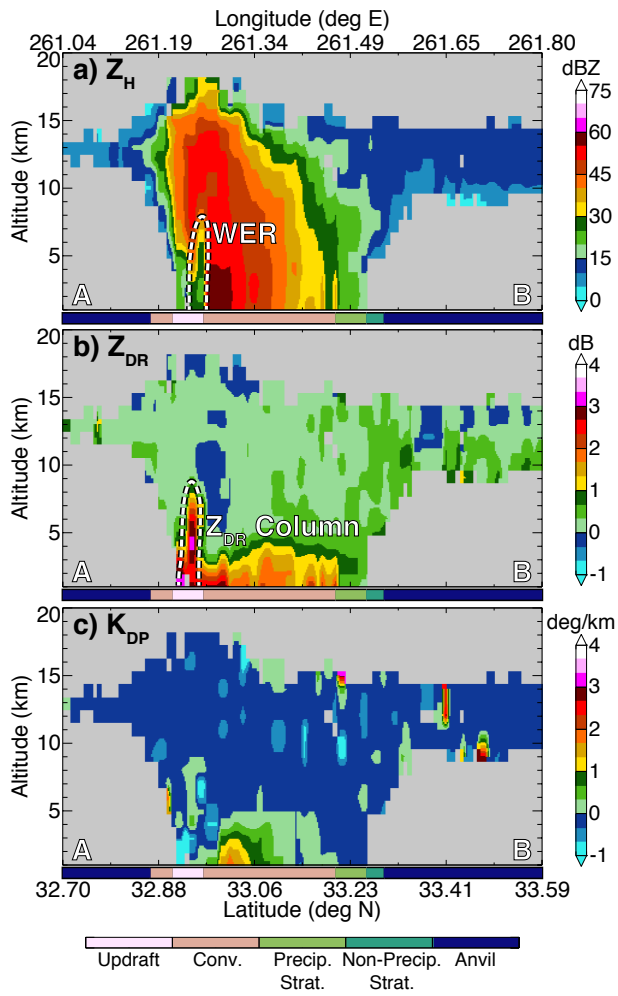


Figure 13: Vertical cross-sections of (a)  $Z_H$ , (b)  $Z_{DR}$ , and (c)  $K_{DP}$  following the thick line in Fig. 12, from A (left) to B (right). The thick colored line at the base of each cross-section shows the corresponding SL3D classification.

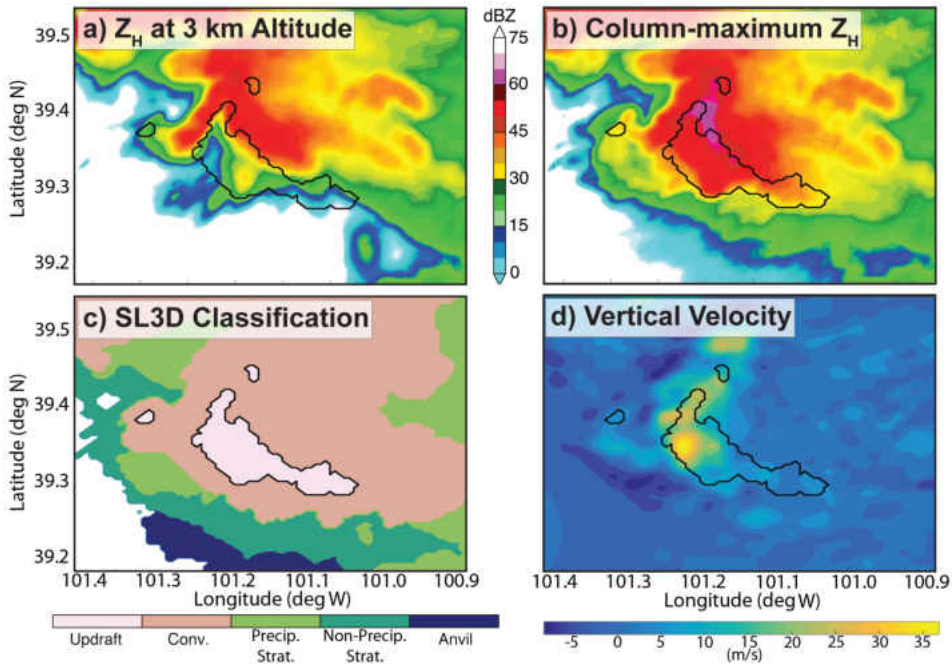


Figure 14: Maps of (a)  $Z_H$  at 3 km altitude, (b) column-maximum  $Z_H$ , (c) the SL3D classification, and (d) dual-Doppler derived mean vertical velocity in the vertical column from a storm observed during the Severe Thunderstorm Electrification and Precipitation Study (STEPS) on 30 June 2000 at 0030 UTC. The black lines denotes the SL3D updraft classification using WER identification alone.



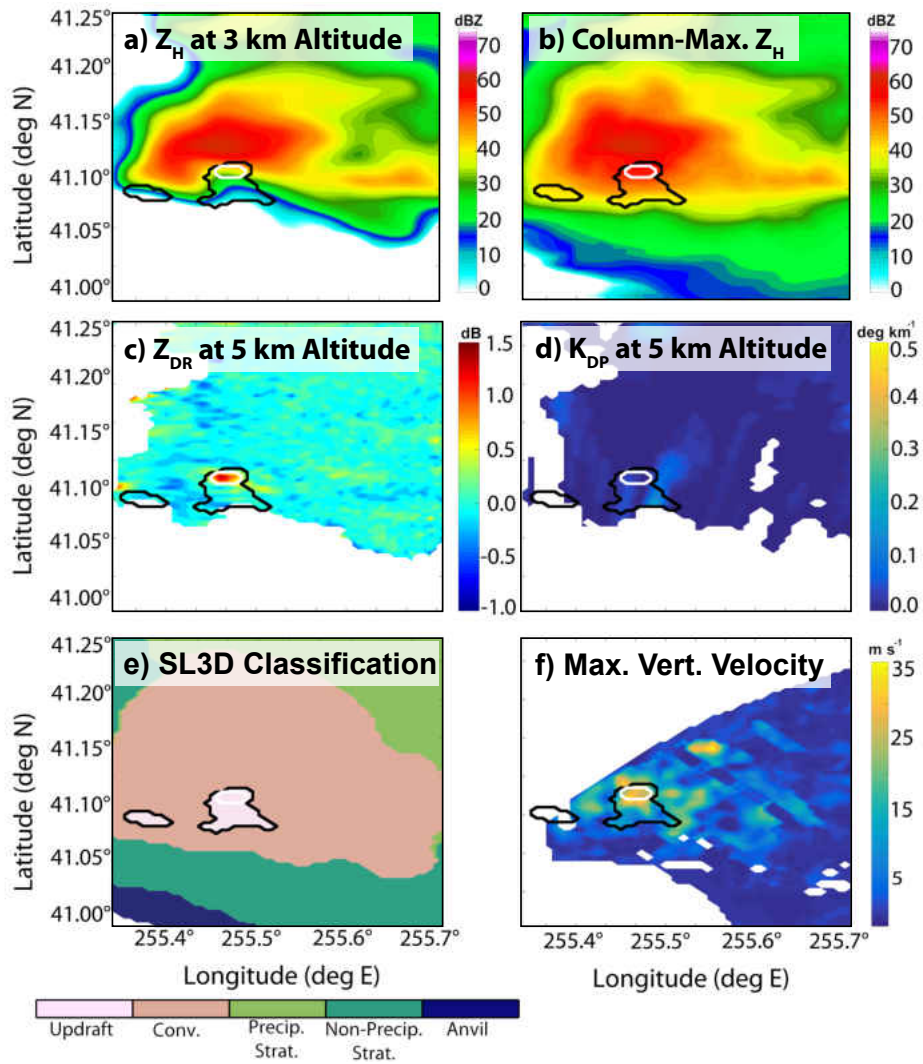


Figure 15: Maps of (a)  $Z_H$  at 3 km altitude, (b) column-maximum  $Z_H$ , (c)  $Z_{DR}$  at 5 km altitude, (d)  $K_{DP}$  at 5 km altitude, (e) the SL3D classification, and (f) maximum dual-Doppler derived vertical velocity on 06 June 2012 at 2230 UTC. The black lines denote the SL3D updraft classification using WER identification alone and the white lines denote the SL3D updraft classification using polarimetric variables alone.

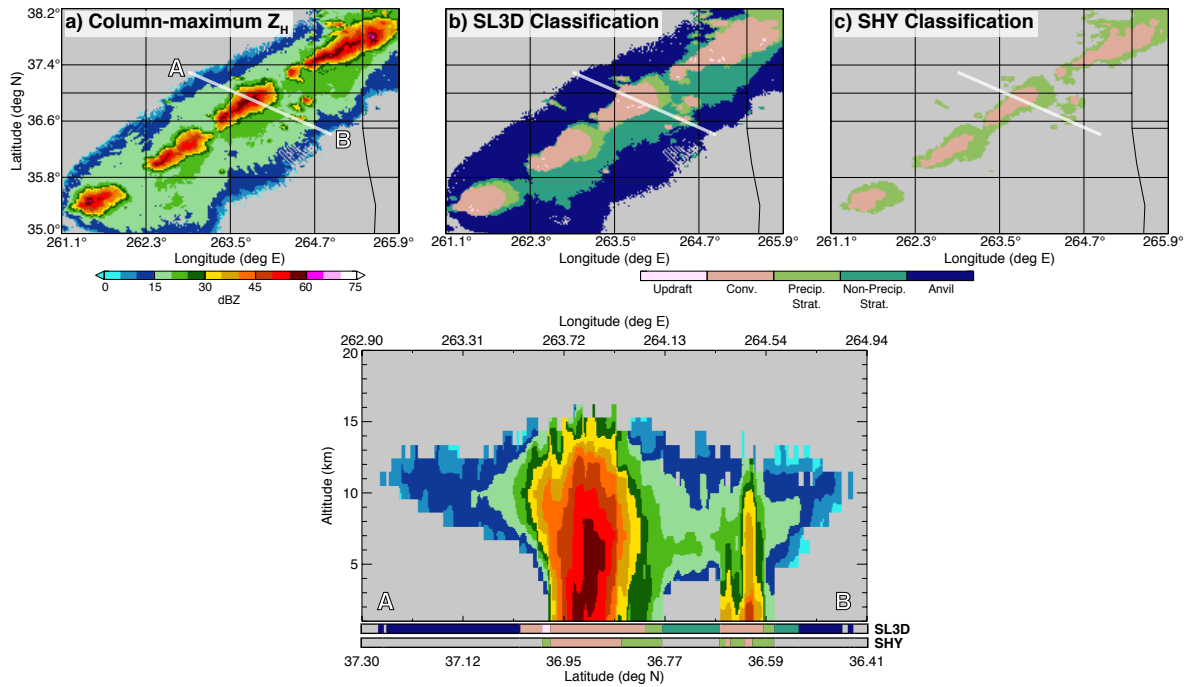


Figure 16: Maps of (a) column-maximum  $Z_H$ , (b) SL3D classification, (c) SHY classification and a vertical cross-section of  $Z_H$  following the thick line labeled A–B for a collection of deep quasi-linear convective storms over Oklahoma and southeast Kansas on 14 May 2009 at 0125 UTC. The thick colored lines at the base of the cross-section show the corresponding SL3D and SHY classifications.

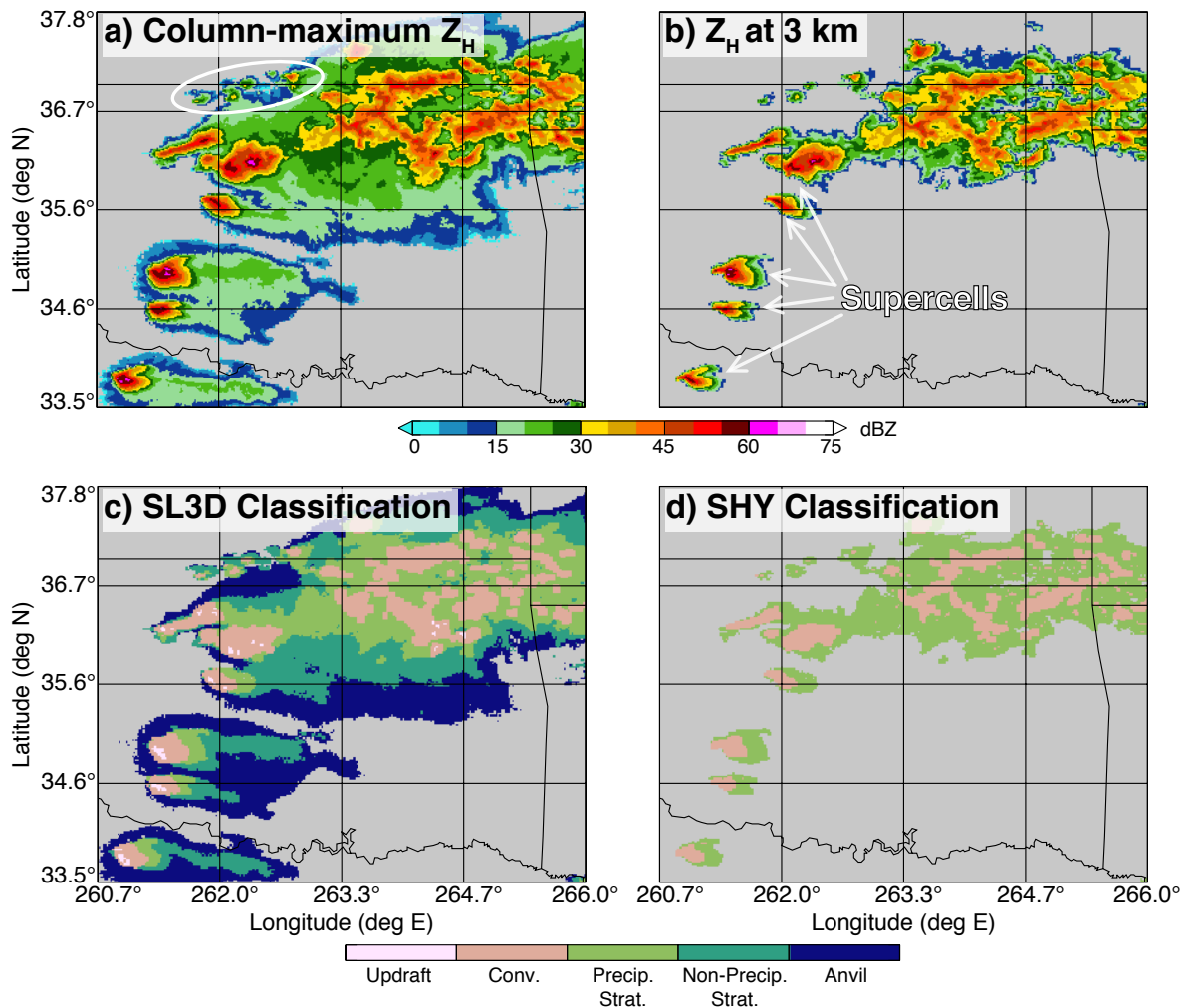


Figure 17: Maps of (a) column-maximum  $Z_H$ , (b)  $Z_H$  at 3 km altitude, (c) SL3D classification, and (d) SHY classification for a collection of supercell storms and an MCS over Oklahoma on 23 May 2011 at 2325 UTC. The white ellipse in (a) encloses weaker convection that is discussed in the text.

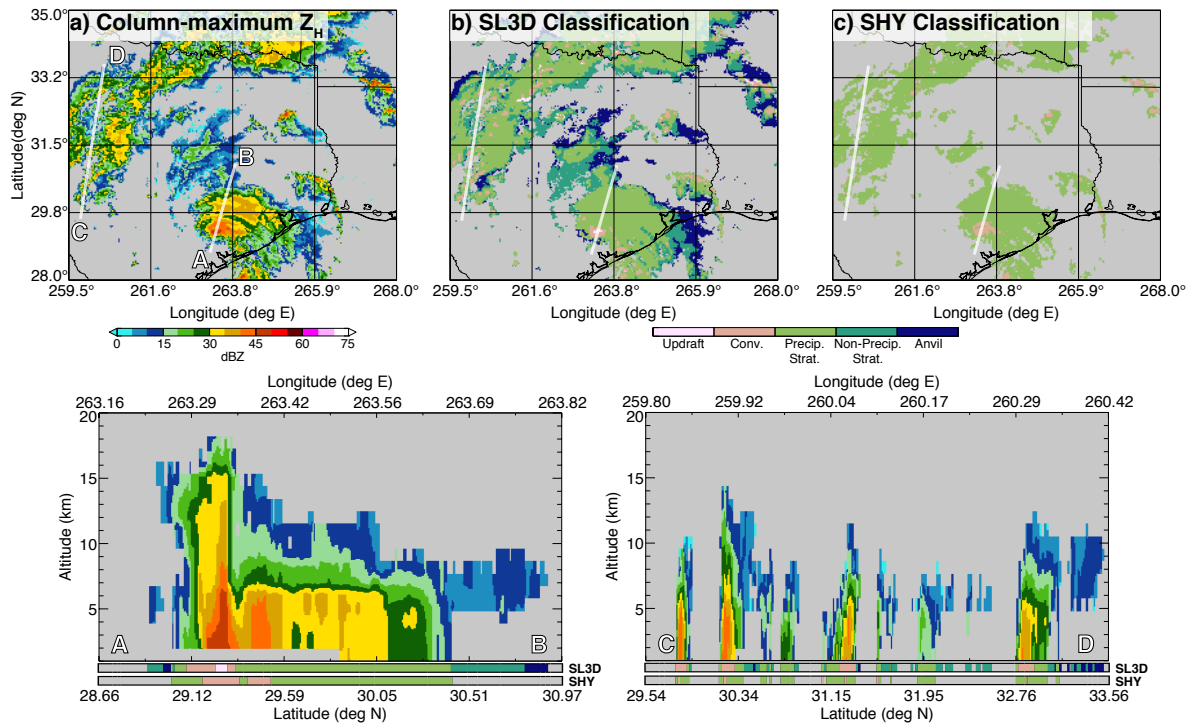


Figure 18: Maps of (a) column-maximum  $Z_H$ , (b) SL3D classification, (c) SHY classification and vertical cross-sections of  $Z_H$  following the thick lines labeled A–B and C–D for Tropical Storm Bill in southeast Texas and additional nearby precipitation in Arkansas, Louisiana, Oklahoma, and Texas on 17 June 2015 at 0000 UTC. The thick colored lines at the base of each cross-section show the corresponding SL3D and SHY classifications.

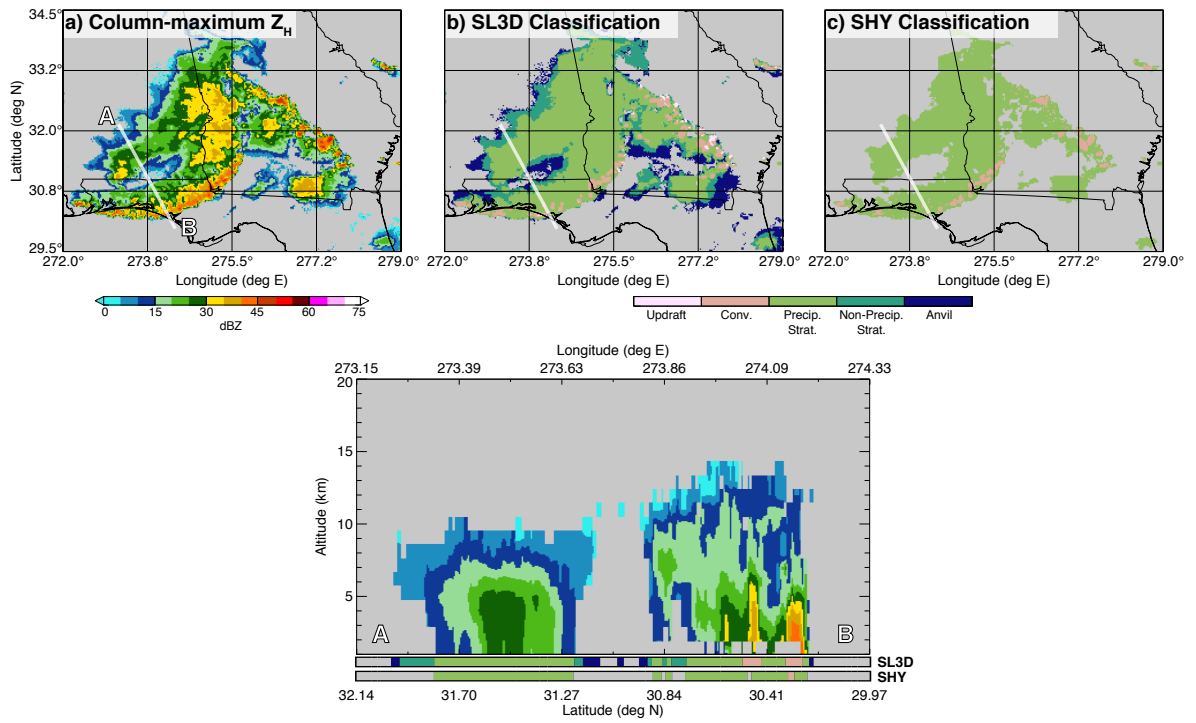


Figure 19: Maps of (a) column-maximum  $Z_H$ , (b) SL3D classification, (c) SHY classification and a vertical cross-section of  $Z_H$  following the thick line labeled A–B for an MCS located over Alabama, Florida, and Georgia on 24 July 2013 at 0000 UTC. The thick colored lines at the base of the cross-section show the corresponding SL3D and SHY classifications.

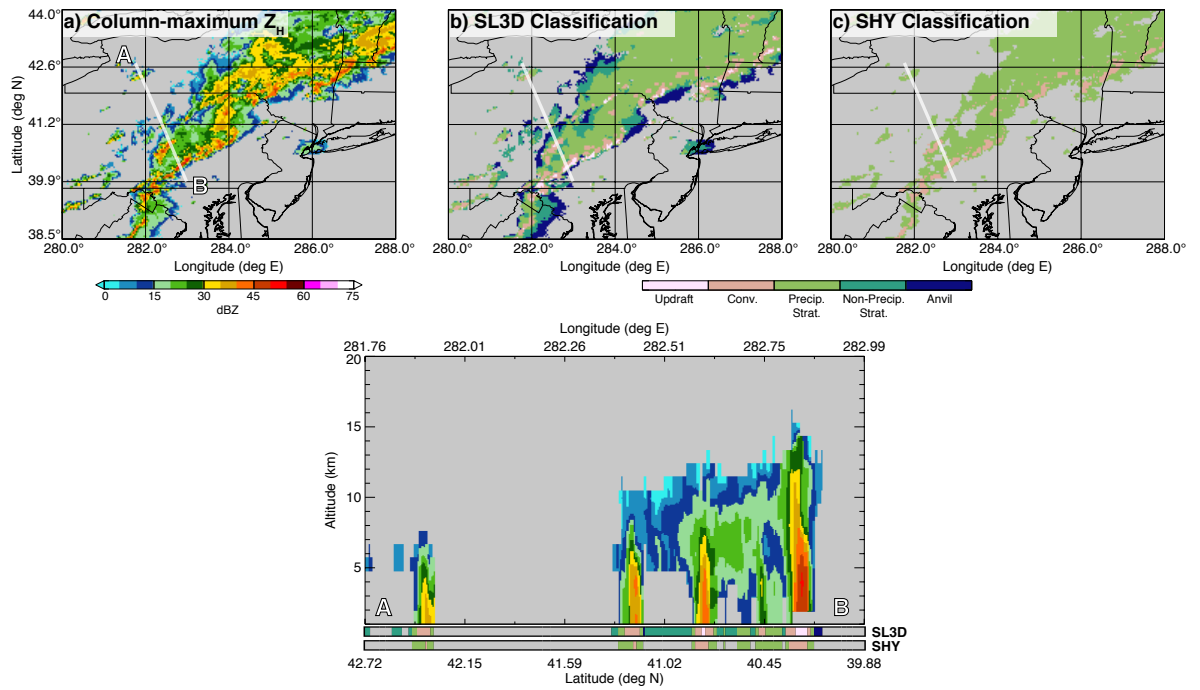


Figure 20: As in Figure 19, but for scattered weak convection and an MCS located primarily over New York and Pennsylvania on 25 June 2014 at 2300 UTC.

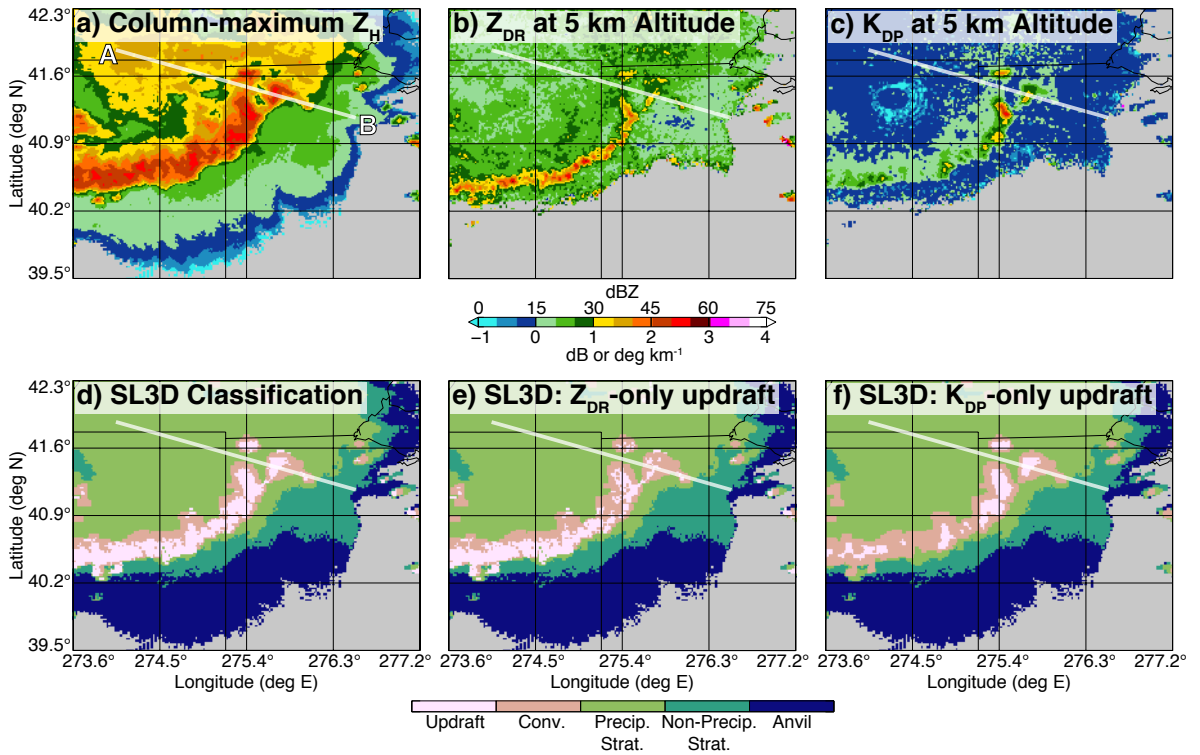


Figure 21: Maps of (a) column-maximum  $Z_H$ , (b)  $Z_{DR}$  at 5 km altitude, (c)  $K_{DP}$  at 5 km altitude, (d) SL3D classification, (e) SL3D classification with  $Z_{DR}$ -only updraft classification, and (f) SL3D classification with  $K_{DP}$ -only updraft classification for an MCS located in northern Indiana and Ohio on 13 June 2013 at 0330 UTC. The thick lines on each map show the location of the vertical cross-sections in Fig. 22.

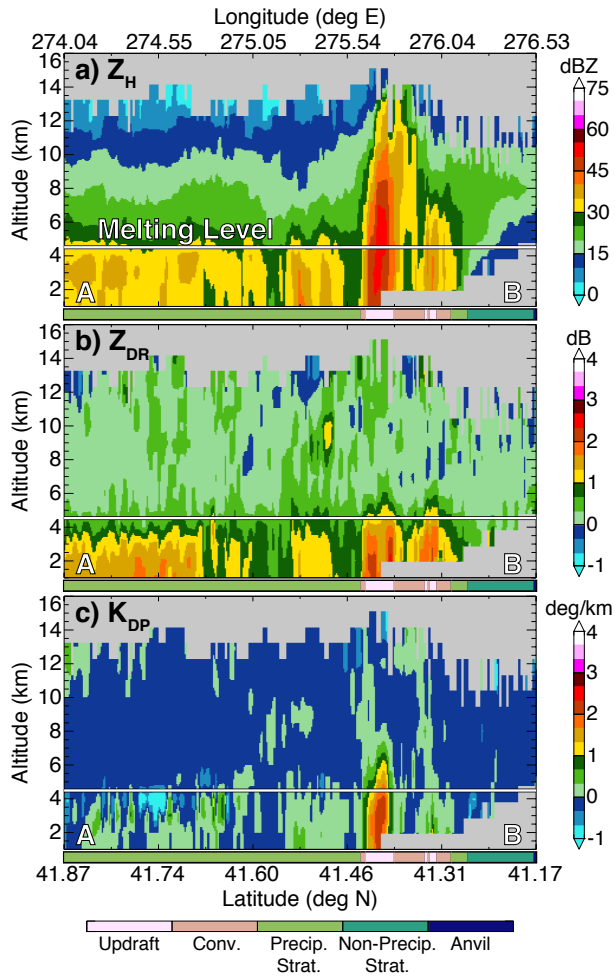


Figure 22: Vertical cross-sections of (a)  $Z_H$ , (b)  $Z_{DR}$ , and (c)  $K_{DP}$  along the line in Fig. 21, from A (left) to B (right). The thick horizontal line in each cross-section represents the altitude of the environmental melting level and the thick colored line at the base of each cross-section shows the corresponding SL3D classification.



## CHAPTER 4

### RETRIEVALS OF CONVECTIVE DETRAINMENT HEIGHTS USING GROUND-BASED RADAR OBSERVATIONS

#### 4.1 Introduction

Mass exchange between the upper troposphere and lower stratosphere changes the chemical composition, radiative properties, and distribution of greenhouse gases in the atmosphere, which has significant implications for climate studies (e.g., Ramaswamy et al., 1992; Holton et al., 1995; Stohl et al., 2003). It is generally accepted that large-scale transport mechanisms such as isentropic transport from the tropical troposphere and Rossby wave breaking are responsible for the majority of mass exchange between the stratosphere and troposphere, with small-scale features such as deep convection contributing substantially less mass. Nevertheless, deep convection has the ability to rapidly and efficiently transport boundary layer mass to the upper atmosphere (e.g., Pickering et al., 1988; Mullendore et al., 2005). Convection can transport mass in minutes to hours, as compared to days for extratropical cyclones and weeks or months for turbulent diffusive processes (Dickerson et al., 1987; Sigmond and Sigmond, 2000). Mass can be transported into the upper troposphere, and in many cases, convection has been observed to penetrate the tropopause and directly inject mass into the stratosphere (e.g., Poulida et al., 1996; Fischer et al., 2003; Hegglin et al., 2004; Homeyer et al., 2014).

Both model simulations and in-situ measurements reveal that air transported by convection can be relatively undiluted (e.g., Ström et al., 1999; Mullendore et al.,

2005). Injection of polluted boundary layer directly into the upper troposphere and lower stratosphere can have significant chemical impact as free tropospheric air has a much different chemical composition than the boundary layer air. Depending on whether boundary layer air is transported into the upper troposphere or is able to reach the lower stratosphere can have important yet differing radiative, climatological, and/or health impacts.

Unfortunately, it is still difficult to identify the altitude to where mass is transported to. Retrievals of the height of mass transport have been determined from aircraft measurements (e.g., Pickering et al., 1996), satellite measurements (Takahashi and Luo, 2012; Takahashi et al., 2017), multi-Doppler observations (e.g., Mullendore et al., 2013), and modeling studies (e.g., Barth et al., 2007; Bigelbach et al., 2014). While invaluable, aircraft measurements are limited temporally, cannot continuously sample every region of storm outflow, and generally are only included in field campaigns. Satellite measurements are too coarse spatially and/or temporally to be used reliably for assessing three-dimensional cloud-scale properties, and generally require thermodynamic assumptions about the vertical structure of the atmosphere. Multi-Doppler analyses require rigorous processing techniques and also typically rely on field campaigns as only a few locations are setup for such observations. While modeling efforts are useful in understanding how mass is transported and are able to provide three-dimensional detail into transport processes, the chemical transport models are largely unconstrained by observations and have a large uncertainty regarding the height of transport. The uncertainty in these models is a combination of uncertainty in both the chemical processes and convective dynamics.

Due to the limitations in height retrievals, the level of neutral buoyancy (LNB) from parcel theory has been commonly utilized to determine the height of convective detrainment. Parcel theory describes the ascent path and available potential energy

of an air parcel initially chosen using the atmospheric properties near the surface. The LNB is defined as the level at which the density of a positively buoyant air parcel is equal to that of the environment. However, parcel theory does not encompass parcel variability (spatial or temporal), ignores hydrometeor loading, perturbation pressure forces, and most importantly does not include effects owing to entrainment and mixing. Entrainment dilutes the parcel by mixing in cooler, drier environmental air resulting in reduced parcel buoyancy. Therefore, deep convection typically does not detrain at LNB but in actuality detrain below it. In certain cases, the actual detrainment level can be lower than the LNB by 5 km or more (Mullendore et al., 2013). The height of detrainment as determined by parcel theory is typically accepted as the theoretical maximum height a parcel can reach.

To avoid the limitations in identifying the detrainment height with previous methods, Mullendore et al. (2009) showed that profiles of bulk dynamic detrainment retrieved from dual-Doppler analyses coincided well with the location of the anvil visible in the radar reflectivity field. Furthermore, Mullendore et al. (2009) noted that the peak in total ice water content (IWC) of the anvil coincided well with the level of maximum horizontal divergence (i.e., vertical convergence), which they termed the level of maximum detrainment (LMD). Carletta et al. (2016) used this knowledge in effort to develop a procedure that could objectively identify the LMD, and coupled a radar classification scheme from Feng et al. (2011, based on Steiner et al. (1995)) to identify suitable anvil near convection. After analyzing several dual-Doppler cases, they concluded that radar-based detection of the LMD is promising and typically accurate within 2 km; however, they noted several limitations: developing convection lacks adequate anvil, detection can be limited in complex storm clusters where convective elements are embedded in deep stratiform cloud, and sufficient radar coverage is required aloft. Furthermore, they used a strict threshold radar echo stratification

schemed that utilized only low-level echo at one height, which resulted in misclassified echo aloft.

In order to improve our understanding of convective mass detrainment and constrain model simulations, more frequent and easily obtainable observations are needed. In this study, the methodology of Mullendore et al. (2009) and Carletta et al. (2016) is built upon to determine the observed detrainment heights for convection across four regions in the United States: Northern Plains, Southern Plains, Northeast and Southeast. Seven years of hourly high-resolution volumetric radar composites for the months of May and July are coupled with a three-dimensional radar-echo classification algorithm to objectively identify convection and convectively-generated anvil. The retrieved LMD heights for different convective morphologies are examined to determine if there is a height dependence on convective mode.

## 4.2 Data

### 4.2.1 Radar Composites

Radar observations are composited following the procedure in section 3.2. Composites are used for every hour for the months of May and July, from 2004 to 2010. Radar observations are analyzed between  $25^{\circ}\text{N}$  and  $49^{\circ}\text{N}$  latitude and between  $105^{\circ}\text{W}$  and  $70^{\circ}\text{W}$  longitude (23). The analysis domain is split into four regions: North-Central (NC), South-Central (SC), Northeast (NE), and Southeast (SE). The  $37^{\circ}\text{N}$  parallel and  $87.5^{\circ}\text{W}$  meridian demarcate the North/South and Central/East regions, respectively.

### 4.2.2 Model Reanalysis

The Interim European Centre for Medium-range Weather Forecasts (ECMWF) Reanalysis (ERA-Interim Dee et al., 2011) data is used to identify the tropopause height across the analysis region (further described in section 4.3.4). The native ERA-Interim data has a horizontal grid spacing of  $\sim 80$  km on a vertical grid containing 60 levels stretching from the surface to 0.1 hPa, with a vertical grid spacing of  $\sim 0.25$  km near the surface, decreasing to  $\sim 1$  km at 10 km, and  $\sim 2$  km at 16 km.

## 4.3 Determining Radar-based LMD

### 4.3.1 Anvil Proxy Method

To identify the LMD, the convectively-generated anvil is used as a proxy for the dynamic detrainment envelope as in Mullendore et al. (2009) and Carletta et al. (2016). The radar reflectivity of the anvil is used to determine the IWC by

$$IWC = (8.0 * 10^{-3})(Z_e + 6.7)^{0.61} \quad (4.1)$$

where  $Z_e$  is the equivalent radar reflectivity factor (Leary and Houze, 1979). The IWC is horizontally integrated to determine the total IWC present at each altitude. The height of the maximum in total IWC corresponds to the LMD.

The LMD is found for every precipitating storm cell for each hour, if the precipitating cell contains an identified deep convective core and if adequate anvil is sampled near the convective source. Only anvil within 20-km of an identified convective core or updraft is used for the analysis. The 20-km threshold follows Mullendore et al. (2009) and was verified by a sensitivity study to perform well when applied to the radar data utilized by this study (not shown). For an LMD retrieval

to occur, there must be at least 5 anvil grid squares present at one height and at least 25 total anvil grid squares sampled within the 20-km radius to ensure adequate anvil is sampled. Isolated anvil pixel that are not adjacent to any other anvil pixels (horizontally and vertically) are ignored. Identification of precipitating storm cells, convective cores, and anvil is determined by the SL3D algorithm (discussed in section 4.3.2).

The LMD retrievals are determined for storms that occur during the months of May and July, as both months are characterized by different environments. May is a more transition period and is typically associated with more strongly forced convective systems and stronger upper level dynamical support, in part due to the location of the jet stream (e.g., Bigelbach et al., 2014) while July typically contains a warmer, more subtropical environmental in the southern analysis regions. Retrievals are also characterized by morphology (discussed in section 4.3.3) to determine if LMD heights are different between convective modes. Lastly, retrievals are subset by region (i.e., NC, SC, NE, SE) to see if there is regional impact on LMD heights.

#### **4.3.2 Radar Echo Stratification**

The Storm Labeling in 3-Dimensions (SL3D Starzec et al., 2017) algorithm discussed in chapter 3 is used to objectively stratify radar echo into four categories: convection, precipitating stratiform, non-precipitating stratiform, and anvil. SL3D utilizes volumetric radar data to stratify three-dimensional radar echo primarily based on storm height, depth, and intensity. In short, the convective classification encompasses precipitation that is directly generated by convective motions (i.e., updrafts) and is identified by columns of enhanced reflectivity extending vertically into the atmosphere. The precipitating (non-precipitating) stratiform category consists of mixed-phased cloud that likely has (does not have) precipitation reaching the surface. The pre-

precipitating (non-precipitating) stratiform regions are identified by the presence (lack) of radar echo near the surface. The anvil category is defined as non-precipitating radar echo above the freezing level and above 5 km that consists of cloud assumed to contain only ice hydrometeors. For more detailed stratification criteria, see Table 3.

Due to radar downtime, there are instances where low-level data are missing in the reflectivity composites. In regions with poor radar coverage this can result in no data up to 6 km above ground level, which adversely affects the SL3D algorithm. For instance, the SL3D anvil category is defined as reflectivity data present above 5 km with no radar echo below. When a large layer of data up to 5 km is missing, SL3D will still be able to identify convection regions but will stratify all echo around the convection as anvil even though the echo is most likely a stratiform rain region. Including this data would result in very low LMD retrievals of  $\sim 6$  km. To filter out the erroneous classifications due to missing data, if no reflectivity data are present within SL3D convective cores up to 4 km but reflectivity data are present at 5 km or more, the convective cores are disregarded from the analysis and do not have an LMD retrieved. Since the layer of missing data may only be present in a portion of the convective core, convective cores are disregarded if over 20% of the original core is deemed to have missing data. Additionally, if the first anvil pixel is present at 5 or 6 km, but has a reflectivity magnitude of  $> 15$  dBZ (similar to the method used in Carletta et al. (2016)), the entire anvil column is disregarded as it is assumed to have missing data below that would change the classification to precipitating or non-precipitating stratiform.

### **4.3.3 Classification of Storm Morphology**

Precipitating storms are also objectively classified into one of three distinct categories: weak convection, quasi-isolated strong convection (QISC), and mesoscale convective

system (MCS) following a criterion similar to Bigelbach et al. (2014). Bigelbach et al. (2014) define QISC and MCSs as precipitating storms having a maximum reflectivity  $\geq 40$  dBZ, containing a deep convective point, and covering  $< 7000$  km<sup>2</sup> and  $\geq 7000$  km<sup>2</sup>, respectively. Weak convection is defined as precipitating storms with maximum reflectivity  $< 40$  dBZ regardless of size. In Bigelbach et al. (2014), a deep convective point is defined as a column containing vertical velocities of at least  $2$  m s<sup>-1</sup> at  $4$  km and  $5$  m s<sup>-1</sup> at  $8$  km. Since no vertical velocity data is available in this study, the deep convective point definition has been altered to follow the SL3D convective definition that focuses on deep convection and uses the criteria of  $25$  dBZ echo tops  $\geq 10$  km.

#### **4.3.4 Identification of Tropopause Height**

While it is important to know the absolute heights that convection detrains mass to, the height of the LMD in relation to the tropopause height provides more insight into whether mass is potentially being mixed into the stratosphere and allows for better comparison of storms from different regions. Several methods have been previously used to identify the tropopause height in relation to deep convection, including temperature lapse rate, stability, and potential vorticity-based (PV) definitions (e.g., Maddox and Mullendore, 2018, and references therein). While temperature lapse rate and stability definitions typically perform well in identifying the tropopause for sounding data, there are occasional occurrences where both methods are unable to capture the initial tropopause but instead capture the “cold-point” tropopause. This misidentification can result in a high tropopause height bias of up to  $6$  km or more, which introduces a significant low bias in tropopause-relative LMD height retrievals of deep convection. These misidentifications were also seen by Homeyer et al. (2010) and Solomon et al. (2016) who noted that such misidentifications occur most commonly



near the subtropical jet or regions of tropopause folding due to the lower vertical resolution of reanalysis data resulting in an apparent “smoothed” temperature field.

To avoid introducing large errors in tropopause heights, the tropopause is identified using Ertels PV Theorem

$$PV = \frac{1}{\rho} \left[ \left( \frac{\partial v}{\partial x} - \frac{\partial u}{\partial y} \right) + f \right] \frac{\partial \theta}{\partial z} \quad (4.2)$$

where  $\rho$  is density,  $u$  and  $v$  are the horizontal velocity components in the  $x$ - and  $y$ -directions, respectively,  $f$  is the Coriolis parameter,  $\theta$  is potential temperature, and  $z$  is height. The first height with a PVU of  $\geq 2.0$  with no heights having a PVU  $< 1.5$  above it is identified as the tropopause height (where 1 PVU is  $10^{-6} \text{ K m}^2 \text{ k}^{-1} \text{ s}^{-1}$  of PV). PV is calculated on the native ERA-Interim grid; however, because of the coarse grid spacing aloft, the PV field is linearly interpolated to a vertical grid with 250 m spacing ranging from 0 to 20 km to more precisely identify the height that crosses the 2.0 PVU threshold. The representative tropopause height used for each storm is the mean tropopause height found within the convective pixels for that storm as determined by the SL3D algorithm. While convection strongly perturbs the PV field at convective scales (i.e., 1 to 10 km Maddox and Mullendore, 2018), the ERA-Interim data does not resolve convective-scale perturbations due to the coarse grid spacing ( $\sim 80$  km), so PV remains a usable field for this study.

## 4.4 Results

### 4.4.1 Applications of Anvil-based Methodology

An example application of the anvil-based methodology is presented for an intense supercell located over northeastern Nebraska on 13 July 2004 at 00 UTC (Fig. 24). The main storm has reflectivity magnitudes reaching  $\sim 65$  dBZ with the highest echo

tops extending above 18 km (Fig. 24a, c). A few less intense convective cells are visible around the main storm. The SL3D algorithm identifies five convective regions during this time (light brown; Fig. 24b) and an extensive anvil emanating from the storm (blue). Several precipitating regions are identified (yellow contours); however, only the precipitating regions containing convective cores (solid yellow contours) are considered for sampling following the criteria in section 4.3.1. A cross-section through the main storm depicts the long anvil present between 7 and 14 km downstream of the storm and a forward, upstream anvil extending up to 16 km (Fig. 24c). The vertical profile of horizontally integrated IWC of all anvil pixels within 20 km of largest convective core (i.e., storm that is intersected by the magenta line in Fig. 24b) is shown in Fig. 24d. The peak in IWC (and therefore, the radar-derived LMD) is located at 13 km, around 2 km above the tropopause height. The LMD defines the height where the most mass is detrained, but it is clear that the forward anvil has a much wider envelope (Fig. 24c); indicating the large vertical spread of detrainment altitudes observed for different parcels.

#### 4.4.2 LMD Height Retrievals

Applying the methodology results in a total of 3,203,716 precipitating cells being detected, of which 946,381 (29.5% of cells) contain SL3D convective cores. Of these SL3D cores, 157,230 (4.9% of cells or 16.6% of SL3D cores) are considered deep. Application of the anvil-based method results in a final sample size containing 135,890 storms, meaning 86.4% of deep convective cores have adequate anvil to sample at a 20 km distance and a successful LMD retrieval is performed. Table 3 illustrates a breakdown of the number of storms sampled by region, month, and morphology across each year. The total number of storms sampled is greater in the Southern regions, with 65.1% of sampled storms being in either the SC or SE region. Of all sampled

storms, 71.4% occurred in July and 88.0% are of QISC morphology. These sample statistics showcase the large amounts of diurnally driven convection that occur over the southern regions during the summer months. Overall, the anvil-based method has a successful application rate ranging from 84.3 to 89.0% of usable cores when looking at different regions, months, or morphologies, implying the method is not biased towards any of those variables.

After the initial LMD identification, the data undergoes a last round of quality assurance checks to make sure the retrievals are physically consistent. For any particular convective core, if there is only a single height that contained anvil or if the LMD height is found at 6 km (the lowest height that is considered anvil), the LMD retrieval is removed as this is likely due to missing radar data aloft. LMD retrievals are also disregarded if the range between the LMD and anvil top is greater than 5 km or if the anvil top is above 18 km as these are were found to be commonly caused by radar technical issues. The anvil top is considered the top of the IWC envelope.

The distribution of aggregated LMD height retrievals for all convection categorized by the months of May and July are shown in Figure 25. When comparing the absolute LMD heights (Fig. 25a), July has a higher mean LMD than May, denoting that convection detrains the maximum amount of mass higher in July. July storms also have higher maximum LMD heights, reaching up to 15 km. Note that due to the vertical grid spacing of the data (i.e., 1 km), the absolute LMD retrieval outlier points overlay each other except when two heights have the same IWC, in which the average of the two LMD heights is used instead. Even though July storms have a higher mean absolute LMD, the mean tropopause-relative LMD for May storms is higher than for July storms, denoting the May storms typically detrain closer to tropopause (Fig. 25b). There are storms in both May and July than have LMDs at and above the tropopause, with July containing a wider distribution of LMD heights that can reach

up to 2 km above the tropopause. Overall, convection tends to detrain the maximum amount of mass  $\sim 4$  km below the tropopause. The aggregated LMD height retrievals are also categorized by morphology to investigate the differences between MCSs and QISC (Fig. 26). Both the absolute and tropopause-relative mean LMD heights are higher for QISC than MCSs, indicating the QISC more commonly detrain to higher altitudes and closer to the tropopause. QISC also contain a larger spread in tropopause-relative LMD heights and more commonly breach the tropopause. The absolute LMD retrievals for July and QISC look similar as the month of July is dominated by QISC type convection (Table 3).

The aggregated results are subdivided by region and are shown in Figure 27. While all regions contain LMD heights that reach and surpass the height of the tropopause, the NC and NE regions contain LMD heights that have a higher likelihood of breaching the tropopause and have mean LMD heights up to 0.75 km higher than the southern regions. The regional results are further broken down by month and morphology to identify what is contributing to the differences in each region. Figure 28 shows the distributions of tropopause-relative LMD heights for each region for May and July. For May, all regions have relatively similar mean LMD heights with both northern regions (in particular, the NC region) having the highest LMD heights (Fig. 28a). In July, the mean LMD heights for both northern regions increase while the mean LMD heights for the southern regions decrease relative to May (Fig. 28b). The northern regions have notably higher mean LMD heights than the southern regions, with the 50th percentile of northern region LMD heights being closer to the tropopause than the top 25th percentile of the southern region. Both north regions have a pronounced increase in the number of storms that have LMD heights above the tropopause even though the NE region only had two outlier storms reaching or surpassing the tropopause height in May.

Subjectively analyzing several cases, the decrease in mean LMD heights for the southern regions is driven by a large increase in weakly-forced, diurnally driven convection that occurs in the summer months. The SC and SE regions have 97% and 304% more LMD retrievals in July than May, respectively. Similar trends are visible when comparing differences between MCSs and QISC by region (Fig. 29). Overall, MCSs have lower mean LMD heights than QISCs for all regions, especially in the northern regions. Only a handful of MCSs across the several years analyzed have LMDs at or above the tropopause, while QISCs more commonly breach the tropopause. A subjective analysis into the QISCs with the highest LMD heights reveals that most of these storms are easily identifiable by their radar characteristics as supercells. This result follows on previous studies showing supercells detrain at higher altitudes in both models (Mullendore et al., 2005; Bigelbach et al., 2014) and observations (Mullendore et al., 2013). The storm that has the highest tropopause-relative LMD is the supercell storm depicted in Figure 24.

## 4.5 Discussion

The findings show that on average, storms in May detrain most of their mass closer to the tropopause than storms in July, and QISC storms have higher tropopause-relative detrainment heights than MCSs. These observational results match the general conclusions of the Bigelbach et al. (2014) modeling study, who used high-resolution Weather Research and Forecasting (WRF) forecasts of convection in the Southern Great Plains to determine the detrainment heights by using simulated vertical velocity values. There are, however, some differences between the details of both studies. Bigelbach et al. (2014) had almost no storm LMDs surpassing the tropopause while many such storms were sampled in this study (particularly the north regions). Overall, the mean tropopause-relative LMD heights for May were higher in July but the

highest tropopause-relative LMD heights were more commonly observed in July (Fig. 26), which did not match Bigelbach et al. (2014). However, if results are constrained to only the SC region (better resembling the modeling domain used in Bigelbach et al. (2014)), the highest tropopause-relative LMD heights occur in May rather than July (Fig. 28) matching the Bigelbach et al. (2014) results. The decrease in mean LMD heights from May to July is also visible if focusing on the SC region, albeit the magnitude of decrease is much greater in Bigelbach et al. (2014) ( $\sim 2$  km decrease vs 1 km in this study; Fig. 28). Comparing these studies showcases the importance in investigating the regional differences in storm detrainment heights.

While the LMD shows the height of maximum mass detrainment, mass is still being detrained above the LMD with the most unstable and/or least mixed parcels detraining near the top of the anvil (Carletta et al., 2016); therefore, investigating anvil tops helps identify the maximum height that mass detains to and provides additional information for when the LMD heights are biased low (discussed in the next section). Figure 30 shows the tropopause-relative heights subdivided by region and month for the height of anvil tops. Overall, the trends between mean anvil top detrainment heights follow similar trends when using the LMD heights (Fig. 28). The detrainment heights in May are relatively similar between regions and July detrainments heights increase for the north regions and decrease for the south regions. The mean anvil top detrainment heights range from  $\sim 0.75$  to 1.25 km below the tropopause in May, as compared to  $\sim 4$  km below the tropopause for the LMD heights (comparing Fig. 28 and Fig. 30). A significant number of storms have anvil tops several kilometers above the tropopause, reaching up to 6 km above the tropopause for the deepest convective cores sampled.

A similar anvil top analysis focusing on morphology is shown in Figure 31. The mean tropopause-relative anvil top height is higher for MCSs than QISC for

all regions even though the mean LMD height was consistently higher for QISCs (Fig. 29). These results need to be further investigated as they imply that while on average the greatest amount of mass is detrained lower in MCSs than QISC, MCSs typically have a wider detrainment envelope. These results may also be capturing the large variability observed in several cases of MCS dual-Doppler derived detrainment heights by Mullendore et al. (2013). QISC still have a larger spread of anvil-top detrainment heights and contain the highest detrainment heights overall, which are not surprisingly the same storms that have the highest LMD heights. The differences between MCSs and QISC also show the importance of morphology on the LMD and detrainment heights. Further detailed analysis needs to be done on why supercells have higher detrainment heights relative to other QISC and MCSs, and why a larger variability in MCS detrainment heights is present. Only seven MCSs have LMD at or above the tropopause and a subjective analysis of these MCSs reveals that majority are supercells and other strong isolate cells transitioning to linear convection.

The detrainment envelope depicts the altitudes where parcels of air are detraining from a convective system, but also provides information on the buoyancy and relative dilution experienced by parcels rising through the updraft. A parcel that may be near the updraft edge experiences more mixing and entrainment of environmental air, resulting in a reduction of the parcel's buoyancy and hence, reduces the parcel's detrainment height; however, mixing also dilutes the parcel. Parcels that experience less entrainment (so called "lucky" parcels) are more buoyant and likely detrain to higher altitudes, but are also less diluted. Therefore, although most mass is commonly detrained below the tropopause as visible by the mean LMD heights, the parcels that reach the highest altitudes are likely less diluted and contain a higher concentration of polluted boundary layer air than the parcels that detrains at the LMD and below it (i.e., where most mass is detrained). This implies that although

fewer parcels penetrate the tropopause, their effect on altering the chemistry of the UTLS may still be substantial relative to the large number of (more diluted) parcels detraining at the LMD. More research is required to investigate the relationship between detrainment altitudes and parcel dilution to determine the relative impact of the most unstable and undiluted parcels.

#### 4.5.1 Limitations

There are some inherent limitations to utilizing the anvil-proxy method. Only storms that are actively producing a notable anvil can be sampled, which excludes developing convection and storms that are embedded within an extensive stratiform rain region and have no pristine anvil to sample. Storms that are developing into pre-existing anvil will have their LMD retrieval incorrectly attributed to the height of the pre-existing anvil (e.g., the cell north of the large supercell in Fig. 24), although this is somewhat limited by focusing only on the deepest convection as weaker convection is generally excluded from the analysis. Lastly, when several deep convective clusters are near each other, anvil may be sampled from multiple convective sources and not just from the convective core being analyzed, which can be sensitive to the anvil search radius used.

Of particular note, is the low bias in LMD estimates. The LMD heights in this study likely contain a low bias that is dependent on the anvil search radius. The 20 km anvil search radius was chosen in order to maximize both the accuracy of the retrieved LMD height and the number of convective objects that contribute to the LMD retrieval. Due to varying environmental conditions and internal dynamic processes, convection may produce limited forward anvil or anvil that spans up to 20 km or more away from the convective source. For the anvil-based LMD retrieval to work properly, adequate anvil near the convective source must be sampled; however,



sampling anvil that is too far from the convective source may be detrimental. For example, if the distance threshold is shorter (e.g., 10 km), the accuracy of the LMD retrieval should be improved since only the anvil closest to the convective core is being sampled; however, there may be no or limited anvil present in the sampling distance (i.e., five grid squares), thereby reducing the overall detection rate. Conversely, if the distance threshold is larger (e.g., 40 km) the amount of anvil sampled is increased and a larger sample size of anvil pixels is attained; however, at larger distances the anvil may begin to slope downward due to aggregation of ice hydrometeors, potential for sampling anvil from differing convective source increases, and downstream stratiform anvil becomes included which leads to less accurate (i.e., low-biased) LMD retrievals.

An example of a low-biased LMD retrieval is presented for a single large storm cluster in Figure 32. The storm cluster contains several convective elements of which some are embedded within a stratiform rain region (Fig. 32a). The storm cluster is producing a very large anvil (blue; Fig. 32b) resulting in ample anvil to sample within 20 km of the convective cores (cyan outline; Fig. 32b). Application of the anvil-proxy methodology on the deepest convective element in the southwestern side of the storm cluster returns an LMD of 12 km. A cross-section through the forward anvil adjacent to the convective core shows that the anvil is present between 9 and 17 km (Fig. 32c), where subjectively the LMD would be selected as being higher than 12 km. A cross-section along the south side of the storm cluster shows the anvil sloping down as distance away from the convective course increases (Fig. 32d). Sampling a large portion of the descending anvil lowers the LMD retrieval height. A similar scenario is observed in Fig. 24c, where the forward anvil is seen extended 1 to 2 km above the retrieved LMD height.

When all the limitations and biases are combined, the anvil proxy method likely depicts detrainment heights that are lower than the actual detrainment height,

especially when considering that S-band radars cannot detect the entire anvil; however, it provides a way to collect a very large observational dataset of midlatitude convective detrainment heights that that does not currently exist and can be used to help constrain model simulations. The low bias also means that the observed convective LMDs are higher than the radar-derived, meaning convection likely detrains mass higher than the heights determined in this study. The methodology may be further improved by incorporating dual-polarized radar data, which would enable the use of SL3Ds objective updraft identification and provide more information for a more detailed IWC calculation and estimation of hydrometeor fall speeds to help account for the low bias.

#### 4.6 Summary and Conclusions

Seven years of hourly ground-based radar observations for the months of May and July are evaluated to determine the level of maximum (mass) detrainment (LMD) by convection for four different regions: north-central, south-central, northeast, and southeast United States. Radar observations are objectively stratified by the SL3D algorithm to identify regions of deep convection and convectively-generated anvil. Anvil near active deep convection is sampled and used as a proxy for the detrainment envelope, where the maximum in the radar-derived ice water content of the anvil represents the LMD. The methodology is regionally inspecific and can be used to study convective detrainment altitudes regardless of location as long as adequate radar observations are present.

Analysis of mean LMD heights shows that July storms tend to have a higher absolute detrainment height than May storms; however, May storms have a higher tropopause-relative detrainment height indicating that on average, May storms are more likely to detrain closer to the tropopause than July storms. Both months contain

individual storms that have LMD heights above the tropopause, but July contains the highest LMD heights extending up to 2 km above the tropopause and a higher frequency of storms reaching the tropopause. When categorized by morphology into mesoscale convective system (MCS) or quasi-isolated strong convection (QISC), QISC are found to have both higher absolute and tropopause-relative LMD heights and more commonly have storm LMD heights above the tropopause. A subjective investigation into the cases with the highest LMD heights reveals that most exhibited the radar characteristics of supercells, supporting the findings of Mullendore et al. (2013) case analysis.

A regional categorization found that both northern regions had higher mean tropopause-relative LMD heights than the southern regions, regardless of month or morphology. The finding that QISC have higher mean tropopause-relative LMD height than MCSs was true for all regions; however, there were regional differences between May and July. The mean tropopause-relative LMD height increased in July for the northern regions but decreased for the southern regions, relative to May. The decrease in the LMD heights in the southern regions is due to a large amount of diurnally driven convection present in the summer months, decreasing the mean LMD heights.

Lastly, while the LMD showcases the height where the maximum mass is being transported to, there is still mass being transported above the LMD. To account for mass transport above the LMD, the anvil top is used as a proxy for the top of the detrainment envelope. Results showed that there are a substantial number of storms with mass being transported well above the unperturbed tropopause (up to 6 km). The mean tropopause-relative anvil top heights for MCSs were found to also be slightly higher than QISC for all regions, even though the mean LMD height for MCSs was lower, which suggests that MCSs may have a wider detrainment envelope.

More research needs to be done investigating morphological differences between MCSs, supercells, and daily convection and their impacts on detrainment altitudes.

Although the detrainment heights are likely biased low, this study built a large dataset of observed convective detrainment heights in the midlatitudes that was previously absent to provide an idea of aggregated detrainment altitudes and to help constrain model simulations. If combined with mass flux estimates, this statistical database can be used to approximate the amount of mass of different chemical species that is being transported into the troposphere and stratosphere. The observed variability present in convective detrainment altitudes for differing morphology has important implications on parameterizations and modeling of mass transport as all convective modes cannot be treated equally. For example, supercells are able to penetrate and transport mass deeper into the UTLS, but MCSs have a wider range of mass detrainment heights, which changes the vertical distribution of transported mass. The observed regional variability in LMD heights further demonstrates the importance of convective morphology, as the diurnally-driven convection notably reduced the mean LMD heights in the southern regions of the United States. The difference in detrainment heights across May and July also indicates that seasonal differences need to be accounted for when estimating long term transport statistics or influences of transport on climate.

Table 3: The total number of storms sampled (i.e, LMD retrievals performed) for each year of the analysis period categorized by region, month, and morphology.

	Region			Month			Morphology	
	North Central	South Central	Northeast	South Central	Southwest	July	MCS	QJSC
2004	4347	5537	3162	6273	5712	13607	2269	17050
2005	3839	6506	2538	5737	3763	14857	1924	16696
2006	4927	6969	2751	6144	5825	14966	2002	18789
2007	5002	9033	2094	6114	6198	16045	2332	19911
2008	4730	5638	1758	5724	3897	13953	2471	15379
2009	3724	6037	1708	6022	6768	10723	2708	14783
2010	4496	6997	2360	5723	6714	12862	2570	17006
Total Sampled	<u>31065</u>	<u>46717</u>	<u>16371</u>	<u>41737</u>	<u>38877</u>	<u>97013</u>	<u>6276</u>	<u>119614</u>
% Sampled	22.9	34.4	12.0	30.7	28.6	71.4	12.0	88.0

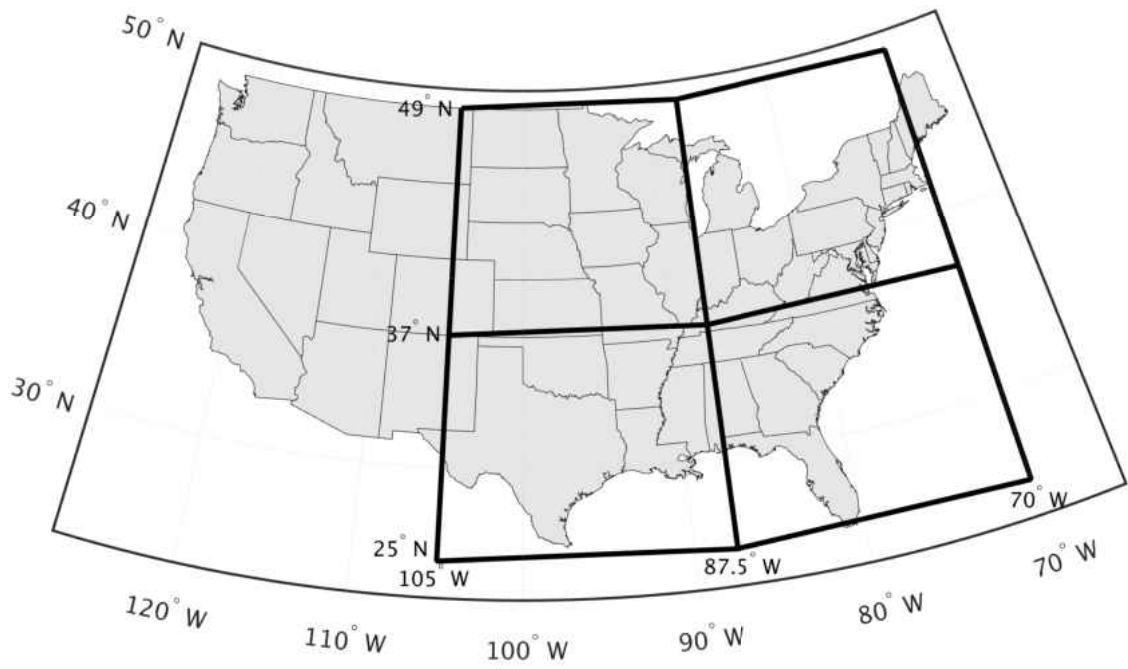


Figure 23: The four analysis regions demarcated by the 37°N parallel and 87.5°W meridian.

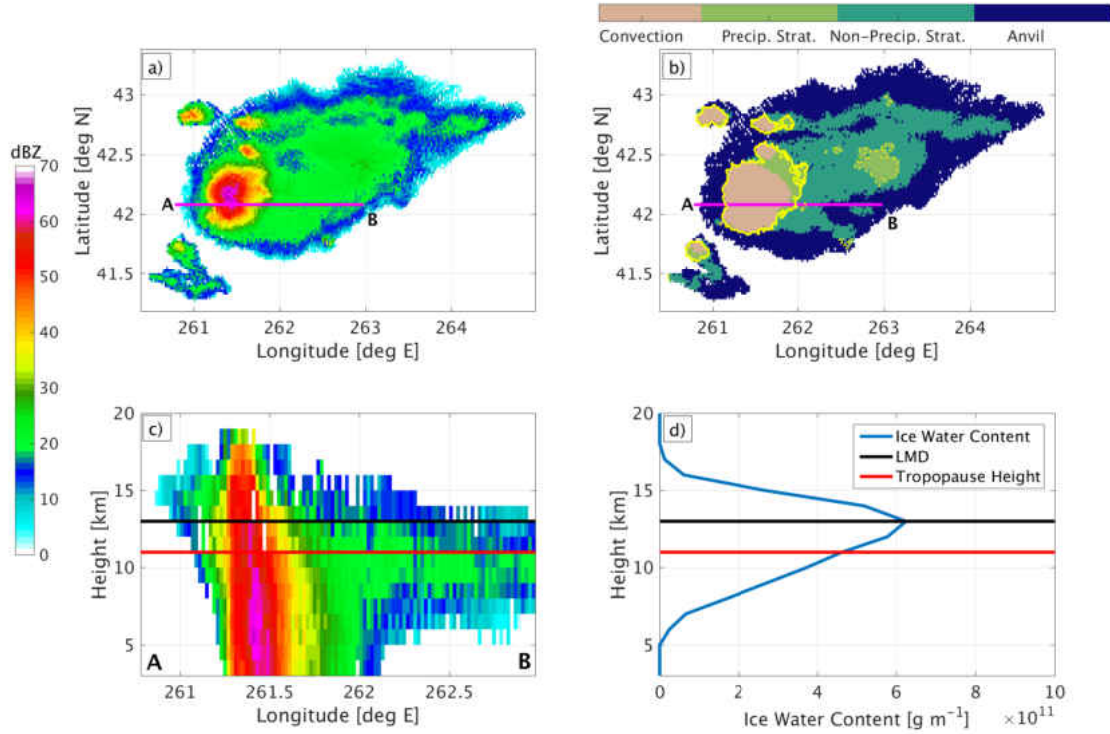


Figure 24: The a) composite reflectivity, b) SL3D classification, c) vertical cross-section of reflectivity following A to B, and d) horizontally integrated IWC for a supercell located in Nebraska on 13 July 2004 at 00 UTC. The yellow lines in b) denote identified precipitating objects, where the thick yellow lines are the objects that match the LMD retrieval criteria. The black line in c) and d) denotes the height of the radar-derived LMD using the anvil-proxy method and the red line denotes the tropopause height.

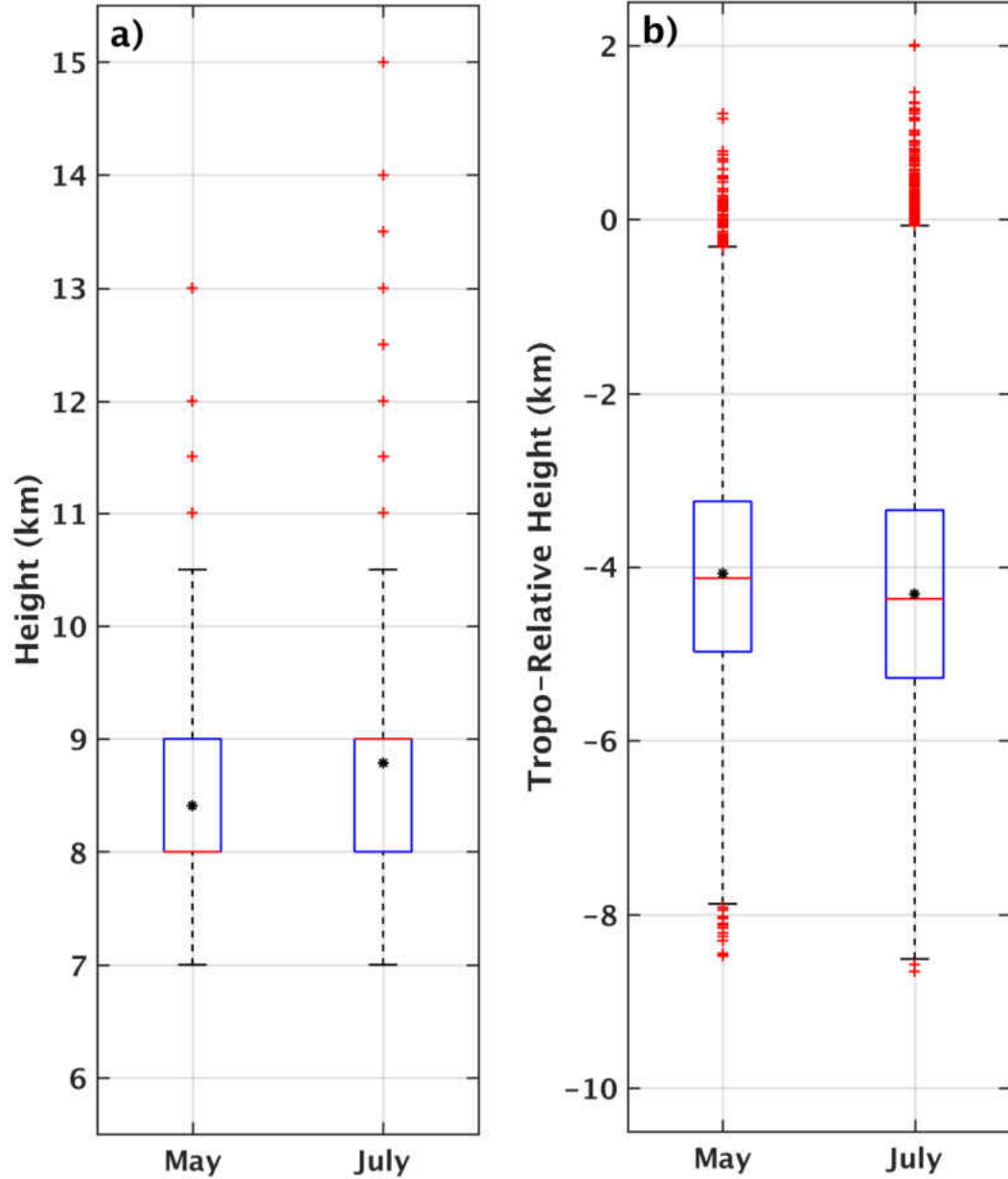


Figure 25: The boxplot distribution of a) retrieved LMD heights and b) tropopause-relative LMD heights across the entire analysis period for the months of May and July. The black asterisk is the mean, the horizontal red line is the median, top and bottom of the boxes are the 75th and 25th percentiles, respectively, the whiskers are three standard deviations from the mean, and the outliers are red crosses.



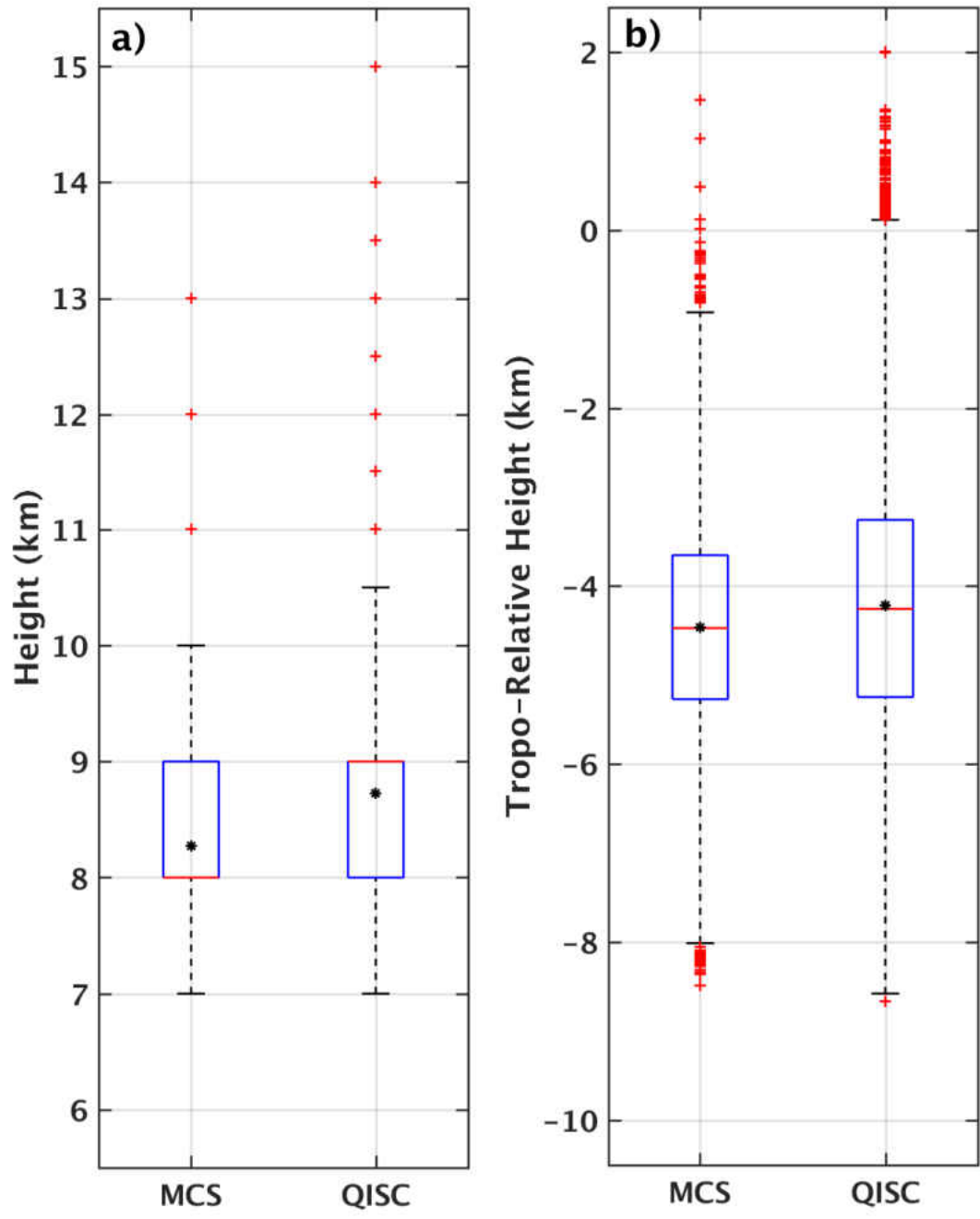


Figure 26: As in Figure 25, except categorized by morphology.

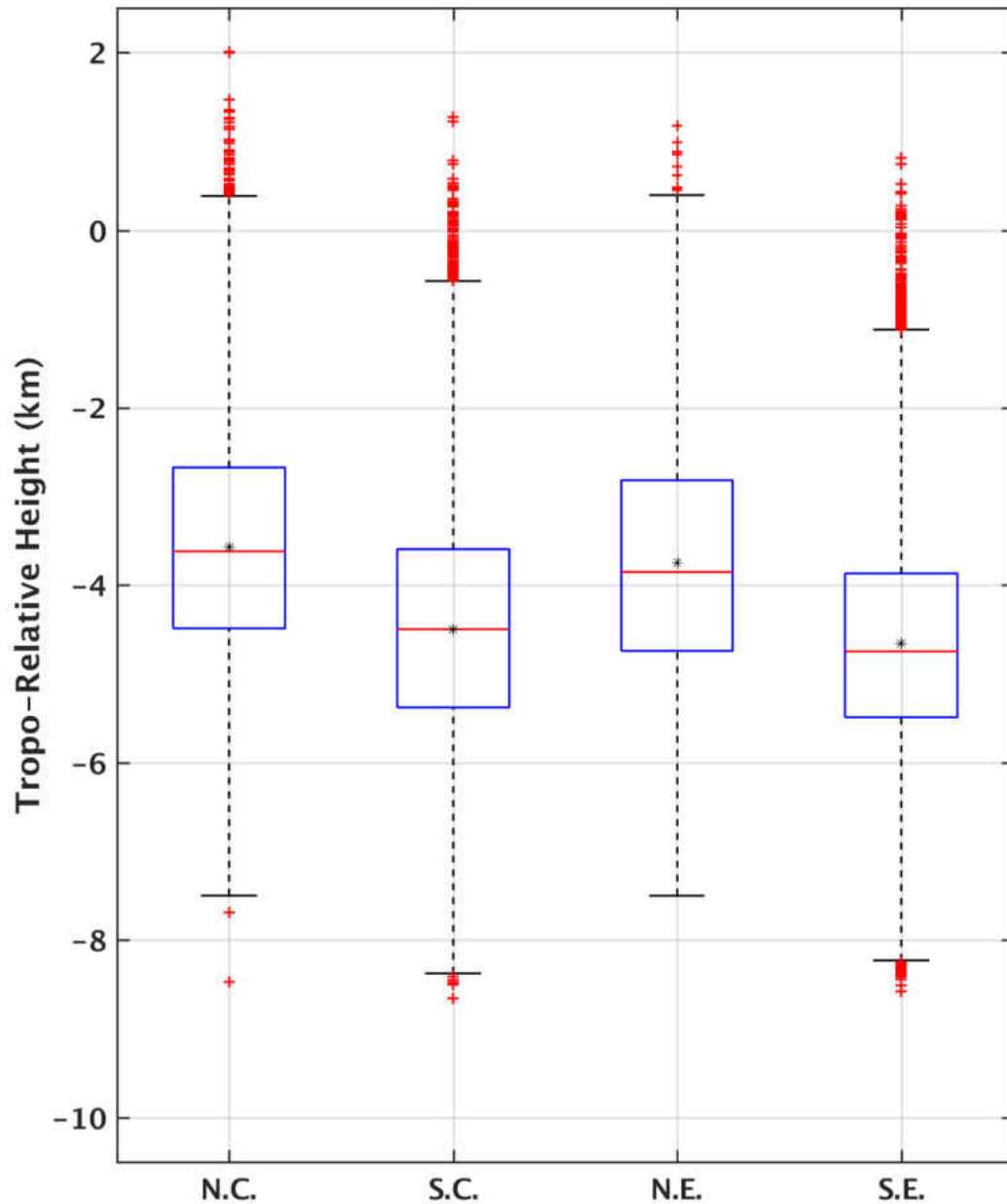


Figure 27: The tropopause-relative LMD height categorized by the four analysis regions: North-Central (NC), South-Central (SC), Northeast (NE), and Southeast (SE). The black asterisk is the mean, the horizontal red line is the median, top and bottom of the boxes are the 75th and 25th percentiles, respectively, the whiskers are three standard deviations from the mean, and the outliers are red crosses.

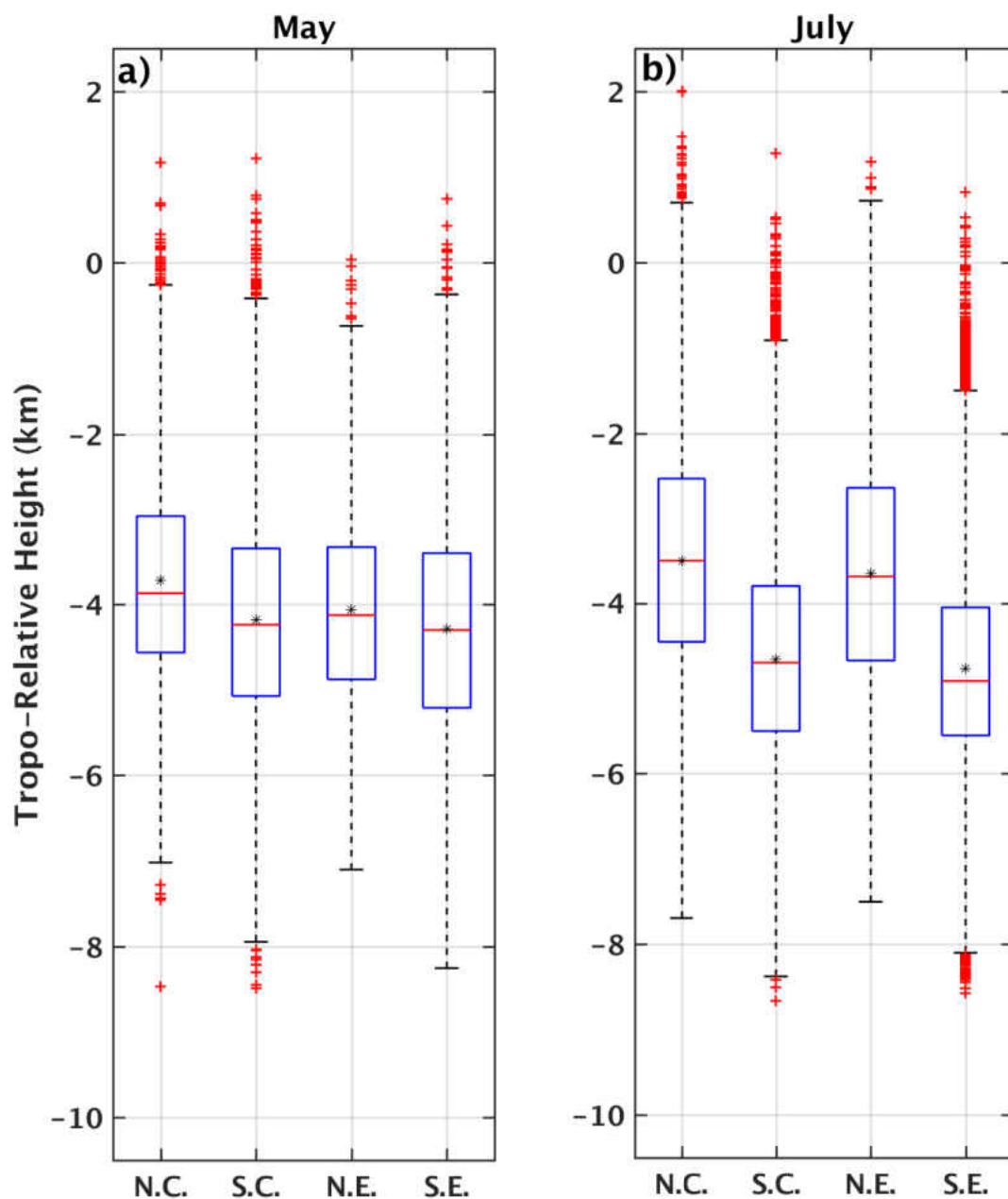


Figure 28: The tropopause-relative LMD height categorized by the months of a) May and b) July for the four analysis regions. The black asterisk is the mean, the horizontal red line is the median, top and bottom of the boxplots are the 75th and 25th percentiles, respectively, the whiskers are three standard deviations from the mean, and the outliers are red crosses.

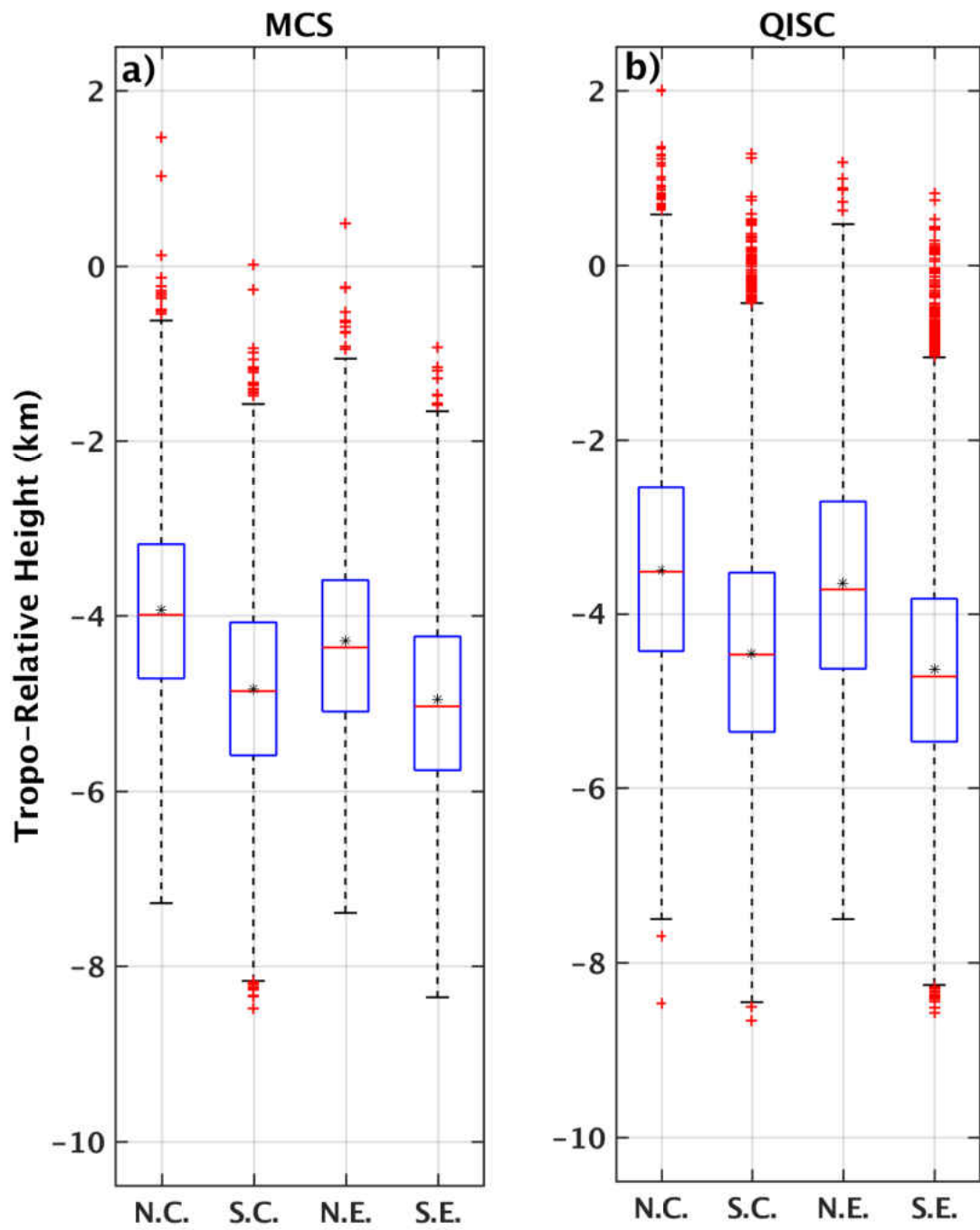


Figure 29: As in Figure 28, except categorized by morphology.

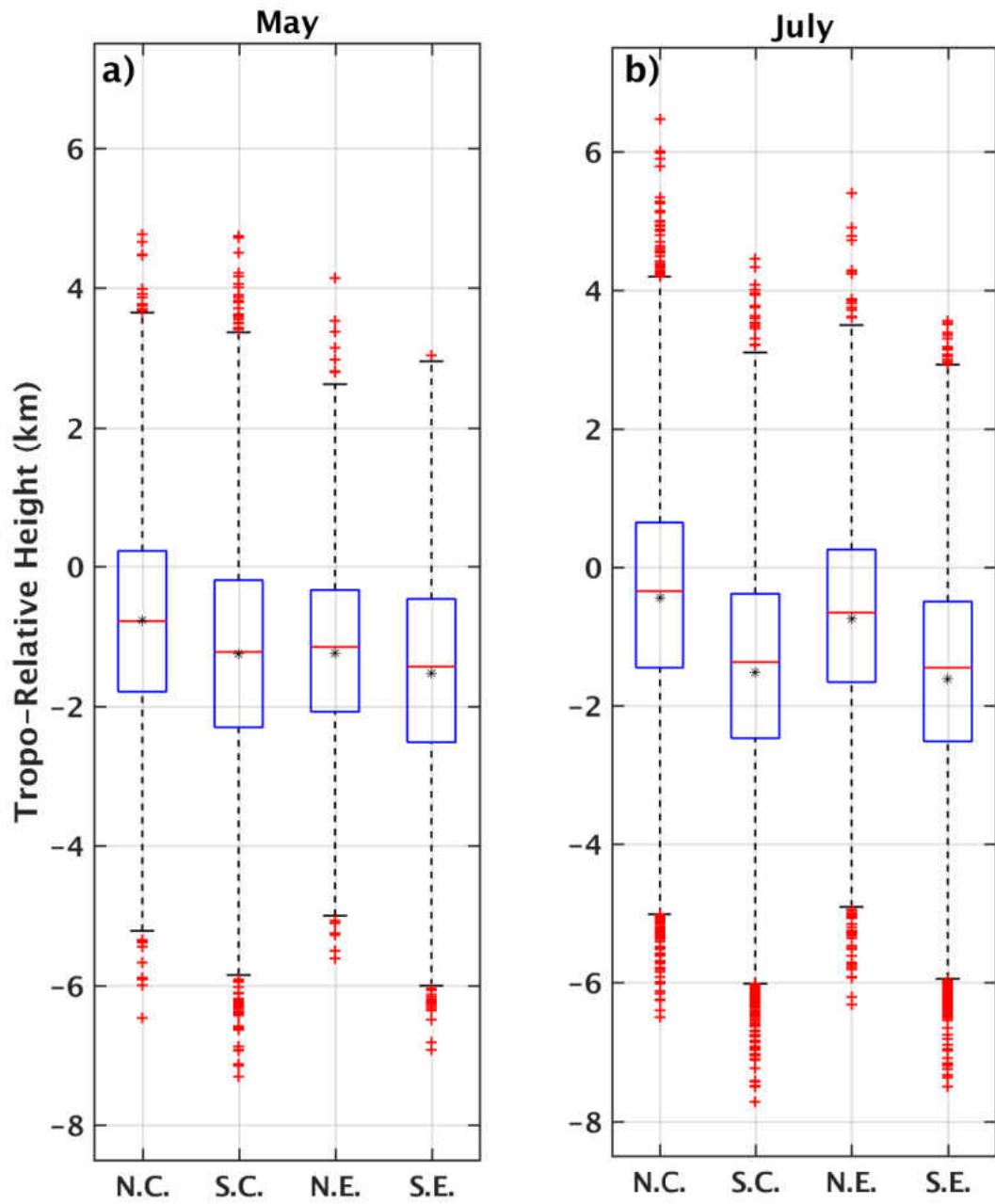


Figure 30: As in Figure 28, except for the anvil-top height and not the LMD height.

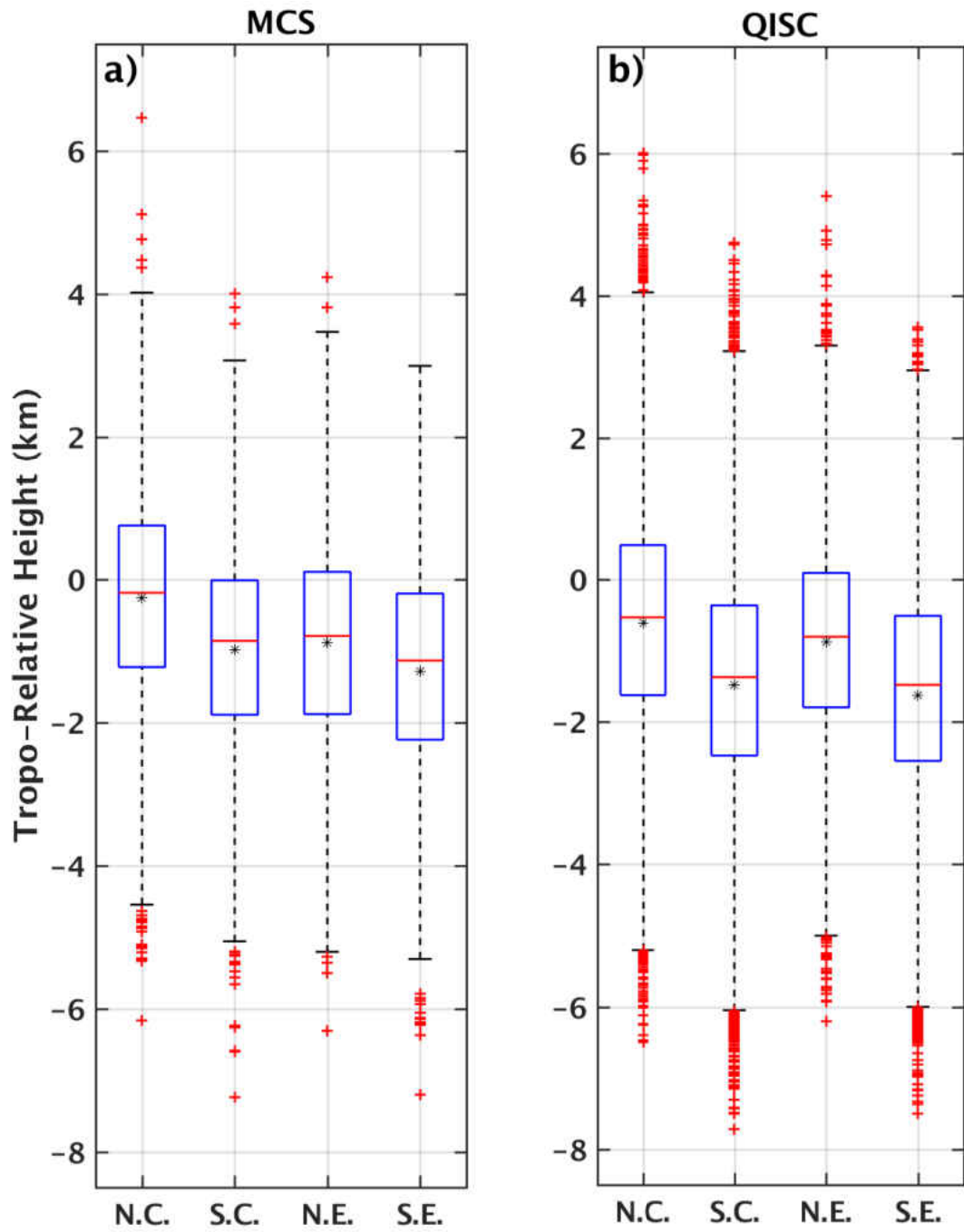


Figure 31: As in Figure 29, except for the anvil-top heights and not the LMD heights.

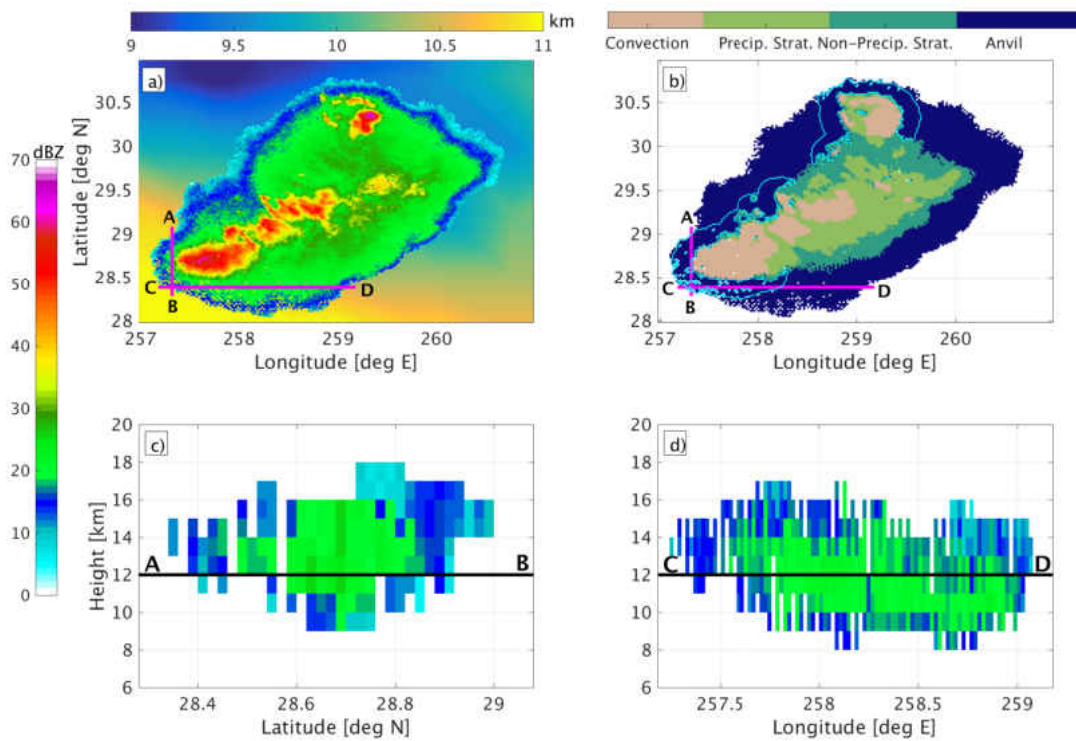


Figure 32: The a) composite reflectivity, b) SL3D classification, and vertical cross-sections of reflectivity following c) A to B and d) C to D in panels (a) and (b) for an MCS located primarily over southeastern Iowa on 18 July 2006 at 01 UTC. The gradient fill in panel (a) denotes the tropopause height and the black line in panels (c) and (d) denotes the LMD height retrieved for the storm.

## CHAPTER 5

### FRACTIONAL ENTRAINMENT RATE RETRIEVALS USING A BOUYANCY-BASED PLUME FRAMEWORK

#### 5.1 Introduction

Deep moist convection has large impacts on both global and local scales. Convection redistributes moisture and energy within the atmosphere and interacts with large-scale atmospheric circulations. On local and regional scales, convection-resolving models still struggle to correctly depict the size, intensity, and structure of deep convection and are frequently notably biased (e.g., Caine et al., 2013; Min et al., 2015; Starzec et al., 2018). The biases in convective structure can lead to large biases in latent heat exchanges and accumulated precipitation (e.g., Davis et al., 2009; Ebert and Gallus, 2009; Gallus, 2010; Johnson et al., 2013; Johnson and Wang, 2013). On global scales, deep convective clouds remain as one of the largest uncertainties within climate model simulations by impacting the energy exchange and radiative balance within the lower atmosphere. Misrepresentation of deep convective clouds can produce positive feedbacks on atmospheric circulations that further influence convection, which can result in incorrect or unphysical depictions of future climates (e.g., Cess et al., 1996, 1990; Zhang et al., 2005; Zhao, 2014).

Large uncertainties in depiction of clouds have been commonly associated with the parameterization of physical processes that occur on subgrid-scales (e.g., Randall et al., 2003; Arakawa, 2004; Rybka and Tost, 2014). Cumulus parameterizations aim to statistically depict the effects of deep moist convection and incorporate a multitude



of small-scale convective processes to adjust transfer of energy. On global scales, the variability between parameterizations has been shown to cause large differences in water vapor of up to 80% and temperature of up to 4 K, particularly in the upper troposphere due to the representation of convection within the different schemes (e.g., Tost et al., 2006; Zhang et al., 2008; Rybka and Tost, 2014). While many issues arise from attempting to represent highly-variable small-scale processes within coarse resolution models, there is still lack of knowledge on certain processes such as entrainment, which means they are poorly constrained in such parametrizations.

Entrainment of relatively colder, drier air into the convective updraft reduces the buoyancy of the rising parcel and influences the depth, intensity, and precipitation potential of the convective system. Entrainment has commonly been expressed using fractional entrainment rate ( $\lambda$ ) that is defined as the rate of change of mass with height of the rising plume relative to the original parcel mass and is given by

$$\lambda = \frac{1}{m} \frac{dm}{dz} \quad (5.1)$$

where  $m$  is the mass of the parcel and  $z$  is height (Houze, 1993). Entrainment has been a focus of numerous studies because of its impact on convection. For example, an entrainment rate of  $1 \text{ km}^{-1}$  (i.e., 100% increase in the plumes mass per kilometer) has been linked with up to a ten-fold decrease in the amount of realizable convective available potential energy (Zhang et al., 2008). On larger scales, errors in depicting entrainment was shown to be the one of the dominant causes of general circulation models producing a diurnal cycle of rainfall several hours earlier than observed (Yang and Slingo, 2001; Del Genio and Wu, 2010; Stirling and Stratton, 2011).

It is difficult to constrain convective parameterizations due to infrequent observations on both spatial and temporal scales that are able to measure the effects

of entrainment. Entrainment rates have been most commonly retrieved for shallow clouds, such as stratocumulus clouds, as these clouds are commonly devoid of precipitation and have weak dynamical forcing. Shallow cloud fractional entrainment rates found by previous studies range anywhere from 0.3 to 3  $\text{km}^{-1}$  with extreme entrainment rates reaching 6  $\text{km}^{-1}$  also being reported (e.g., Siebesma and Cuijpers, 1995; Gerber et al., 2008; Romps, 2010; Lu et al., 2012; Yeo and Romps, 2013; Wagner et al., 2013; Moser and Lasher-Trapp, 2017). Observational studies of deep convective entrainment rate retrievals are limited due to the complicated nature of deeper convection, as such studies need to account for complex microphysical-dynamical interactions and dynamic forces that develop within an updraft. To account for some of these processes, Jensen and Del Genio (2006) used the conservation of equivalent potential energy to retrieve entrainment rates for tropical cumulus convection and found entrainment rates varied from 0.01 to 0.68  $\text{km}^{-1}$ . Guo et al. (2015) used aircraft measurements in a moist static energy framework and found that entrainment rates varied depending on cloud width, but found rates up to  $\sim 0.8 \text{ km}^{-1}$ . Due to the lack of observations, studies have shifted to developing idealized models or theoretical frameworks to better understand the deep convective entrainment process and attempt to retrieve “direct estimates” of entrainment by following parcel motions in and out of the updraft. Deep convective entrainment rates have been found to typically range up to 1.5  $\text{km}^{-1}$ , with rates usually lower than those seen in shallow convection (e.g., Gregory, 2001; Khairoutdinov and Randall, 2006; Romps, 2010). Unfortunately, these models are unconstrained and difficult to verify; thus, more observational-based methods are required.

In this study, a dynamically-based method is developed to determine the fractional entrainment rate of deep convection by using observations of vertical velocity (such as from multi-Doppler observations) and environmental temperature and mois-

ture profiles (such as from soundings). The methodology works on the basis of comparing the buoyancy of an idealized (unmixed) plume to the buoyancy of the observed (mixing) plume by constraining the ideal plume with observations as discussed in section 5.2. The methodology is demonstrated on two modeled cases of deep convection of different intensities using different characteristics of ideal parcel ascent described in section 5.3. For context, the resulting fractional entrainment rates are compared to a traditional constant entrainment rate plume model in section 5.4. Lastly, discussion and limitations of this approach are discussed in section 5.5.

## 5.2 Entraining Plume Model

The procedure to determine how the entrainment rate varies with height involves constraining plume theory by coupling vertical velocity observations with environmental observations. This study contains many of the traditional assumptions made in entraining plume theory, where the plume is assumed to represent the cloud updraft and the interior of the plume is considered homogeneous and in steady-state. Furthermore, all entrained air into to updraft is assumed to be environmental (i.e., cloud-free) air represented by a steady-state sounding. No detrainment is included in the model; however, a lack of the detrainment process should not affect the internal properties of the plume as detrainment only mixes the plume properties into the environment.

A general overview schematic of the fractional entrainment rate procedure is depicted in Figure 33. Starting at cloud base (i.e.,  $z_1$  in Fig. 33), the mixed (i.e., observed) parcel temperature and moisture content are determined by iteratively solving the vertical momentum equation using observations (following section 5.2.1). An ideal parcel is initialized at  $z_1$  with the retrieved mixed parcel properties and ascends following modified parcel theory until the next height with vertical velocity observations

(e.g.,  $z_2$ ). The difference between the ideal parcel temperature and retrieved mixed parcel temperature at  $z_2$  is attributed to entrainment and the fractional entrainment rate is determined (following section 5.2.2). The ideal parcel at  $z_2$  is then mixed to match the mixed parcel properties at  $z_2$  and the process is repeated until cloud top is reached.

Since the standard representation of parcel theory only assumes irreversible ascent, entrainment rate retrievals will be biased as they do not include effects such as hydrometeor drag, ice-phase processes, and perturbation pressure gradients that act on the parcel. Parcel theory is modified to include hydrometeor drag and ice-phase processes (as described in section 5.2.3) to investigate the variability induced in entrainment rate retrievals when these effects are included.

### 5.2.1 Mixed Temperature Retrieval

Using the vertical momentum equation scaled for parcel motions, the vertical velocity of an observed parcel is given by

$$\frac{Dw^*}{Dt} = \frac{-1}{\rho} \frac{\partial p'}{\partial z} + B_p - \frac{1}{m} \frac{Dm}{Dt} w^* \quad (5.2)$$

where  $w^*$  is the mixed (i.e., observed) parcel vertical velocity,  $\rho$  is density,  $p'$  is the perturbation pressure,  $B_p$  is parcel buoyancy, and  $m$  is mass of the parcel (adapted form of Eq. 7.19 from Houze (1993)). Herein, the ending subscript ‘p’ and ‘e’ on atmospheric variables describe the ideal (unmixed) parcel and environment properties, respectively, and the superscript ‘\*’ denotes the mixed or observed parcel property that incorporates entrainment. The first term on the right-hand side (r.h.s) is the perturbation pressure gradient force, the second term is the ideal parcel buoyancy, and the third term is the change in buoyancy due to entrainment of environmental

air. Following Houze (1993), by using  $w = Dz/Dt$  the coordinates of Eq. (5.2) are transformed to

$$\frac{1}{2} \frac{Dw^{*2}}{Dz} = \frac{-1}{\rho} \frac{\partial p'}{\partial z} + B_p - \frac{1}{m} \frac{Dm}{Dz} w^{*2} \quad (5.3)$$

Since the entrainment term (i.e., term three) is a negative buoyancy term relative to the rising positively buoyant parcel, it can be combined with the unmixed parcel buoyancy (term two) to give the mixed parcel buoyancy,  $B^*$ , which is the buoyancy that includes entrainment effects on the rising parcel and Eq. (5.3) becomes

$$\frac{1}{2} \frac{Dw^{*2}}{Dz} = \frac{-1}{\rho} \frac{\partial p'}{\partial z} + B^* \quad (5.4)$$

For simplicity, ignoring the pressure perturbation gradient terms and assuming the perturbation pressure within the buoyancy term is small (e.g., Markowski and Richardson, 2010), viewing buoyancy in a virtual potential temperature framework,

$$\frac{1}{2} \frac{Dw^{*2}}{Dz} = \frac{\theta_{vp}^* - \theta_{ve}}{\overline{\theta_{ve}}} g \quad (5.5)$$

where  $g$  is the gravitational constant, and  $\theta_{vp}^*$ ,  $\theta_{ve}$ , and  $\overline{\theta_{ve}}$  are the mixed parcel, environmental, and mean environmental virtual potential temperatures, respectively.  $\theta_{vp}^*$  is the virtual potential temperature of the rising parcel that includes effects of entrainment. By integrating across two heights with vertical velocity observations, Eq. (5.5) becomes

$$\theta_{vp}^* = \left[ \frac{w^{*2}(z_2) - w^{*2}(z_1)}{z(z_2) - z(z_1)} \right] \left[ \frac{\overline{\theta_{ve}}}{2g} \right] + \theta_{ve}. \quad (5.6)$$

If the mixed parcel is assumed to be completely saturated, then the mixed parcel temperature ( $T_p^*$ ) and mixed parcel water vapor mixing ratio ( $q_{vp}^*$ ) can be iteratively

determined by applying the Magnus equation. These mixed parcel values depict what the observed parcel temperature and moisture content must have been, respectively, to produce the observed  $\theta_{vp}^*$  and hence the observed vertical velocity (i.e.,  $w^*$ ).

Equation (5.6) assumes no hydrometeors are present to produce drag on the parcel, which is true of irreversible ascent. Under reversible ascent,  $\theta_{vp}^*$  in Eq. (5.6) includes the effects of hydrometeor loading by assuming the difference between the parcel  $q_{vp}^*$  at cloud base and the parcel saturation vapor pressure at a certain height results in development of condensate. When ice processes are included, the newly developed hydrometeor phase is determined by following a linear function of temperature further discussed in section 5.2.3. At the initial level at cloud base, it is assumed no hydrometeors are present in the parcel.

### 5.2.2 Fractional Entrainment Rate

Following the assumptions made in section 5.2.1, the rate of change of a parcel's temperature with height caused by continuous, homogenous (lateral) entrainment is given by

$$\frac{DT_p^*}{Dz} = \frac{-g}{c_p} - \frac{L}{c_p} \frac{Dq_{vp}}{Dz} + \lambda \left[ [T_e - T_p] + \frac{L_v}{c_p} [q_{ve} - q_{vp}] \right] \quad (5.7)$$

where  $T_e$  is the environmental temperature,  $T_p$  is the unmixed parcel temperature,  $c_p$  is the specific heat of water,  $L_v$  is the latent heat of vaporization, and  $q_{vp}$  and  $q_{ve}$  are the water vapor mixing ratios of the parcel and environment, respectively (Eq. 7.22 in Houze (1993)). The first two terms on the r.h.s. are the internal changes experienced by a buoyant parcel of air and depict the dry adiabatic expansive parcel cooling modulated by latent heating due to changes in water vapor content via phase changes. The last term contains the effects of entrained air on the buoyancy of the parcel by changes to the parcel temperature and water vapor content. Assuming

no advective contributions to the plume, integrating across two heights that contain observations and re-arranging terms

$$T_p^*(z_2) = T_p^*(z_1) + \int_{z_1}^{z_2} \left[ \frac{-g}{c_P} - \frac{L_v}{c_p} \frac{Dq_{vp}}{Dz} \right] dz - \ln(\chi) \left[ [T_e - T_p] + \frac{L_v}{c_p} [q_{ve} - q_{vp}] \right] \quad (5.8)$$

where  $\chi$  is the mixing fraction of air that denotes the mass ratio of adiabatic cloudy air at  $z_1$  to the mixture of air containing the adiabatic cloudy air and entrained air at  $z_2$ . The  $\chi$  is found by integrating Eq. (5.1), where

$$\lambda = \frac{\ln \frac{m(z_2)}{m(z_1)}}{[z(z_2) - z(z_1)]} = \frac{-\ln(\chi)}{[z(z_2) - z(z_1)]} \quad (5.9)$$

as in Lu et al. (2012). While integrating Eq. (5.8), it is assumed that  $\lambda$  does not vary in the layer from height  $z_1$  to  $z_2$ , which is consistent with plume theory. The first two terms on the r.h.s. in Eq. (5.8) denote the mixed parcel temperature at height  $z_1$  and the internal changes the parcel experiences (following parcel theory; section 5.2.3) as the parcel accelerates from  $z_1$  to  $z_2$ , respectively. It is possible to combine these two terms, resulting in the unmixed parcel temperature at  $z_2$  as entrainment is not included; therefore,

$$T_p^*(z_2) = T_p(z_2) - \ln(\chi) \left[ [T_e - T_p] + \frac{L_v}{c_p} [q_{ve} - q_{vp}] \right] \quad (5.10)$$

and

$$\chi = e^{-\frac{T_p^*(z_2) - T_p(z_2)}{[T_e - T_p] + \frac{L_v}{c_p} [q_{ve} - q_{vp}]}}. \quad (5.11)$$

The  $\chi$  can be used to determine the fractional entrainment rate using Eq. (5.9). The unmixed parcel properties can be determined using parcel theory assumptions (section 5.2.3) while the mixed parcel temperature and be retrieved by incorporating

observations of the environmental temperature and moisture with vertical velocity data (as discussed in the previous section).

### 5.2.3 Ideal Parcel Ascent

Parcel ascent is determined by parcel theory. Parcel theory describes the ascent path of a parcel of air relative to the environmental temperature and moisture profile. The traditional form of parcel theory assumes pseudoadiabatic or irreversible ascent (i.e., all hydrometeors instantly fall out of the parcel when formed), no pressure perturbation effects exist, the ice-phase is ignored, and no entrainment or mixing occurs. Since the aforementioned effects are not included in parcel theory, any fractional entrainment rate retrievals following the methodology in sections 5.2.1 and 5.2.2 would likely be inaccurate as these processes (which are all highly active in convection) would be unaccounted for. To account for some of these effects on the parcel buoyancy, parcel ascent is also determined following reversible ascent and a simplistic ice phase is included via the deposition/freezing pathways; however, pressure gradient forces are not included.

When the parcel is unstable, it is considered to be positively buoyant relative to the environment, where buoyancy is defined as

$$B_p = g \frac{\theta_{vp} - \theta_{ve}}{\theta_{ve}}, \quad (5.12)$$

where  $\theta_{vp}$  is the virtual potential temperature of the ideal parcel. The virtual potential temperature is defined as

$$\theta_v = \theta(1 + 0.61q_{vp} - q_{hydro}), \quad (5.13)$$



where  $\theta$  is the potential temperature and  $q_{hydro}$  is the hydrometeor loading or drag term. Under irreversible ascent,  $q_{hydro}$  is 0. When hydrometeors are included, the parcel follows reversible ascent, where all hydrometeors are assumed to stay within the parcel and never fall out; therefore, the impact of hydrometeor drag gradually increases with height and acts to decelerate the parcel. While realistically the parcel ascent is between the reversible and irreversible rates, assuming that either all hydrometeors fall out or all hydrometeors stay with the parcel provides the range where the actual parcel profile should be present without attempting to calculate the actual amount of hydrometeors and further including more uncertainty. The mass of water vapor at each level that condenses to liquid water is given by

$$\Delta q_l = \frac{q_{vp} - q_{vs}}{1.0 + \frac{q_{vs} L_v^2}{C_d R_v T_p}}, \quad (5.14)$$

where  $q_{vs}$  is the saturation mixing ratio,  $C_d$  is the specific heat of dry air, and  $R_v$  is the water vapor gas constant (following Bryan and Fritsch (2002)).  $L_v$  is dependent on temperature and is given by

$$L_v = L_{v0} - (C_l - C_{pv})(T_p - T_0), \quad (5.15)$$

where  $L_{v0}$  is the reference latent heat of vaporization,  $C_l$  is the specific heat of liquid water,  $C_{pv}$  is the specific heat of water vapor, and  $T_0$  is the reference temperature. Eq. (5.14) is solved iteratively and limits the amount of condensate generated by including the latent heat release of condensation, which affects the saturation vapor mixing ratio. In reversible ascent,  $\Delta q_l$  is retained and  $q_{hydro}(z_2) = q_{hydro}(z_1) + \Delta q_l$ .

Following Bryan and Fritsch (2002), the change in latent heating of the parcel is

$$\Delta Q = \frac{\Delta q_t L_v^2}{C_d R_v T_p}. \quad (5.16)$$

When simple ice processes are included, ice is added in two ways: converting only the new condensate to ice hydrometeors via deposition (e.g., Bryan and Fritsch, 2002) and converting existing water hydrometeors to ice hydrometeors via freezing. Both pathways for conversion of liquid water to ice water follow a simple linear relationship based on temperature, given by

$$ratio = max \left( min \left( \frac{T_p - 233.15}{273.15 - 233.15}, 1.0 \right), 0.0 \right). \quad (5.17)$$

In summary, if the parcel temperature is  $\geq 0^\circ\text{C}$  the ratio in Eq. (5.17) is 1.0 and new hydrometeor mass is assumed to increase only via condensation growth of liquid water and no freezing of pre-existing liquid water occurs. If the parcel temperature is  $\leq -40^\circ\text{C}$ , Eq. (5.17) has a ratio of 0 and new hydrometeor mass is assumed to increase via deposition of excess vapor to ice water only, and all pre-existing liquid water freezes to ice water. The linear temperature relationship results in overly-rapid freezing process; however, it is adequate for a simple first-order approximation of ice phase processes. Since liquid water is sub-saturated with respect to ice and ice is super-saturated with respect to water, between  $0^\circ\text{C}$  and  $-40^\circ\text{C}$ , an effective saturation mixing ratio is determined by

$$q_s = (ratio)q_{vs} + (1.0 - ratio)q_{is}, \quad (5.18)$$

where  $q_{is}$  is the ice water saturation mixing ratio. The maximum potential new mass of ice,  $\Delta q_{imax}$ , and water,  $\Delta q_{lmax}$ , is then

$$\Delta q_{imax} = \max((1.0 - ratio)(q_{vp} - q_s), 0.0), \quad (5.19)$$

$$\Delta q_{lmax} = \max(ratio(q_{vp} - q_i - q_s), 0.0), \quad (5.20)$$

where  $q_i$  is the ice water mixing ratio. The actual amount of ice and water condensed at each level follows similar arguments as Eq. (5.14) and is

$$\Delta q_l = \frac{\Delta q_{lmax}}{1.0 + \frac{q_{vs} L_v^2}{C_d R_v T_p}}, \quad (5.21)$$

and

$$\Delta q_i = \frac{\Delta q_{imax}}{1.0 + \frac{q_{is} L_s^2}{C_d R_v T_p}}, \quad (5.22)$$

respectively.  $L_s$  is the temperature-dependent latent heat of sublimation and is given by

$$L_s = L_{s0} - (C_i - C_{pv})(T_p - T_0), \quad (5.23)$$

where  $C_i$  is the specific heat of ice water and  $L_{s0}$  is the reference latent heat of sublimation. For reversible processes, the hydrometeor loading term is then  $q_{hydro}(z_2) = q_{hydro}(z_1) + \Delta q_i + \Delta q_l$ . The amount of latent heat released follows Eq. (5.16) for both liquid water and ice water, except  $L_s$  is used for ice.

### 5.3 Application of Entraining Model to Convection

While the goal of this study is to develop a methodology that is able to retrieve entrainment rates from observations, the methodology is demonstrated on two modeled cases of deep convection to avoid incorporating any errors or biases present in ob-

servational data. For example, multi-Doppler observations may contain artifacts and biases in the vertical velocity field, especially at heights above 4 km (e.g., North et al., 2017; Oue et al., 2018). Atmospheric soundings are likely to also be spatially and/or temporally offset from where convection is occurring. A model dataset enables a comprehensive three-dimensional view and provides more control for sensitivity testing and methodology validation than a limited observational framework.

The two convective cases that are being analyzed were generated by real-time WRF forecasts matching the WSM6 model configuration and initialization used in Chapter 2 (section 2.2.1). To replicate the potential resolution of an observational dataset, the simulated vertical velocity data are linearly interpolated to a vertical grid with a grid spacing of 200 m. Environmental data (i.e., temperature and dew point) are linearly interpolated to a vertical grid with spacing of 20 m to replicate the resolution of sounding data. The methodology is applied to a weakly-forced shallow convective cell and a strong deep convective complex to 1) investigate how the methodology performs in convection of different magnitudes, scales, and dynamical forcing and 2) determine the potential variability in fractional entrainment rates between these convective cases.

### **5.3.1 Weakly-forced Shallow Convection**

The modeled weakly-forced convective case valid at 18 UTC on 3 July 2018 is presented in Figure 34a, which shows several small, weak convective cells in the domain. A vertical cross-section across the largest cell shows storm heights that reach  $\sim 5$  km with maximum reflectivity values  $\sim 43$  dBZ near the surface (Fig. 35a). The updraft core is visible to the east of the reflectivity column with maximum vertical velocity values reaching  $\sim 6$  m s<sup>-1</sup> just below 3 km (Fig. 35b). The environment is characterized by a  $\sim 100$  mb well-mixed boundary layer with a conditionally unstable

layer between  $\sim 850$  and  $700$  mb that is aiding convective development (Fig. 36). A surface-based parcel following parcel theory with irreversible ascent is able to reach  $\sim 350$  mb (black line; Fig. 36); however, a parcel following reversible ascent is only able to reach  $\sim 630$  mb (dark green line; Fig. 36) as the strong inversion right above the conditionally unstable layer is able to prevent deeper convective development and provides a better representation of the height of convection occurring at this time (e.g., Fig. 35a). The majority of the updraft and vertical velocity maximum occur below the freezing level, limiting the impact of latent heating from ice phase processes.

Since the ice phase has a minor impact on this case, the entrainment rate retrieval methodology is applied using only irreversible and reversible parcel ascent to investigate the variability in entrainment rates induced by assumptions in hydrometeor content. Figure 37a shows the vertical velocity profile using three different parcels: an ideal (unmixed) parcel that following parcel theory (red line), a mixing parcel following the entrainment rate methodology in section 5.2 assuming irreversible ascent (black), and a similar mixing parcel assuming reversible ascent (green). Without any mixing, the ideal parcel has significantly higher vertical velocities and is able to reach a maximum vertical velocity of  $\sim 42$  m s<sup>-1</sup> near 9 km (not shown; similar path to the irreversible parcel in Fig. 36). Both mixing parcels better match the vertical velocity observed in the model as they are constrained by the modeled vertical velocity measurements; however, the mixed parcel vertical velocities are still significantly larger than the modeled vertical velocity, meaning significant amounts of air must be entrained to mix the parcel to the model values. The virtual potential temperature profiles for each parcel ascent are shown in Figure 37b, and showcase the large difference between the mixed or actual virtual potential temperature retrieved using Eq. (5.6) to the virtual temperature predicted by the rising plume.

The fractional entrainment rates for this case reveal that hydrometeor drag cannot be neglected (Fig. 37c). The irreversible mixed parcel rates vary from  $\sim 0.6$  to  $1.6 \text{ km}^{-1}$  indicating that the parcel is entraining anywhere from over half to over 1.5 times its mass per kilometer. With hydrometeor drag, the rates are significantly lower and vary from  $\sim 0.25$  to  $0.55 \text{ km}^{-1}$ . The largest fractional entrainment rate retrieved for reversible ascent is smaller than the lowest rate retrieved for irreversible ascent.

### 5.3.2 Deep Convective Cluster

To investigate the retrieval methodology on more vigorous convection, a deep convective case valid on 21 UTC on 3 August 2012 is presented in Figure 34b. The storm cell being analyzed is located at the south end of a large storm cluster, with maximum reflectivity values reaching  $\sim 57 \text{ dBZ}$ . A vertical cross-section through part of the core region shows convection extending to  $\sim 14 \text{ km}$  with maximum updraft velocities reaching  $22 \text{ m s}^{-1}$  at  $\sim 10 \text{ km}$  (Fig. 38). The environment is characterized by a near-adiabatic layer extending to  $\sim 825 \text{ mb}$ , with a small layer of convective inhibition above it (Fig. 39). Ascent following an ideal irreversible parcel is able to reach  $13 \text{ km}$  with  $\sim 2350 \text{ J kg}^{-1}$  of convective available potential energy (CAPE; Fig. 39). An ideal reversible parcel is able to reach  $12.4 \text{ km}$  but contains 43% less CAPE. Convection in this case is clearly able to penetrate far above the freezing level, meaning ice-phase processes are able to inject a considerable amount of latent heat into the convective cell. Under ideal reversible mixed-phase ascent, the parcel is able to reach the same height as the irreversible parcel (cyan line; Fig. 39).

Profiles of vertical velocity show that the ideal irreversible parcel can reach a maximum of  $\sim 80 \text{ m s}^{-1}$  at  $13 \text{ km}$ , which is substantially greater than the modeled velocities (Fig. 40a). The profiles of the mixed parcels show that the irreversible mixed parcel contains slightly higher vertical velocities below  $\sim 5.75 \text{ km}$  (Fig. 40c),

but as the parcel temperature decreases below freezing, latent heat associated with ice production (visible in Fig. 40d) is able increase the buoyancy of the parcel and generate vertical velocities greater than the irreversible parcel.

On average, the irreversible mixed parcel fractional entrainment rate is  $\sim 0.25 \text{ km}^{-1}$ , with a maximum just over  $0.5 \text{ km}^{-1}$  at 3 km (black line; Fig. 40e). The fractional entrainment rate is near zero around  $\sim 7.5 \text{ km}$  and becomes negative above 7.5 km (which is unphysical). This occurs because the irreversible ascent can only make the parcel stable once the parcel properties are set to the mixed parcel (i.e., following the slope of the pseudoadiabats at high altitudes in Fig. 39 can only make the parcel stable). By including hydrometeor drag and ice phase processes, the average fractional entrainment rate is similar, but the location of the maxima is shifted from  $\sim 3 \text{ km}$  to  $\sim 6.5 \text{ km}$  (cyan line; Fig. 40e). The hydrometeor drag force negates a large portion of excess buoyancy in the parcel and the entrainment rate decreases by half below 5 km. At 2 km, the entrainment rate becomes negative, which is caused by hydrometeor drag reducing the parcel buoyancy enough that it momentarily becomes stable by interacting with the shallow layer of convective inhibition that was visible in Figure 39. Further aloft, additional latent heat release from ice processes are able to provide a substantial increase to the parcels buoyancy, meaning entrainment rates need to increase to account for the additional parcel acceleration. Including the ice phase enables the parcel to reach higher altitudes (9 km as opposed to  $\sim 7.5 \text{ km}$ ) and now better matches the height of the modeled vertical velocity maximum, indicating that ice processes cannot be neglected for deep convective entrainment rate retrievals. Since the ice scheme is expected to generate too much ice too fast and the hydrometeor drag term is likely too high as realistically not all the hydrometeors are retained by the parcel, the actual entrainment rates are likely found between the irreversible liquid-only and reversible mixed-phase parcel entrainment rate profiles.

Interestingly, the deep convective case has fractional entrainment rates roughly half that of the shallow case across the heights covered by both convective cells.

#### 5.4 Comparison to Traditional Plume Theory

To put the entrainment rate retrieval results in context, they are compared to the traditional form of plume theory that assumes a constant entrainment rate. The constant entraining plume model is a simplistic approach that assumes the parcel is entraining at the same rate everywhere as it ascends, and is commonly used by bulk plume parameterizations. The constant entrainment rate is typically applied from either cloud base or the surface until cloud top (which is assumed to be the level of neutral buoyancy). The constant entrainment rate,  $\sigma$ , is determined by following Jensen and Del Genio (2006) where

$$\theta_{ES}(z + \Delta z) = \left[ \frac{\theta_{ES}(z) + \sigma \Delta z \theta_E}{1 + \sigma \Delta z} \right], \quad (5.24)$$

where  $\theta_E$  and  $\theta_{ES}$  are the equivalent potential temperature and saturated equivalent potential temperatures, respectively, determined following Bolton (1980).  $\theta_E$  has been used to investigate entrainment as it is a conserved quantity in saturated and moist adiabatic expansion that accounts for all the (liquid) latent energy stored in a moist parcel of air, which is commonly assumed to be a good approximation in the tropics because the environment is relatively close to saturation. In the midlatitudes, this approximation is less valid as the atmosphere has significant deviations from near-saturation. Since  $\theta_E$  is conserved, an ideal parcel that does not mix with the environment should have a constant  $\theta_E$  throughout the troposphere while an entraining parcel will have its  $\theta_E$  reduced as it rises. Equation (5.24) is iteratively solved by increasing the values of  $\sigma$  until the  $\theta_E$  of the parcel matches the  $\theta_{ES}$  of the



environment at the LMD of the convective cell. The LMD is determined following Mullendore et al. (2009) and is defined as the greatest rate of horizontal divergence (i.e., vertical convergence) where

$$Divergence = \frac{d(\rho w^*)}{dz} \quad (5.25)$$

where  $\rho$  is density that assumed to follow an exponential decay assuming a scale height of 7.4 km. The  $\theta_E$  of a surface-based parcel and a parcel with the properties found at the top of the boundary layer are used to determine the constant entrainment rate to provide a range of entrainment rates that should encompass any boundary layer parcel.

Figure 41 shows the equivalent potential temperature profile and both the surface and top of the boundary layer parcel ascent paths for the shallow convective case (discussed in section 5.3.1). The LMD for this case was approximated at 4.06 km (horizontal black line; Fig. 41). For the surface parcel to reach the LMD while constantly entraining air at the same rate, it must be entraining air at a rate of  $\sim 0.23 \text{ km}^{-1}$  while a constant entrainment rate of  $\sim 0.19 \text{ km}^{-1}$  is needed for a parcel originating at the top of the boundary layer. For the deep convective case (discussed in section 5.3.2), because the boundary layer is well-mixed the differences between a surface parcel and boundary layer top parcel are relatively negligible, and the constant entrainment rate needed is  $\sim 0.07$  to  $0.08 \text{ km}^{-1}$  to reach the  $\sim 11.5 \text{ km}$  LMD (Fig. 42).

The entrainment rates retrieved from the constant entraining plume method are notable smaller than fractional entrainment rates retrieved following section 5.2. For the shallow convective case, the constant entrainment rate was similar to the lowest fractional entrainment rate retrieved assuming reversible ascent; however, overall

the fractional entrainment rates were higher. For the deep convective case, the entrainment rates between the two methods were only similar between 4 and 5 km, particularly when assuming reversible ascent. At any other height, the fractional entrainment rates were notably higher.

## 5.5 Discussion

When discussing entrainment rates, it is important to understand the context of the entrainment rates retrieved. For example, the shallow convective case had an entrainment rate of  $\sim 0.28 \text{ km}^{-1}$  at 2 km assuming reversible ascent, meaning the plume was entraining air at a rate of 28% of the plume's mass per kilometer. Since the vertical grid spacing of the data is 200 m, an alternative way to think about this process is that the plume had to entrain 5.6% of its mass between 1.8 km and 2 km to match the properties of the plume derived from observations. The 5.6% mass increase is relative to the mass of the parcel at 1.8 km not the original (i.e., starting) parcel, since the original parcel has previously already increased its mass three times due to entrainment (as it ascended from cloud base at 1.2 to 1.4 km, 1.4 to 1.6 km, and 1.6 to 1.8 km).

There are several assumptions and limitations associated with this methodology. One of the assumptions is that entrainment occurs only laterally. Studies have long hypothesized that cloud-top entrainment likely plays a significant role (e.g., Squires, 1958; Paluch, 1979). These hypotheses have been recently refuted (e.g., Zhao and Austin, 2005; Heus and Jonker, 2008; Romps, 2010; Dawe and Austin, 2011) suggesting that majority of entrainment occurs laterally, limiting the impact of assuming no cloud-top entrainment. Nevertheless, retrieving the mixed parcel properties (section 5.2.1) involves utilizing the observed vertical velocity, which includes all mixing process, but when the fractional entrainment rate is calculated based on the offset

between the rising parcel and retrieved mixed properties, it is assumed to only occur laterally.

Entrainment is also assumed to be continuous and homogenous; however, there are many strong arguments against this (discussed in de Rooy et al. (2006)). While the methodology is derived from these assumptions, they can be mitigated based on the resolution of dataset used. For example, if vertical grid spacing of the data are 1 km, then any decrease in parcel buoyancy attributed to entrainment is distributed equally across that 1 km (i.e., continuous, homogenous entrainment assumed across that 1 km). If the vertical grid spacing is 1 m and there was a reduction in buoyancy, then the assumption that entrainment was continuous and homogenous across that 1 m is more appropriate and likely more realistic than across 1 km. The method is largely independent of the resolution of the data. The rising mixing plume is also assumed to mix instantaneously and is assumed to be homogenous, which is not realistic especially when studying smaller scale turbulent entrainment; however, the fractional entrainment retrievals would still be sufficient to verify cumulus parameterizations and bulk plume parameterizations of entrainment.

The pressure perturbation forces were also not accounted for, which can have magnitudes that greatly affect the buoyancy of a parcel (e.g., Morrison, 2016), and hence the rate of entrainment into the parcel. For shallow isolated convection in low-shear environment, the errors are likely lower as only the buoyant perturbation pressure gradient force will likely have a notable contribution. For deeper convection in strong shear environments such as for mesoscale convective systems and supercells, in addition to a larger buoyant pressure perturbation forces, the dynamic perturbation pressure force can no longer be neglected and has a large contribution to the  $p'$  field. For completeness, the pressure perturbation force needs to be accounted for to retrieve accurate entrainment rates (particularly for deeper convection).

Lastly, there are also several caveats when applying the methodology to observational data. The methodology has a high sensitivity to the vertical velocity data; therefore, any errors or noise in observations will produce inaccurate mixing parcel properties and hence entrainment rate retrievals. The methodology also requires sounding data for retrieval of entrainment heights; however, it is not apparent where the sounding should be taken as one sounding is likely not representative of the entire three-dimensional storm environment. The soundings used in the two case studies were strictly environmental, meaning they were taken far away from the convective cells to avoid any direct cloud influences; however, entrainment of air into the updraft likely does not only contain environmental air but a mix of environmental and cloudy (non-updraft) air. Furthermore, the sounding is assumed to be in steady-state (i.e., not changing with time) as the parcel rises, which is likely unrealistic as the convection itself alters the near-storm environment via processes such as detrainment.

## 5.6 Conclusions

A buoyancy-based method is developed to constrain traditional plume theory with observations to better retrieve fractional entrainment rates. The goal of the methodology is to be able to use observations of vertical velocity such as taken by multi-Doppler observations and environment properties such as taken by soundings to retrieve entrainment rates for deep convection. The method works by using observations to retrieve the mixed (i.e., observed) plume properties at multiple levels. An ideal parcel starts with the mixed plume properties and ascends between levels. The fractional entrainment rate is retrieved by comparing the difference between the mixed and ideal parcel, when accounting for certain processes such as hydrometeor drag and latent heating related to the ice-phase.

The methodology was applied to two modeled cases: a shallow convective cell and a deep convective cluster. The shallow convective case extended to 5 km and had a maximum updraft velocity of  $6 \text{ m s}^{-1}$  just below 3 km. The fractional entrainment rates retrieved following reversible parcel ascent varied between  $\sim 0.25$  and  $0.55 \text{ km}^{-1}$  and were roughly half of rates found with irreversible parcel ascent. The deep convective case extended to 14 km and had a maximum vertical velocity of  $22 \text{ m s}^{-1}$  around 10 km. Fractional entrainment rates varied up to  $0.56 \text{ km}^{-1}$  and it was found that ice-phase processes were essential to retrieve entrainment rates aloft as it allowed for a better representation of the mixing plume properties aloft. The average entrainment rates for the deep convective cell were lower than the shallow cells entrainment rates. The fractional entrainment rate retrievals were compared to a traditional entraining plume using a constant entrainment rate. Results showed that the constant entraining plume model had significantly lower entrainment rates than retrieved by the buoyancy-based methodology, especially for the deep convective case.

By directly ingesting observations, the buoyancy-based methodology can be used to retrieve fractional entrainment rates for a large number of convective storms to help constrain cumulus parameterizations and verify theoretical models. Retrievals can also be used to investigate the differences in entrainment between different convective morphologies, as for example, supercells have been shown to detrain mass to much higher altitudes than ordinary convection and parcels more readily reach their LNB (e.g., Mullendore et al., 2013). This methodology can be combined with the LMD retrieval methodology in Chapter 4 to investigate the relationship between retrieved entrainment rates and the detrainment envelope to analyze how entrainment reduces parcel buoyancy and reduces detrainment altitudes from the LNB to the LMD. Furthermore, the methodology can be used to investigate the amount of dilution that

occurs within rising parcels in observed storms to better estimate the amount of mass that is reaching the UTLS and to quantify the variability in parcel dilution that is present with the detrainment envelope.

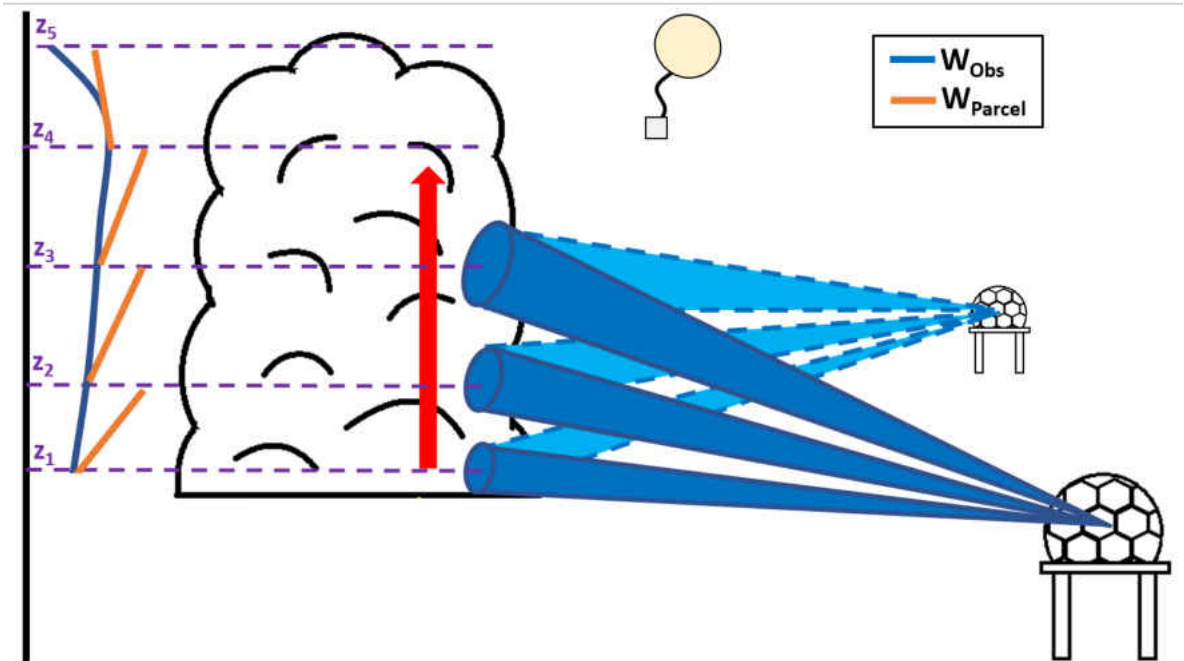


Figure 33: A illustrative overview of the fractional entrainment rate retrieval process, where a deep convective updraft is sampled by multiple Doppler radars with environmental profiles taken by a sounding. The blue line depicts a hypothetical observed vertical velocity while the orange line depicts a hypothetical idealized parcel ascending between levels.

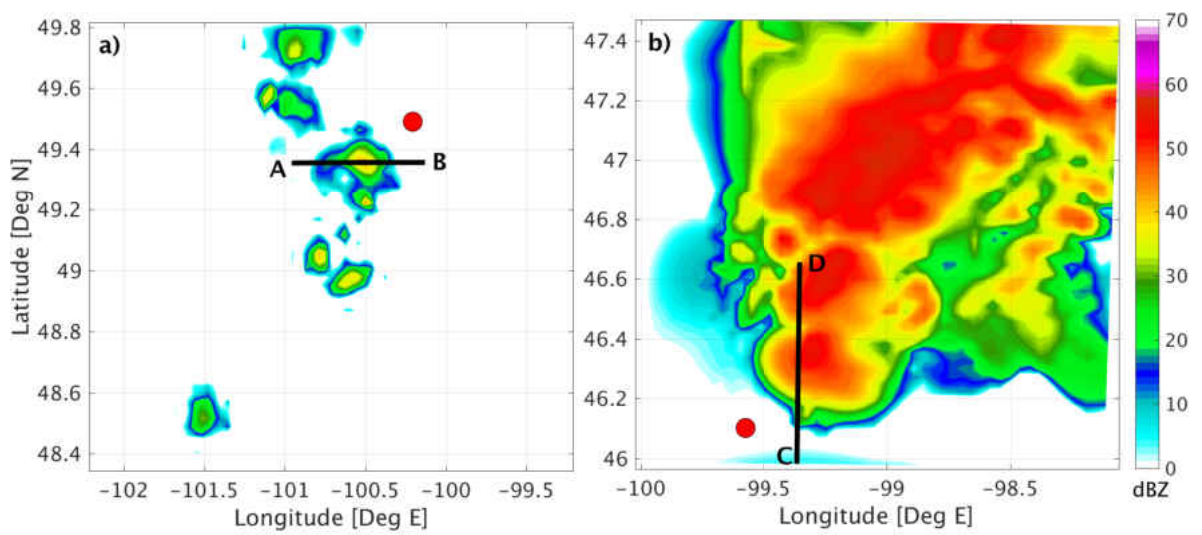


Figure 34: The composite simulated reflectivity for a) several weak convective cells forecasted at 18 UTC July 2018 and b) a deep convective cluster forecasted at 21 UTC on August 2012. The red circles denote the locations of the environmental soundings.



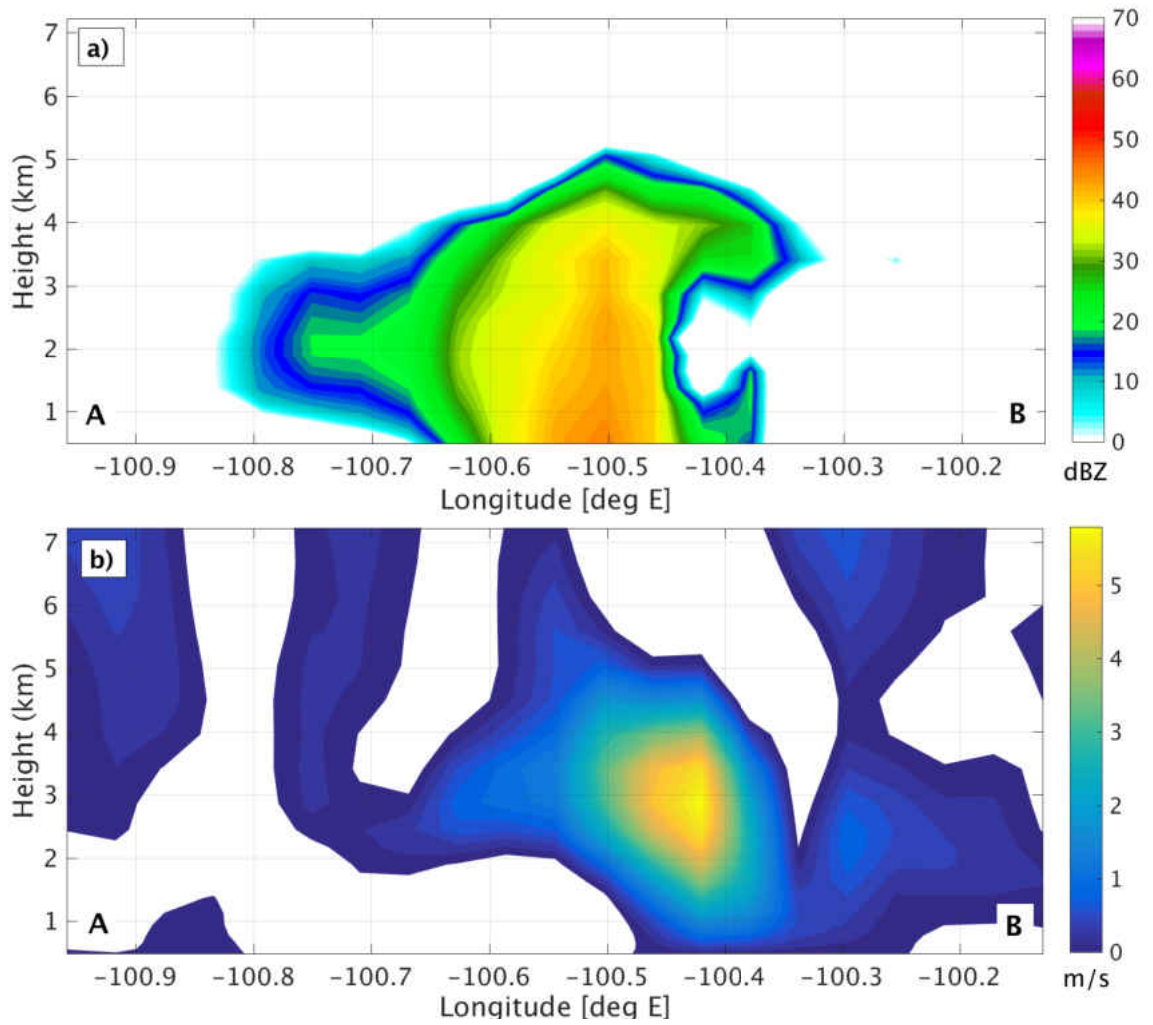


Figure 35: A vertical cross-section of a) simulated reflectivity and b) vertical velocity across the analysis cell from point A to point B in Figure 34a.

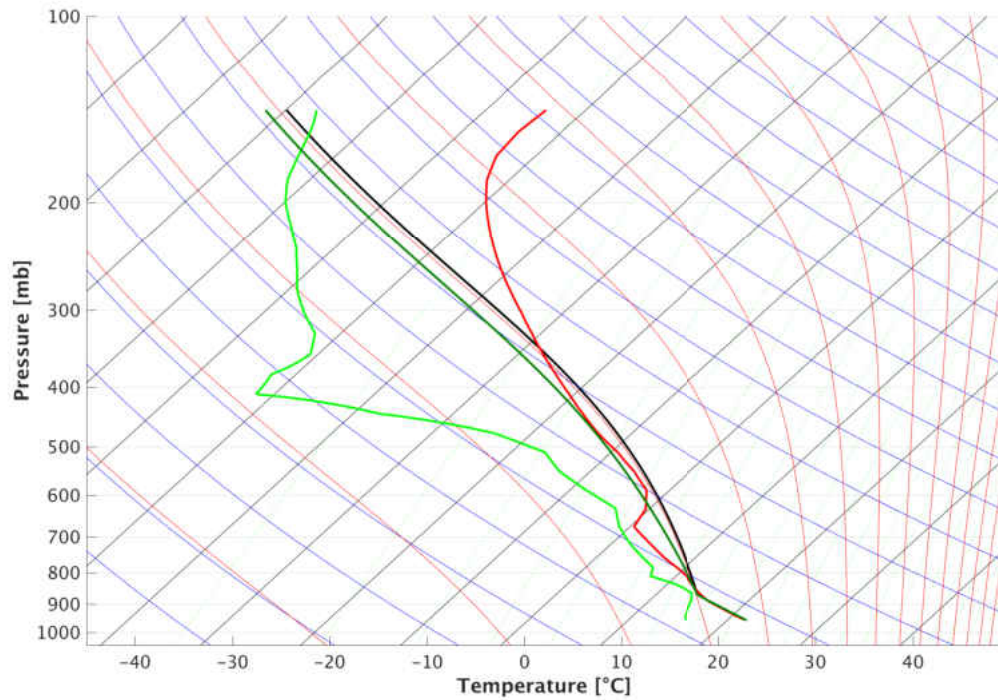


Figure 36: The environmental sounding used for the shallow convective cell. The red and light green lines depict the environmental temperature and dew point, respectively. The black and dark green lines depict the ascent path of a surface-based parcel assuming irreversible and reversible ascent, respectively.

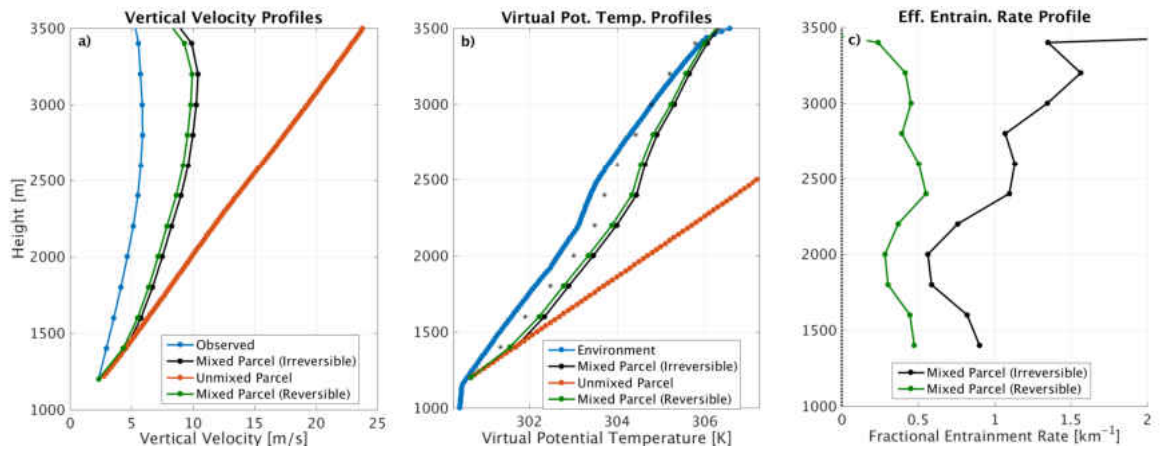


Figure 37: The a) vertical velocity, b) virtual potential temperature, and c) effective entrainment rate profiles for the shallow convective case. Blue lines depict the profile from the model, the black and dark green lines depict mixing parcels assuming irreversible and reversible ascent, respectively, and the red lines depict an ideal (non-mixing) irreversible parcel ascent. The stars in panel b) denote the mixed parcel virtual potential temperature.

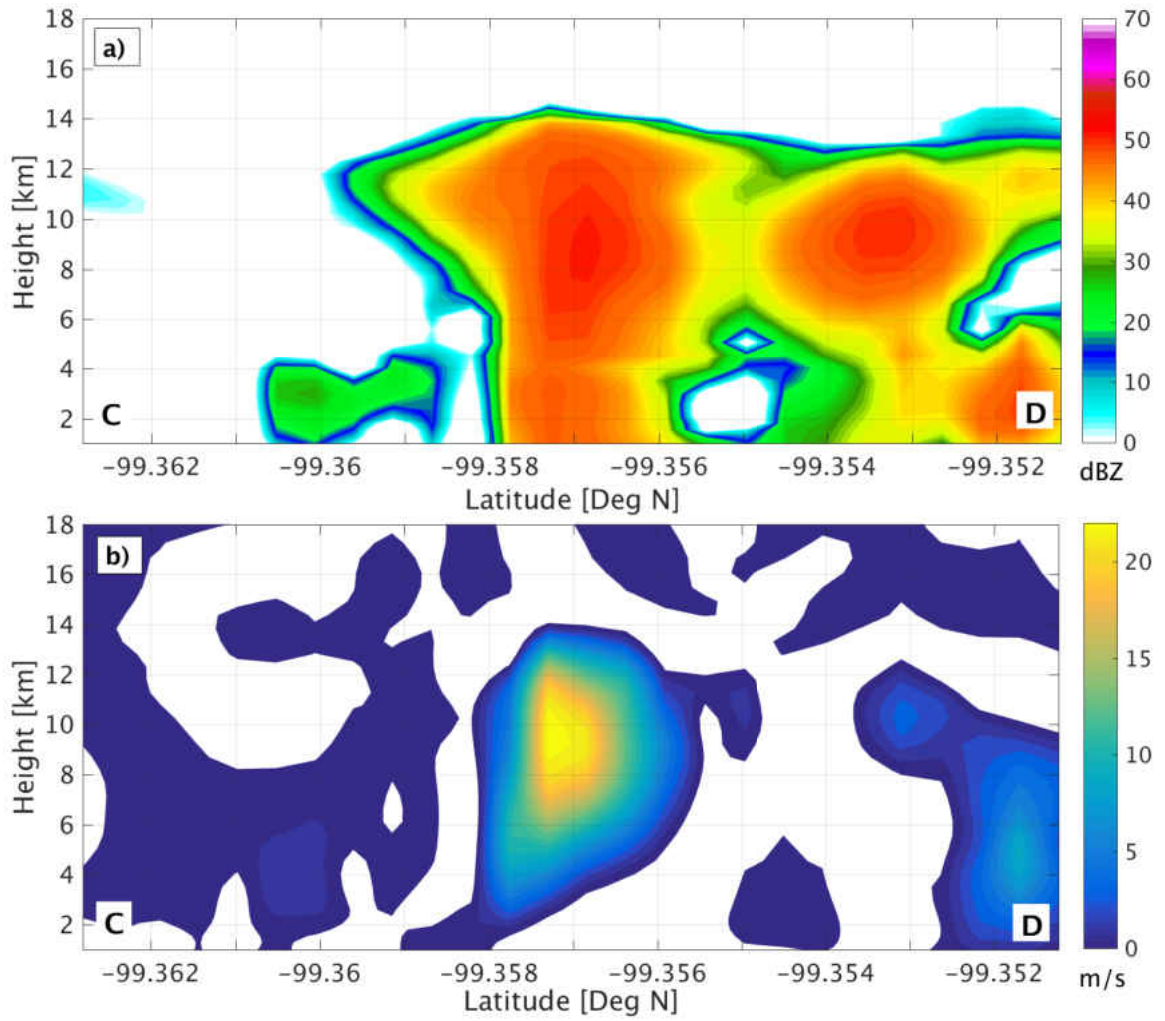


Figure 38: A vertical cross-section of a) simulated reflectivity and b) vertical velocity across the analysis cell from point C to point D in Figure 34b.

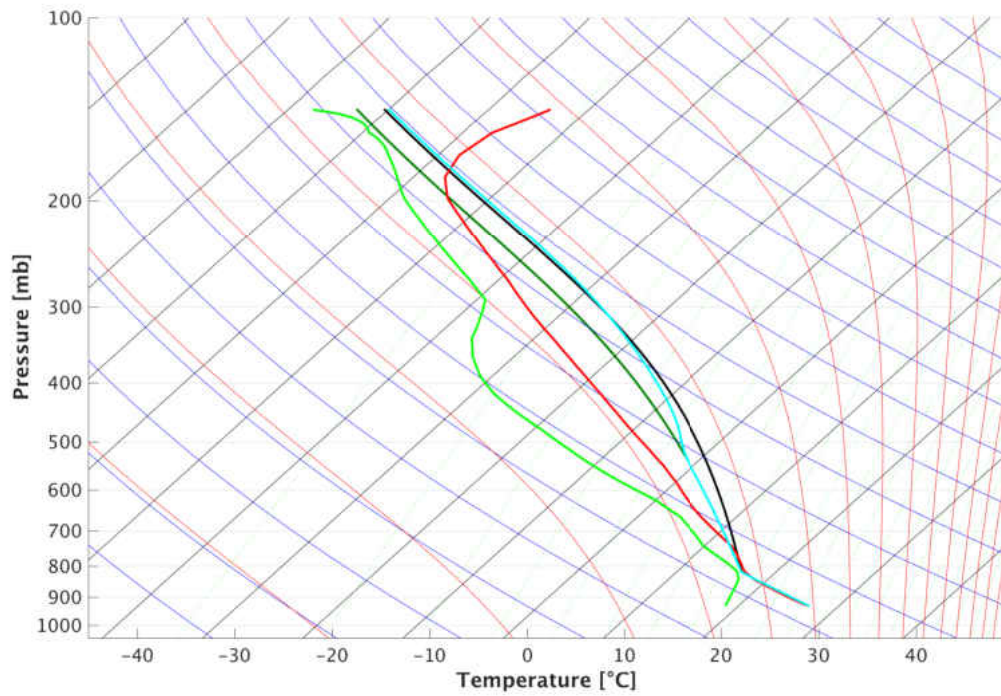


Figure 39: As in Fig. 36 except for the deep convective cell. The cyan line denotes a reversible process with ice-phase processes included.

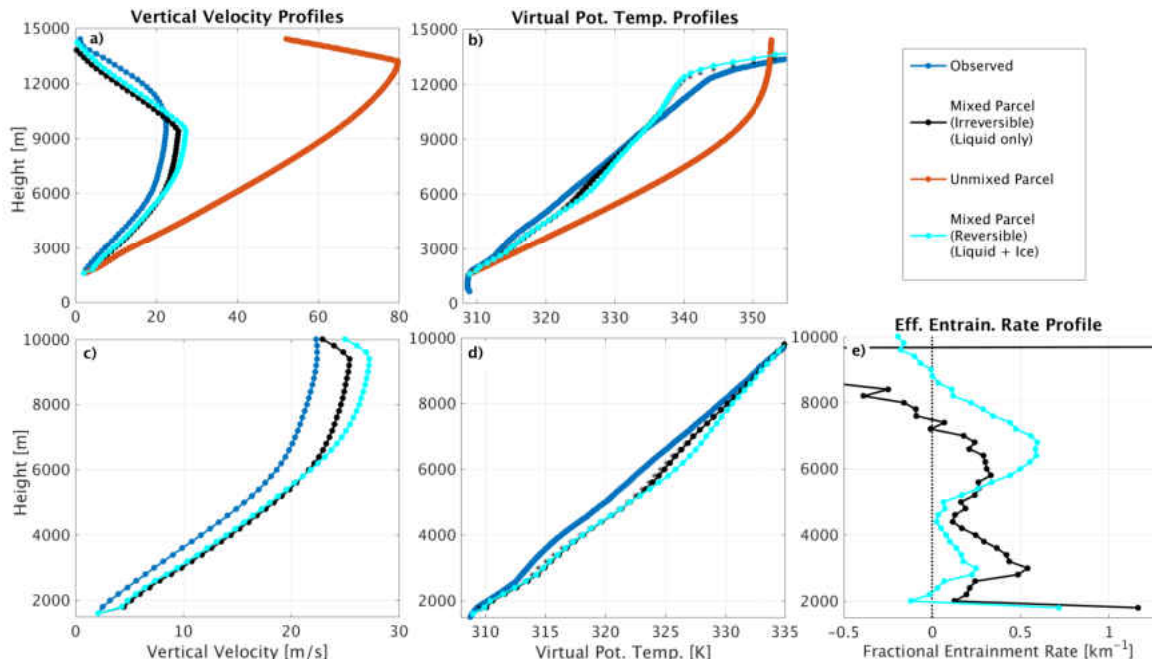


Figure 40: The a, c) vertical velocity, b, d) virtual potential temperature, and e) effective entrainment rate profiles for the deep convective case. Panels c) and d) are the same as panels a) and b), respectively, but are shown close-up to better illustrate the mixing parcel ascent paths. Blue lines depict the profile from the model, the black and cyan lines depict mixing parcels assuming irreversible liquid-only and reversible mixed-phase ascent, respectively, and the red lines depict an ideal (non-mixing) irreversible parcel ascent. The stars in b) and d) denote the mixed parcel virtual potential temperature.

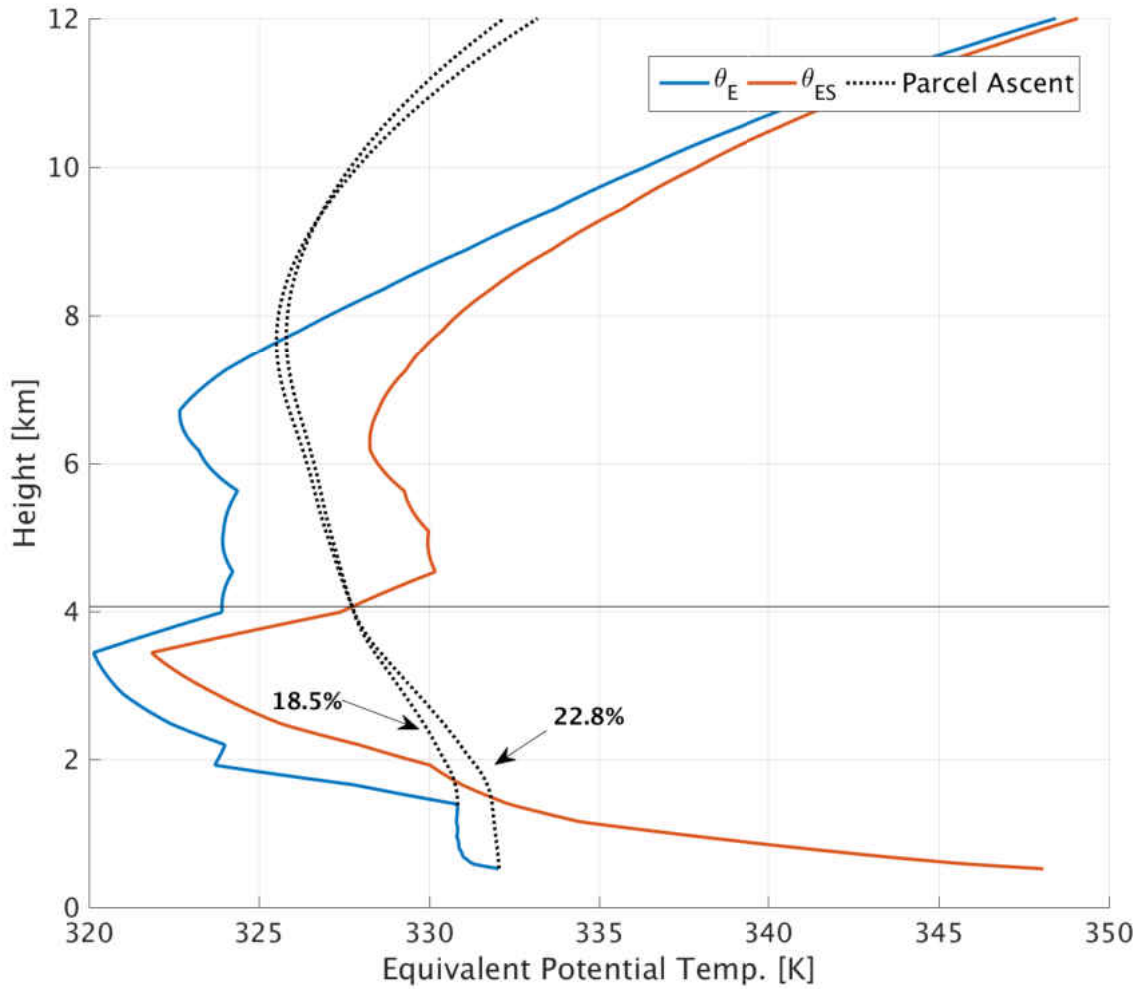


Figure 41: The environmental (blue)  $\theta_E$  and (red)  $\theta_{ES}$  and (black dashed lines) the parcel ascent paths from the surface and top of the boundary layer for the shallow convective case. Parcels ascend assuming a constant entrainment rate until the parcels reach the storm's LMD height (denoted by a horizontal solid black line).

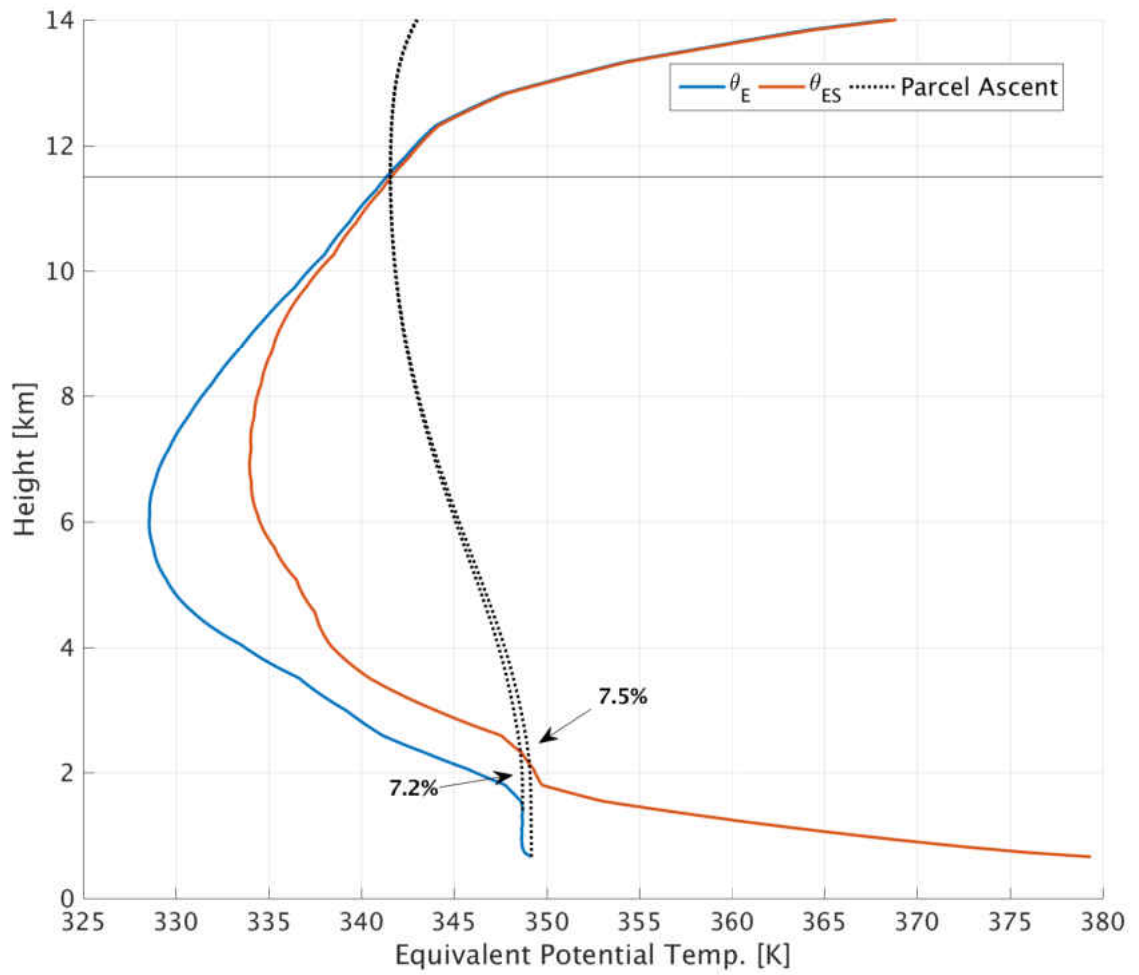


Figure 42: As in Figure 41 except for the deep convective case.



## CHAPTER 6

### SUMMARY AND CONCLUSIONS

The purpose of this study was to improve our understanding of convective mass transport by using a large number of readily-available observations to validate and better constrain model simulations. To achieve this goal: 1) high-resolution model forecasts were evaluated to investigate the accuracy of predicted convective structure and depth in order to identify any biases in model depictions of convection, 2) the first database of observed convective detrainment altitudes in the midlatitudes was built using ground-based radar observations, and 3) a framework was developed that constrains plume theory with observations to retrieve entrainment rates for observed deep convection.

Four months of WRF summertime convective-allowing forecasts using two different microphysical schemes (WSM6 and Thompson) were evaluated by comparing the simulated reflectivity field to the observed reflectivity field to investigate whether model simulations were able to correctly depict convective dynamics (and hence, mass transport; Chapter 2). By using the reflectivity field, the entire three-dimensional deep convective structure was evaluated to identify biases in simulated convection. Results showed that while the forecasted low-level convective structure looked very similar to observations, large differences were found aloft between forecasts and observations and between the two differing microphysical schemes, highlighting the importance of extending convective model verification into the vertical. The model forecasts contained a larger spread in reflectivity values, particularly aloft ( $\geq 5$  km),

and contained more than double the amount of convective cores reaching 6 and 10 km. Thompson forecasts were found to be significantly too intense and frequently had reflectivity values that were rarely or never seen in observations. Conversely, WSM6 forecasts were unable to represent the highest reflectivity magnitudes that were found in observed convection. A large sensitivity to the simulated reflectivity calculation scheme was also shown, illustrating that while the simulated reflectivity field can provide a general depiction of model performance it should not be relied on for specific storm properties.

Several radar stratification schemes have been previously developed for studies focusing on precipitation, which typically rely on strict thresholding applied to radar echo near the surface; however, there is a lack of stratification schemes for process-oriented or dynamical studies that require knowledge on the vertical extent and depth of convection. To account for this, a new radar echo stratification scheme that uses both single and dual-polarized radar observations and leverages three-dimensional information has been developed (Chapter 3). The SL3D algorithm classifies radar echo into five distinct dynamically and physically-based categories: updraft, convection, precipitating stratiform, non-precipitating stratiform, and (ice-only) anvil. Updrafts are objectively identified by locating weak echo regions and both  $Z_{DR}$  and  $K_{DP}$  columns when dual-polarization data is available, and were shown to correctly identify updrafts when compared against multi-Doppler derived vertical velocity. The SL3D algorithm was demonstrated on several cases of convection of different depths and in differing environments and compared to a traditional low-level stratification scheme, which revealed that SL3D was able to correctly classify weak convection that was missed by the traditional scheme and correctly identified intense stratiform that was misclassified as convection.

Observations of convective mass detrainment heights are uncommon due to many limitations in current observations platforms; therefore, limited observational datasets exist to constrain model simulations. A large observational dataset consisting of seven years of hourly radar composites for the months of May and July for four different regions was coupled with an anvil-proxy methodology to retrieve the LMD for convection in Chapter 4. Radar echo was stratified by the SL3D algorithm (Chapter 3) and the anvil near active convection was sampled to locate the convective LMD. Analysis of the mean LMD heights showed that May had higher tropopause-relative LMD heights but July contained the highest overall tropopause-relative LMD heights, suggesting potential for direct mass detrainment into the stratosphere. When convection was categorized into MCS or QISC morphology, QISC were found to commonly have LMD heights above the tropopause and had higher absolute and tropopause-relative LMD heights. Only a few MCS cases had LMD heights above the tropopause, but were found to have a wider detrainment envelope (based on comparing LMD heights to anvil top heights). When investigating regionality, the northern study regions were found to have higher overall mean tropopause-relative LMD heights than the southern regions. The southern regions were dominated by a large number of diurnally driven convective cells, particularly in July, which resulted in decreased the mean LMD detrainment heights.

One of the greatest impacts on convective detrainment heights is the entrainment of colder, drier (i.e., less buoyant) air into the convective updraft. To improve our understanding of entrainment and constrain convective models, a method was developed in Chapter 5 that uses observed convective and environmental properties to constrain plume theory. The method works by comparing an ideal non-mixing parcel to the observationally-derived mixing parcel, by comparing parcel buoyancy on soundings (idealized) to parcel buoyancy based on vertical velocity (observed). The

method also includes effects such as hydrometeor drag and ice phase latent heating. The methodology was demonstrated on modeled cases of shallow and deep convection and revealed that fractional entrainment rates varied up to a maximum of  $0.6 \text{ km}^{-1}$  and the average fractional entrainment rate was lower for deep convection. It was found that including the ice phase was essential for the retrieval of deep convective entrainment rates and accounting for hydrometeor drag improved the retrieval for the shallow convective cell. The retrieved fractional entrainment rates were compared against a traditional form of a constant entraining plume model that is commonly found in bulk plume cumulus parameterizations and it was found that the constant entrainment rates were lower by a factor of two to four.

This study also showcases the importance of incorporating vertical information into analysis of both modeled and observational datasets. Model biases were shown to differ between the near-surface and aloft, while analysis on one level may have led to broad and incorrect conclusions about model performance. By including vertical information, similarities and differences between simulated reflectivity calculations were revealed and illustrated the difficulty in depicting the simulated melting layer. Inclusion of volumetric radar data enabled stratification of radar echo in a dynamical and physically-based way, which was required to retrieve detrainment heights for convection of various depths and characteristics. Lastly, the traditional form of plume theory was expanded upon and constrained by including vertical observations of vertical velocity and environmental properties, which enabled the use of observations to retrieve fractional entrainment rates for deep convection that varied with height. All of the procedures and algorithms developed in this study are unspecific to region or season and can be applied anywhere where adequate radar observations exist.

The biases found in modeled convective structure showcase where convection-allowing models need more work and the methodology is now in place to enable large

intercomparisons of convective structure using different model physics and configurations. The identified biases can also provide further information on where the biases in the accumulated precipitation fields originate from. The convective detrainment altitudes retrieved from observations can be used to constrain the detrainment heights that are depicted by chemical transport models, and illustrate that convective morphology must be accounted for to capture the variability in observed detrainment heights. The retrieved detrainment heights also reveal that convection can transport mass directly into the stratosphere via the convective anvil. Furthermore, the distribution of detrainment heights can be used to estimate the amount of mass transported into the free troposphere and stratosphere by convection. The fractional entrainment retrieval methodology can be applied to a large observational dataset to retrieve a database of entrainment rates similar to the database of LMD heights collected in this study. Such large statistical datasets of observed entrainment rates are currently severely limited and largely unavailable, especially for deep convection, and would enable large-scale comparisons and provide constraints for cumulus parameterizations. The LMD height and detrainment envelope retrievals can be further coupled with the entrainment retrieval methodology to identify how much entrainment, and hence, parcel dilution must have occurred to different rising parcels in order to study the amount of boundary layer mass that can reach the UTLS.

## REFERENCES

- Adler, R. F., and R. A. Mack, 1984: Thunderstorm Cloud Height Rainfall Rate Relations for Use with Satellite Rainfall Estimation Techniques. **23** (2), 280–296, doi:10.1175/1520-0450(1984)023<0280:TCHRRF>2.0.CO;2.
- Adler, R. F., and A. J. Negri, 1988: A satellite infrared technique to estimate tropical convective and stratiform rainfall. *J. Appl. Meteor.*, **27**, 30–51, doi:10.1175/1520-0450(1988)027<0030:ASITTE>2.0.CO;2.
- Alexander, M. J., 2004: Gravity waves generated by convection in the Darwin area during the Darwin Area Wave Experiment. *J. Geophys. Res.*, **109** (D20), D20S04, doi:10.1029/2004JD004729.
- Anagnostou, E. N., 2004: A convective/stratiform precipitation classification algorithm for volume scanning weather radar observations. *Meteorol. Appl.*, **11** (4), 291–300, doi:10.1017/S1350482704001409.
- Anagnostou, E. N., and C. Kummerow, 1997: Stratiform and convective classification of rainfall using SSM/I 85-GHz brightness temperature observations. *J. Atmos. Oceanic Technol.*, **14** (3), 570–575, doi:10.1175/1520-0426(1997)014<0570:SACCOR>2.0.CO;2.

- Anderson, J. G., D. M. Wilmouth, J. B. Smith, and D. S. Sayres, 2012: UV Dosage Levels in Summer: Increased Risk of Ozone Loss from Convectively Injected Water Vapor. *Science*, **337** (6096), 835 – 839, doi:10.1126/science.1222978.
- Arakawa, A., 2004: The cumulus parameterization problem: Past, present, and future. *Journal of Climate*, **17** (13), 2493–2525, doi:10.1175/1520-0442(2004)017;2493:RATCPP;2.0.CO;2.
- Balakrishnan, N., and D. S. Zrnić, 1990: Estimates of rain and hail rates in mixed-phase precipitation. *J. Atmos. Sci.*, **47**, 565–583.
- Baldwin, M. E., and J. S. Kain, 2006: Sensitivity of Several Performance Measures to Displacement Error, Bias, and Event Frequency. *Weather and Forecasting*, **21** (4), 636–648, doi:10.1175/WAF933.1.
- Baray, J.-L., G. Ancellet, T. Randriambelo, and S. Baldy, 1999: Tropical cyclone marlene and stratosphere-troposphere exchange. *Journal of Geophysical Research: Atmospheres*, **104** (D11), 13 953–13 970, doi:10.1029/1999JD900028.
- Barber, K. A., G. L. Mullendore, and M. J. Alexander, 2018: Out-of-Cloud Convective Turbulence: Estimation Method and Impacts of Model Resolution. *Journal of Applied Meteorology and Climatology*, **57** (1), 121–136, doi:10.1175/JAMC-D-17-0174.1.
- Barth, M. C., S.-W. Kim, W. C. Skamarock, A. L. Stuart, K. E. Pickering, and L. E. Ott, 2007: Simulations of the redistribution of formaldehyde, formic acid, and peroxides in the 10 July 1996 Stratospheric-Tropospheric Experiment: Radiation, Aerosols, and Ozone deep convection storm. *Journal of Geophysical Research*, **112** (D13310), doi:10.1029/2006JD008046.

- Barth, M. C., and Coauthors, 2015: The Deep Convective Clouds and Chemistry (DC3) Field Campaign. *Bull. Amer. Meteorol. Soc.*, **96**, 1281–1309, doi:10.1175/BAMS-D-13-00290.1.
- Basarab, B. M., 2015: Prediction of total lightning in Colorado and Alabama thunderstorms based on storm dynamical and microphysical variables. *M. S. Thesis, Dept. of Atmos. Science, Colorado State University*, 109 pp.
- Basarab, B. M., S. A. Rutledge, and B. R. Fuchs, 2015: An improved lightning flash rate parameterization developed from Colorado DC3 thunderstorm data for use in cloud-resolving chemical transport models. *J. Geophys. Res. Atmos.*, **120**, 9481–9499.
- Bigelbach, B. C., G. L. Mullendore, and M. Starzec, 2014: Differences in deep convective transport characteristics between quasi-isolated strong convection and mesoscale convective systems using seasonal WRF simulations. *J. Geophys. Res.*, **119** (11), 445–455, doi:10.1002/2014JD021875.
- Biggerstaff, M. I., and S. A. Listemaa, 2000: An improved scheme for convective/stratiform echo classification using radar reflectivity. *J. Appl. Meteor.*, **39** (12), 2129–2150, doi:10.1175/1520-0450(2001)040<2129:AISFCS>2.0.CO;2.
- Bolton, D., 1980: The computation of equivalent potential temperature. *Monthly Weather Review*, **108** (7), 1046–1053, doi:10.1175/1520-0493(1980)108<1046:TCOEPT>2.0.CO;2.
- Brandes, E. A., J. Vivekanandan, J. D. Tuttle, and C. J. Kessinger, 1995: A study of thunderstorm microphysics with multiparameter radar and aircraft observations. *Mon. Wea. Rev.*, **123** (11), 3129–3143, doi:10.1175/1520-0493(1995)123<3129:asotmw>2.0.co;2.



- Braun, S. A., and R. A. Houze, 1994: The transition zone and secondary maximum of radar reflectivity behind a midlatitude squall line: Results retrieved from doppler-radar data. *J. Atmos. Sci.*, **51**, 2733–2755.
- Bringi, V. N., D. A. Burrows, and S. M. Menon, 1991: Multiparameter radar and aircraft study of raindrop spectral evolution in warm-based clouds. *J. Appl. Meteor.*, **30**, 853–880.
- Bringi, V. N., and V. Chandrasekar, 2001: *Polarimetric Doppler Weather Radar*. 1st ed., Cambridge University Press.
- Bringi, V. N., C. R. Williams, M. Thurai, and P. T. May, 2009: Using dual-polarized radar and dual-frequency profiler for DSD characterization: A case study from Darwin, Australia. *J. Atmos. Oceanic Technol.*, **26** (10), 2107–2122, doi:10.1175/2009JTECHA1258.1.
- Browning, K. A., and R. J. Donaldson, 1963: Airflow and structure of a tornadic storm. *J. Atmos. Sci.*, **20**, 533–545.
- Browning, K. A., J. C. Nicol, J. H. Marsham, P. Rogberg, and E. G. Norton, 2011: Layers of insect echoes near a thunderstorm and implications for the interpretation of radar data in terms of airflow. *Quarterly Journal of the Royal Meteorological Society*, **137** (656), 723–735, doi:10.1002/qj.800.
- Bryan, G. H., and J. M. Fritsch, 2002: A benchmark simulation for moist nonhydrostatic numerical models. *Monthly Weather Review*, **130** (12), 2917–2928, doi:10.1175/1520-0493(2002)130<2917:ABSFMN>2.0.CO;2.
- Burghardt, B. J., C. Evans, and P. J. Roebber, 2014: Assessing the Predictability of Convection Initiation in the High Plains Using an Object-Based Approach. *Weather and Forecasting*, **29** (2), 403–418, doi:10.1175/WAF-D-13-00089.1.

- Cai, H., and R. E. Dumais, 2015: Object-Based Evaluation of a Numerical Weather Prediction Model's Performance through Forecast Storm Characteristic Analysis. *Weather and Forecasting*, **30** (6), 1451–1468, doi:10.1175/WAF-D-15-0008.1.
- Caine, S., T. P. Lane, P. T. May, C. Jakob, S. T. Siems, M. J. Manton, and J. Pinto, 2013: Statistical Assessment of Tropical Convection-Permitting Model Simulations Using a Cell-Tracking Algorithm. *Monthly Weather Review*, **141** (2), 557–581, doi:10.1175/MWR-D-11-00274.1.
- Calhoun, K. M., D. R. MacGorman, C. L. Ziegler, and M. I. Biggerstaff, 2013: Evolution of lightning activity and storm charge relative to dual-doppler analysis of a high-precipitation supercell storm. *Mon. Wea. Rev.*, **141**, 2199–2223, doi:10.1175/MWR-D-12-00258.1.
- Carletta, N. D., G. L. Mullendore, M. Starzec, B. Xi, Z. Feng, and X. Dong, 2016: Determining best method for estimating observed level of maximum convective detrainment based on radar reflectivity. *Mon. Wea. Rev.*, 2915–2926.
- Caylor, I. J., and A. J. Illingworth, 1987: Radar observations and modeling of warm rain initiation. *Q. J. R. Meteorol. Soc.*, **113**, 1171–1191, doi:10.1002/qj.49711347806.
- Cess, R. D., and Coauthors, 1990: Cloud feedback in atmospheric general circulation models: An update. *Journal of Geophysical Research: Atmospheres*, **101** (D8), 12 791–12 794, doi:10.1029/96JD00822.
- Cess, R. D., and Coauthors, 1996: Intercomparison and interpretation of climate feedback processes in 19 atmospheric general circulation models. *Journal of Geophysical Research: Atmospheres*, **95** (D10), 16 601–16 615, doi:10.1029/JD095iD10p16601.

- Churchill, D. D., and R. A. Houze, 1984: Development and structure of winter monsoon cloud clusters on 10 december 1978. *J. Atmos. Sci.*, **41** (6), 933–960.
- Clark, A. J., R. G. Bullock, T. L. Jensen, M. Xue, and F. Kong, 2014: Application of Object-Based Time-Domain Diagnostics for Tracking Precipitation Systems in Convection-Allowing Models. *Weather and Forecasting*, **29** (3), 517–542, doi:10.1175/WAF-D-13-00098.1.
- Clark, A. J., and Coauthors, 2012: An overview of the 2010 Hazardous Weather Testbed experimental forecast program spring experiment. *Bulletin of the American Meteorological Society*, **93** (1), 55–74, doi:10.1175/bAms-d-11-00040.1.
- Collis, S., A. Protat, P. T. May, and C. Williams, 2013: Statistics of storm updraft velocities from TWP-ICE including verification with profiling measurements. *J. Appl. Meteor. Climatol.*, **52**, 1909–1922.
- Conway, J. W., and D. S. Zrnić, 1993: A study of embryo production and hail growth using dual-doppler and multiparameter radars. *Mon. Wea. Rev.*, **121** (9), 2511–2528, doi:10.1175/1520-0493(1993)121;2511:ASOEPA;2.0.CO;2.
- Cooper, O. R., and Coauthors, 2006: Large upper tropospheric ozone enhancements above midlatitude north america during summer: In situ evidence from the ions and mozaic ozone measurement network. *Journal of Geophysical Research: Atmospheres*, **111** (D24), doi:10.1029/2006JD007306.
- Crum, T. D., and R. L. Alberty, 1993: The WSR-88D and the WSR-88D operational support facility. *Bull. Amer. Meteor. Soc.*, **74** (9), 1669–1687.
- Cunningham, J. G., W. D. Zittel, R. R. Lee, and R. L. Ice, 2013: Methods for identifying systematic differential reflectivity ( $Z_{DR}$ ) biases on the operational WSR-88D network. *36th Conf. on Radar Meteorology*, Amer. Meteor. Soc., 9B.5.

- Davis, C., B. Brown, and R. Bullock, 2006: Object-Based Verification of Precipitation Forecasts. Part I: Methodology and Application to Mesoscale Rain Areas. *Monthly Weather Review*, **134** (7), 1772–1784, doi:10.1175/MWR3145.1.
- Davis, C. a., B. G. Brown, R. Bullock, and J. Halley-Gotway, 2009: The Method for Object-Based Diagnostic Evaluation (MODE) Applied to Numerical Forecasts from the 2005 NSSL/SPC Spring Program. *Weather and Forecasting*, **24**, 1252–1267, doi:10.1175/2009WAF2222241.1.
- Dawe, J. T., and P. H. Austin, 2011: Interpolation of les cloud surfaces for use in direct calculations of entrainment and detrainment. *Monthly Weather Review*, **139** (2), 444–456, doi:10.1175/2010MWR3473.1.
- de Rooy, W. C., and Coauthors, 2006: Entrainment and detrainment in cumulus convection: an overview. *Quarterly Journal of the Royal Meteorological Society*, **139** (670), 1–19, doi:10.1002/qj.1959.
- DeCaria, A. J., K. E. Pickering, G. L. Stenchikov, and L. E. Ott, 2005: Lightning-generated nox and its impact on tropospheric ozone production: A three-dimensional modeling study of a stratosphere-troposphere experiment: Radiation, aerosols and ozone (sterao-a) thunderstorm. *Journal of Geophysical Research: Atmospheres*, **110** (D14), doi:10.1029/2004JD005556.
- Dee, D. P., and Coauthors, 2011: The era-interim reanalysis: configuration and performance of the data assimilation system. *Quarterly Journal of the Royal Meteorological Society*, **137** (656), 553–597, doi:10.1002/qj.828.
- Del Genio, A. D., and J. Wu, 2010: The role of entrainment in the diurnal cycle of continental convection. *Journal of Climate*, **23** (10), 2722–2738, doi:10.1175/2009JCLI3340.1.

- DeMott, C. A., R. Cifelli, and S. A. Rutledge, 1995: An improved method for partitioning radar data into convective and stratiform components. *27th Conf. Radar Meteorol.*, 236–266.
- DeMott, C. A., and S. A. Rutledge, 1998: The vertical structure of TOGA COARE convection. Part I: radar echo distribution. *J. Atmos. Sci.*, **55**, 2730–2747.
- Dickerson, R. R., and Coauthors, 1987: Thunderstorms: An Important Mechanism in the Transport of Air Pollutants. *Science*, **235** (4787), 460–465.
- Dixon, M., 2010: Radx C++ Software Package. NCAR.
- Donavon, R. A., and K. A. Jungbluth, 2007: Evaluation of a Technique for Radar Identification of Large Hail across the Upper Midwest and Central Plains of the United States. *Weather and Forecasting*, **22** (2), 244–254, doi:10.1175/WAF1008.1.
- Doviak, R. J., and D. S. Zrnić, 1993: *Doppler Radar and Weather Observations*. 2nd ed., Dover, 562 pp.
- Doviak, R. J., and D. S. Zrnić, 1993: *Doppler Radar and Weather Observations*. 2nd ed., ISBN 0-486-45060-0, Dover Publications, Inc., 31 East 2nd Street, Mineola, NY, 11501.
- Drdla, K., and R. Müller, 2012: Temperature thresholds for chlorine activation and ozone loss in the polar stratosphere. *Annales Geophysicae*, **30** (7), 1055–1073, doi:10.5194/angeo-30-1055-2012, URL <https://www.ann-geophys.net/30/1055/2012/>.
- Ebel, A., H. Hass, H. Jakobs, M. Laube, M. Memmesheimer, A. Oberreuter, H. Geiss, and Y.-H. Kuo, 1991: Simulation of ozone intrusion caused by a tropopause fold

- and cut-off low. *Atmospheric Environment. Part A. General Topics*, **25** (10), 2131–2144, doi:[https://doi.org/10.1016/0960-1686\(91\)90089-P](https://doi.org/10.1016/0960-1686(91)90089-P).
- Ebert, E. E., and W. A. Gallus, 2009: Toward Better Understanding of the Contiguous Rain Area (CRA) Method for Spatial Forecast Verification. *Weather and Forecasting*, **24** (5), 1401–1415, doi:10.1175/2009WAF2222252.1.
- Ebert, E. E., and J. L. McBride, 2000: Verification of precipitation in weather systems: Determination of systematic errors. *Journal of Hydrology*, **239** (1-4), 179–202, doi:10.1016/S0022-1694(00)00343-7.
- Fabian, P., and P. G. Pruchniewicz, 1977: Meridional distribution of ozone in the troposphere and its seasonal variations. *Journal of Geophysical Research*, **82** (15), 2063–2073, doi:10.1029/JC082i015p02063.
- Feng, Z., X. Dong, B. Xi, C. Schumacher, P. Minnis, and M. Khaiyer, 2011: Top-of-atmosphere radiation budget of convective core/stratiform rain and anvil clouds from deep convective systems. *J. Geophys. Res.*, **116** (23), 1–13, doi:10.1029/2011JD016451.
- Fischer, H., and Coauthors, 2003: Deep convective injection of boundary layer air into the lowermost stratosphere at midlatitudes. *Atmospheric Chemistry and Physics*, **3**, 739–745.
- Forster, P. M. d. F., and K. P. Shine, 1999: Stratospheric water vapour changes as a possible contributor to observed stratospheric cooling. *Geophysical Research Letters*, **26** (21), 3309–3312, doi:10.1029/1999GL010487.
- Frederick, K., and C. Schumacher, 2008: Anvil characteristics as seen by C-POL during the Tropical Warm Pool International Cloud Experiment (TWP-ICE). *Mon. Wea. Rev.*, **136**, 206–222.

- Fujiwara, M., K. Kita, and T. Ogawa, 1998: Stratosphere-troposphere exchange of ozone associated with the equatorial kelvin wave as observed with ozonesondes and rawinsondes. *Journal of Geophysical Research: Atmospheres*, **103 (D15)**, 19 173–19 182, doi:10.1029/98JD01419.
- Gallus, W. A., 2010: Application of Object-Based Verification Techniques to Ensemble Precipitation Forecasts. *Weather and Forecasting*, **25 (1)**, 144–158, doi:10.1175/2009waf2222274.1.
- Gerber, H. E., G. M. Frick, J. B. Jensen, and J. G. Hudson, 2008: Entrainment, mixing, and microphysics in trade-wind cumulus. *Journal of the Meteorological Society of Japan. Ser. II*, **86A**, 87–106, doi:10.2151/jmsj.86A.87.
- Ghude, S. D., and Coauthors, 2016: Premature mortality in india due to pm2.5 and ozone exposure. *Geophysical Research Letters*, **43 (9)**, 4650–4658, doi:10.1002/2016GL068949.
- Giangrande, S. E., J. M. Krause, and A. V. Ryzhkov, 2008: Automatic designation of the melting layer with a polarimetric prototype of the WSR-88D Radar. *J. Appl. Meteor.*, **47**, 1354–1364.
- Gregory, D., 2001: Estimation of entrainment rate in simple models of convective clouds. *Quarterly Journal of the Royal Meteorological Society*, **127 (571)**, 53–72, doi:10.1002/qj.49712757104.
- Griffin, S. M., J. A. Otkin, C. M. Rozoff, J. M. Sieglaff, L. M. Cronic, and C. R. Alexander, 2017: Methods for Comparing Simulated and Observed Satellite Infrared Brightness Temperatures and What Do They Tell Us? *Weather and Forecasting*, **32 (1)**, 5–25, doi:10.1175/WAF-D-16-0098.1.

- Guo, X., C. Lu, T. Zhao, G. J. Zhang, and Y. Liu, 2015: An observational study of entrainment rate in deep convection. *Atmosphere*, **6**, 1362–1376.
- Hassim, M. E. E., and T. P. Lane, 2010: A model study on the influence of overshooting convection on ttl water vapour. *Atmospheric Chemistry and Physics*, **10** (20), 9833–9849, doi:10.5194/acp-10-9833-2010.
- Hegglin, M. I., and Coauthors, 2004: Tracing troposphere-to-stratosphere transport above a mid-latitude deep convective system. *Atmospheric Chemistry and Physics*, **4**, 741–756.
- Held, G., 1978: The Probability of Hail in Realtion to Radar Echo Hights. *Journal of Applied Meteorology*, **17**, 755 – 762.
- Herzogh, P. H., and A. R. Jameson, 1992: Observing precipitation through dual-polarization radar measurements. *Bull. Amer. Meteor. Soc.*, **73**, 1365–1374.
- Heus, T., and H. J. J. Jonker, 2008: Subsiding shells around shallow cumulus clouds. *Journal of the Atmospheric Sciences*, **65** (3), 1003–1018, doi:10.1175/2007JAS2322.1.
- Hints, E. J., and Coauthors, 1998: Troposphere-to-stratosphere transport in the lowermost stratosphere from measurements of h<sub>2</sub>o, co<sub>2</sub>, n<sub>2</sub>o and o<sub>3</sub>. *Geophysical Research Letters*, **25** (14), 2655–2658, doi:10.1029/98GL01797.
- Holton, J. R., P. H. Haynes, M. E. McIntyre, A. R. Douglass, R. B. Rood, and L. Pfister, 1995: Stratosphere-troposphere exchange. *Reviews of Geophysics*, **33** (4), 403–439, doi:10.1029/95RG02097.



- Homeyer, C. R., 2014: Formation of the enhanced-v infrared cloud-top feature from high-resolution three-dimensional radar observations. *J. Atmos. Sci.*, **71** (1), 332–348, doi:10.1175/JAS-D-13-079.1.
- Homeyer, C. R., K. P. Bowman, and L. L. Pan, 2010: Extratropical tropopause transition layer characteristics from high-resolution sounding data. *Journal of Geophysical Research: Atmospheres*, **115** (D13), doi:10.1029/2009JD013664.
- Homeyer, C. R., K. P. Bowman, L. L. Pan, E. L. Atlas, R.-S. Gao, and T. L. Campos, 2011: Dynamical and chemical characteristics of tropospheric intrusions observed during start08. *Journal of Geophysical Research: Atmospheres*, **116** (D6), doi:10.1029/2010JD015098.
- Homeyer, C. R., and M. R. Kumjian, 2015: Microphysical characteristics of overshooting convection from polarimetric radar observations. *J. Atmos. Sci.*, **72**, 870–891, doi:10.1175/JAS-D-13-0388.1.
- Homeyer, C. R., and Coauthors, 2014: Convective transport of water vapor into the lower stratosphere observed during double-tropopause events. *J. Geophys. Res.*, **119**, 10 941–10 958, doi:10.1002/2014JD021485.
- Hong, S.-Y., and J.-O. J. Lim, 2006: The WRF single-moment 6-class microphysics scheme (WSM6). *Journal of the Korean Meteorological Society*, **42**, 129–151.
- Hong, Y., C. D. Kummerow, and W. S. Olson, 1999: Separation of convective and stratiform precipitation using microwave brightness temperature. *J. Appl. Meteor.*, **38** (8), 1195–1213, doi:10.1175/1520-0450(1999)038<1195:SOCASP>2.0.CO;2.
- Houghton, H. G., 1968: On precipitation mechanisms and their artificial modification. *J. Appl. Meteor.*, **7**, 851–859.

- Houze, R. A., 1989: Observed structure of mesoscale convective systems and implications for large-scale heating. *Quarterly Journal of the Royal Meteorological Society*, **115**, 425–461.
- Houze, R. A., 1993: *Cloud Dynamics*. 3rd ed., Academic Press.
- Houze, R. A., 1997: Stratiform precipitation in regions of convection: A meteorological paradox? *Bull. Amer. Meteor. Soc.*, **78**, 2179–2196.
- Huntrieser, H., and Coauthors, 2016: On the origin of pronounced O<sub>3</sub> gradients in the thunderstorm outflow region during DC3. *Journal of Geophysical Research: Atmospheres*, **121** (11), 6600–6637, doi:10.1002/2015JD024279.
- Illingworth, A. J., 1988: The formation of rain in convective clouds. *Nature*, **336**, 754–756, doi:10.1038/336754a0.
- IPCC, 2013: Climate change 2013: The physical science basis. contribution of working group I to the fifth assessment report of the intergovernmental panel on climate change. Cambridge University Press, Cambridge, United Kingdom and New York, NY, USA, 1535 pp.
- Jacob, D. J., and Coauthors, 1993: Simulation of summertime ozone over north america. *Journal of Geophysical Research: Atmospheres*, **98** (D8), 14 797–14 816, doi:10.1029/93JD01223.
- Jensen, M. P., and A. D. Del Genio, 2006: Factors limiting convective cloud-top height at the ARM Nauru Island Climate Research Facility. *Journal of Climate*, **19** (10), 2105–2117, doi:10.1175/JCLI3722.1.

- Jensen, T. L., and Coauthors, 2010: An Overview of the Objective Evaluation Performed During the Hazardous Weather Testbed (HWT) 2010 Spring Experiment. *Preprints*, 7, doi:10.1017/CBO9781107415324.004, arXiv:1011.1669v3.
- Jiang, J. H., N. J. Livesey, H. Su, L. Neary, J. C. McConnell, and N. A. D. Richards, 2007: Connecting surface emissions, convective uplifting, and long-range transport of carbon monoxide in the upper troposphere: New observations from the aura microwave limb sounder. *Geophysical Research Letters*, **34** (18), doi:10.1029/2007GL030638.
- Johnson, A., and X. Wang, 2013: Object-Based Evaluation of a Storm-Scale Ensemble during the 2009 NOAA Hazardous Weather Testbed Spring Experiment. *Monthly Weather Review*, **141** (3), 1079–1098, doi:10.1175/MWR-D-12-00140.1.
- Johnson, A., X. Wang, F. Kong, and M. Xue, 2013: Object-Based Evaluation of the Impact of Horizontal Grid Spacing on Convection-Allowing Forecasts. *Monthly Weather Review*, **141** (10), 3413–3425, doi:10.1175/MWR-D-13-00027.1.
- Johnson, R. H., 1984: Partitioning tropical heat and moisture budgets into cumulus and mesoscale components: Implications for cumulus parameterization. *Mon. Wea. Rev.*, **112** (8), 1590–1601, doi:10.1175/1520-0493(1984)112;1590:PTHAMB;2.0.CO;2.
- Jorgensen, D. P., M. A. LeMone, and S. B. Trier, 1997: Structure and evolution of the 22 February 1993 TOGA COARE squall line: Aircraft observations of precipitation, circulation, and surface energy fluxes. *J. Atmos. Sci.*, **54**, 1961–1985.
- Kain, J. S., and Coauthors, 2008: Some Practical Considerations Regarding Horizontal Resolution in the First Generation of Operational Convection-Allowing NWP. *Weather and Forecasting*, **23** (5), 931–952, doi:10.1175/WAF2007106.1.

- Kain, J. S., and Coauthors, 2010: Assessing Advances in the Assimilation of Radar Data and Other Mesoscale Observations within a Collaborative Forecasting Research Environment. *Weather and Forecasting*, **25** (5), 1510–1521, doi:10.1175/2010WAF2222405.1.
- Khairoutdinov, M., and D. Randall, 2006: High-resolution simulation of shallow-to-deep convection transition over land. *Journal of the Atmospheric Sciences*, **63** (12), 3421–3436, doi:10.1175/JAS3810.1.
- Kirk-Davidoff, D. B., E. J. Hints, J. G. Anderson, and D. W. Keith, 1999: The effect of climate change on ozone depletion through changes in stratospheric water vapour. *Nature*, **402**, 401–499.
- Koch, S. E., B. S. Ferrier, M. T. Stoelinga, E. Szoke, S. J. Weiss, and J. S. Kain, 2005: The Use of Simulated Radar Reflectivity Fields in the Diagnosis of Mesoscale Phenomena from High-Resolution WRF Model Forecasts. *11th Conf. on Mesoscale Processes and 32nd Conf. on Radar Meteorology*, 1–9.
- Kumjian, M. R., 2013a: Principles and Applications of Dual-Polarization Weather Radar. Part I: Description of the Polarimetric Radar Variables. *Journal of Operational Meteorology*, **1** (19), 226–242, doi:10.15191/nwajom.2013.0119.
- Kumjian, M. R., 2013b: Principles and applications of dual-polarization weather radar. Part II: Warm- and cold-season applications. *Journal of Operational Meteorology*, **1** (20), 243–264, doi:10.15191/nwajom.2013.0120.
- Kumjian, M. R., 2013c: Principles and applications of dual-polarization weather radar. Part III: Artifacts. *Journal of Operational Meteorology*, **1** (21), 265–274, doi:10.15191/nwajom.2013.0121.

- Kumjian, M. R., A. P. Khain, N. Benmoshe, E. Ilotoviz, A. V. Ryzhkov, and V. T. J. Phillips, 2014: The anatomy and physics of  $Z_{DR}$  columns: Investigating a polarimetric radar signature with a spectral bin microphysical model. *J. Appl. Meteor. Climatol.*, **53** (7), 1820–1843, doi:10.1175/JAMC-D-13-0354.1.
- Kumjian, M. R., and A. V. Ryzhkov, 2008: Polarimetric signatures in supercell thunderstorms. *J. Appl. Meteor. Climatol.*, **47** (7), 1940–1961, doi:10.1175/2007JAMC1874.1.
- Kuo, Y.-H., and R. A. Anthes, 1984: Mesoscale budgets of heat and moisture in a convective system over the Central United States. *Mon. Wea. Rev.*, **112**, 1482–1497.
- Lakshmanan, V., J. Zhang, and K. Howard, 2010: A technique to censor biological echoes in radar reflectivity data. *Journal of Applied Meteorology and Climatology*, **49** (3), 453–462, doi:10.1175/2009JAMC2255.1.
- Lane, T. P., R. D. Sharman, T. L. Clark, and H.-M. Hsu, 2003: An Investigation of Turbulence Generation Mechanisms above Deep Convection. *Journal of the Atmospheric Sciences*, **60** (10), 1297–1321, doi:10.1175/1520-0469(2003)60<1297:aiotgmj>2.0.co;2.
- Lang, T. J., and S. A. Rutledge, 2002: Relationships between convective storm kinematics, precipitation, and lightning. *Mon. Wea. Rev.*, **130**, 2492–2506.
- Lang, T. J., and S. A. Rutledge, 2008: Kinematic, microphysical, and electrical aspects of an asymmetric bow-echo mesoscale convective system observed during STEPS 2000. *J. Geophys. Res.*, **113**, D08 213, doi:10.1029/2006JD007709.
- Lang, T. J., and Coauthors, 2004: Prediction of total lightning in Colorado and Alabama thunderstorms based on storm dynamical and microphysical variables. *Bull. Amer. Meteorol. Soc.*, **85**, 1107–1125.

- Lawrence, M. G., R. von Kuhlmann, M. Salzmann, and P. J. Rasch, 2003: The balance of effects of deep convective mixing on tropospheric ozone. *Geophysical Research Letters*, **30** (18), doi:10.1029/2003GL017644.
- Leary, C. A., and R. A. Houze, 1979: Melting and evaporation of hydrometeors in precipitation from the anvil clouds of deep tropical convection. *Journal of the Atmospheric Sciences*, **36** (4), 669–679.
- Lin, M., and Coauthors, 2012: Springtime high surface ozone events over the western united states: Quantifying the role of stratospheric intrusions. *Journal of Geophysical Research: Atmospheres*, **117** (D21), doi:10.1029/2012JD018151.
- Liu, S. C., M. Trainer, F. C. Fehsenfeld, D. D. Parrish, E. J. Williams, D. W. Fahey, G. Hbler, and P. C. Murphy, 1987: Ozone production in the rural troposphere and the implications for regional and global ozone distributions. *Journal of Geophysical Research: Atmospheres*, **92** (D4), 4191–4207, doi:10.1029/JD092iD04p04191.
- Loney, M. L., D. S. Zrnić, J. M. Straka, and A. V. Ryzhkov, 2002: Enhanced polarimetric radar signatures above the melting level in a supercell storm. *J. Appl. Meteor.*, **1** (V), 1179–1194, doi:10.1109/IGARSS.2002.1025018.
- Lu, C., Y. Liu, S. S. Yum, S. Niu, and S. Endo, 2012: A new approach for estimating entrainment rate in cumulus clouds. *Geophysical Research Letters*, **39** (4), doi:10.1029/2011GL050546.
- Maddox, E. M., and G. L. Mullendore, 2018: Determination of best tropopause definition for convective transport studies. *Journal of the Atmospheric Sciences*, **75** (10), 3433–3446, doi:10.1175/JAS-D-18-0032.1.

- Mapes, B., and R. A. Houze, 1993: An integrated view of the 1987 Australian monsoon and its mesoscale convective systems. II: Vertical structure. *Q. J. R. Meteorol. Soc.*, **119**, 733–754.
- Markowski, P., and Y. Richardson, 2010: *Mesoscale Meteorology in Midlatitudes*. Wiley-Blackwell, 424 pp.
- Markowski, P. M., 2002: Hook echoes and rear-flank downdrafts: A review. *Mon. Wea. Rev.*, **130** (4), 852–876, doi:10.1175/1520-0493(2002)130<0852:HEARFD>2.0.CO;2.
- Mass, C. F., D. Ovens, K. Westrick, and B. A. Colle, 2002: Does Increasing Horizontal Resolution Produce More Skillful Forecasts? *Bulletin of the American Meteorological Society*, **83**, 407–430, doi:http://dx.doi.org/10.1175/1520-0477(2002)083.
- Min, K.-H., S. Choo, D. Lee, and G. Lee, 2015: Evaluation of WRF Cloud Microphysics Schemes Using Radar Observations. *Weather and Forecasting*, **30** (6), 1571–1589, doi:10.1175/WAF-D-14-00095.1.
- Mittermaier, M. P., 2014: A Strategy for Verifying Near-Convection-Resolving Model Forecasts at Observing Sites. *Weather and Forecasting*, **29** (2), 185–204, doi:10.1175/WAF-D-12-00075.1.
- Morrison, H., 2016: Impacts of updraft size and dimensionality on the perturbation pressure and vertical velocity in cumulus convection. part ii: Comparison of theoretical and numerical solutions and fully dynamical simulations. *Journal of the Atmospheric Sciences*, **73** (4), 1455–1480, doi:10.1175/JAS-D-15-0041.1.
- Morrison, H., G. Thompson, and V. Tatarskii, 2009: Impact of Cloud Microphysics on the Development of Trailing Stratiform Precipitation in a Simulated Squall

- Line: Comparison of One- and Two-Moment Schemes. *Monthly Weather Review*, **137 (3)**, 991–1007, doi:10.1175/2008MWR2556.1.
- Moser, D. H., and S. Lasher-Trapp, 2017: The influence of successive thermals on entrainment and dilution in a simulated cumulus congestus. *Journal of the Atmospheric Sciences*, **74 (2)**, 375–392, doi:10.1175/JAS-D-16-0144.1.
- Mote, P. W., and Coauthors, 1996: An atmospheric tape recorder: The imprint of tropical tropopause temperatures on stratospheric water vapor. *Journal of Geophysical Research*, **101 (D2)**, 3989–4006.
- Mullendore, G. L., D. R. Durran, and J. R. Holton, 2005: Cross-tropopause tracer transport in midlatitude convection. *Journal of Geophysical Research: Atmospheres*, **110**, 1–14, doi:10.1029/2004JD005059.
- Mullendore, G. L., A. J. Homann, K. Bevers, and C. Schumacher, 2009: Radar reflectivity as a proxy for convective mass transport. *J. Geophys. Res.*, **114 (D16)**, 1–8, doi:10.1029/2008jd011431.
- Mullendore, G. L., A. J. Homann, S. T. Jorgenson, T. J. Lang, and S. A. Tessendorf, 2013: Relationship between level of neutral buoyancy and dual-doppler observed mass detrainment levels in deep convection. *Atmospheric Chemistry and Physics*, **13 (1)**, 181–190, doi:10.5194/acp-13-181-2013.
- Musil, D. J., A. J. Heymsfield, and P. L. Smith, 1986: Microphysical characteristics of a well-developed weak echo region in a High Plains supercell thunderstorm. *J. Clim. Appl. Meteor.*, **25 (7)**, 1037–1051, doi:10.1175/1520-0450(1986)025<1037:MCOAWD>2.0.CO;2.



- NOAA National Weather Service, R. O. C., 1991: NOAA Next Generation Radar (NEXRAD) Level II Base Data. NOAA National Centers for Environmental Information, accessed May 2015 to January 2016, doi:10.7289/V5W9574V.
- North, K. W., M. Oue, P. Kollias, S. E. Giangrande, S. M. Collis, and C. K. Potvin, 2017: Vertical air motion retrievals in deep convective clouds using the arm scanning radar network in oklahoma during mc3e. *Atmospheric Measurement Techniques*, **10** (8), 2785–2806, doi:10.5194/amt-10-2785-2017, URL <https://www.atmos-meas-tech.net/10/2785/2017/>.
- Nuret, M., and M. Chong, 1998: Characteristics of heat and moisture budgets of a mesoscale convective system observed during TOGA-COARE. *Q. J. R. Meteorol. Soc.*, **124** (548), 1163–1181.
- O'Brien, J. J., 1970: Alternative solutions to the classical vertical velocity problem. *J. Appl. Meteor.*, **9**, 197–203.
- Ott, L. E., K. E. Pickering, G. L. Stenchikov, H. Huntrieser, and U. Schumann, 2007: Effects of lightning nox production during the 21 july european lightning nitrogen oxides project storm studied with a three-dimensional cloud-scale chemical transport model. *Journal of Geophysical Research: Atmospheres*, **112** (D5), doi:10.1029/2006JD007365.
- Oue, M., P. Kollias, A. Tatarevis, K. W. North, T. Matsui, A. M. Fridlind, D. Wang, and K. Yu, 2018: State of 3d convective vertical velocity retrievals at the arm sites: Challenges, uncertainties and future recommendations. *2018 Joint ARM-ASR Conference*, Tysons Corner, VA.

- Paluch, I. R., 1979: The entrainment mechanism in colorado cumuli. *Journal of the Atmospheric Sciences*, **36** (12), 2467–2478, doi:10.1175/1520-0469(1979)036<2467:TEMICC>2.0.CO;2.
- Pan, L. L., and Coauthors, 2010: The stratospheretroposphere analyses of regional transport 2008 experiment. *Bulletin of the American Meteorological Society*, **91** (3), 327–342, doi:10.1175/2009BAMS2865.1.
- Park, H., A. V. Ryzhkov, D. S. Zrníc, and K.-E. Kim, 2009: The hydrometeor classification algorithm for the polarimetric WSR-88D: Description and application to an MCS. *Wea. Forecasting*, **24**, 730–748, doi:10.1175/2008WAF2222205.1.
- Pessi, A. T., and S. Businger, 2009: Relationships among lightning, precipitation, and hydrometeor characteristics over the North Pacific Ocean. *Journal of Applied Meteorology and Climatology*, **48** (4), 833–848, doi:10.1175/2008JAMC1817.1.
- Pickering, K. E., R. R. Dickerson, G. J. Huffman, J. F. Boatman, and A. Schanot, 1988: Trace gas transport in the vicinity of frontal convective clouds. *Journal of Geophysical Research: Atmospheres*, **93** (D1), 759–773, doi:10.1029/JD093iD01p00759.
- Pickering, K. E., and Coauthors, 1996: Convective transport of biomass burning emissions over Brazil during TRACE A. *Journal of Geophysical Research*, **101**, 22 993–24 012.
- Pinto, J. O., J. a. Grim, and M. Steiner, 2015: Assessment of the High-Resolution Rapid Refresh Model’s Ability to Predict Mesoscale Convective Systems Using Object-Based Evaluation. *Weather and Forecasting*, **30** (4), 892–913, doi:10.1175/WAF-D-14-00118.1.

- Plumb, R. A., 1996: A "tropical pipe" model of stratospheric transport. *Journal of Geophysical Research*, **101**, 3957–3972.
- Poulida, O., R. R. Dickerson, and A. Heymsfield, 1996: Stratosphere-troposphere exchange in a midlatitude mesoscale convective complex 1. Observations. *Journal of Geophysical Research*, **101 (D03523)**, 6823–6839.
- Powell, S. W., and R. A. Houze, 2015: Evolution of precipitation and convective echo top heights observed by TRMM radar over the Indian ocean during DYNAMO. *Journal of Geophysical Research*, **120 (9)**, 3906–3919, doi:10.1002/2014JD022934.
- Powell, S. W., R. A. Houze, and S. R. Brodzik, 2016: Rainfall-type categorization of radar echoes using polar coordinate reflectivity data. *J. Atmos. Oceanic Technol.*, **33**, 523–538.
- Ramaswamy, V., M. D. Schwarzkopf, and K. P. Shine, 1992: Radiative forcing of climate from halocarbon-induced global stratospheric ozone loss. *Nature*, **355**, 810–812.
- Randall, D., M. Khairoutdinov, A. Arakawa, and W. Grabowski, 2003: Breaking the cloud parameterization deadlock. *Bulletin of the American Meteorological Society*, **84 (11)**, 1547–1564, doi:10.1175/BAMS-84-11-1547.
- Rogers, R. F., M. L. Black, S. S. Chen, and R. A. Black, 2007: An Evaluation of Microphysics Fields from Mesoscale Model Simulations of Tropical Cyclones. Part I: Comparisons with Observations. *Journal of the Atmospheric Sciences*, **64 (6)**, 1811–1834, doi:10.1175/JAS3932.1.
- Romps, D. M., 2010: A direct measure of entrainment. *Journal of the Atmospheric Sciences*, **67 (6)**, 1908–1927, doi:10.1175/2010JAS3371.1.

- Rybka, H., and H. Tost, 2014: Uncertainties in future climate predictions due to convection parameterisations. *Atmospheric Chemistry and Physics*, **14** (11), 5561–5576, doi:10.5194/acp-14-5561-2014, URL <https://www.atmos-chem-phys.net/14/5561/2014/>.
- Ryzhkov, A. V., S. E. Giangrande, V. M. Melnikov, and T. J. Schuur, 2005a: Calibration issues of dual-polarization radar measurements. *J. Atmos. Oceanic Technol.*, **22**, 1138–1155.
- Ryzhkov, A. V., T. J. Schuur, D. W. Burgess, P. L. Heinselman, S. E. Giangrande, and D. S. Zrníc, 2005b: The joint polarization experiment: Polarimetric rainfall measurements and hydrometeor classification. *Bulletin of the American Meteorological Society*, **86** (6), 809–824, doi:10.1175/BAMS-86-6-809.
- Ryzhkov, A. V., T. J. Schuur, D. W. Burgess, P. L. Heinselman, S. E. Giangrande, and D. S. Zrníc, 2005c: The Joint Polarization Experiment: Polarimetric rainfall measurements and hydrometeor classification. *Bull. Amer. Meteor. Soc.*, **86**, 809–824, doi:10.1175/BAMS-86-6-809.
- Ryzhkov, A. V., V. B. Zhuravlyov, and N. A. Rybakova, 1994: Preliminary results of x-band polarization radar studies of clouds and precipitation. *J. Atmos. Oceanic Technol.*, **11**, 132–139.
- Scharfenberg, K. a., and Coauthors, 2005: The Joint Polarization Experiment: Polarimetric radar in forecasting and warning decision making. *Wea. Forecasting*, **20** (5), 775–788, doi:10.1175/WAF881.1.
- Schumacher, C., and R. A. Houze, 2003: Stratiform rain in the tropics as seen by the TRMM Precipitation Radar. *J. Clim.*, **16**, 1739–1756.

- Schumacher, C., R. a. Houze, and I. Kraucunas, 2004: The tropical dynamical response to latent heating estimates derived from the TRMM precipitation radar. *J. Atmos. Sci.*, **61**, 1341–1358, doi:10.1175/1520-0469(2004)061;1341:TTDRTL;2.0.CO;2.
- Schumacher, C., S. N. Stevenson, and C. R. Williams, 2015: Vertical motions of the tropical convective cloud spectrum over Darwin, Australia. *Q. J. R. Meteorol. Soc.*, **141**, 2277–2288.
- Schwartz, C. S., and Coauthors, 2009: Next-Day Convection-Allowing WRF Model Guidance: A Second Look at 2-km versus 4-km Grid Spacing. *Monthly Weather Review*, **137** (10), 3351–3372, doi:10.1175/2009MWR2924.1.
- Siebesma, A. P., and J. W. M. Cuijpers, 1995: Evaluation of parametric assumptions for shallow cumulus convection. *Journal of the Atmospheric Sciences*, **52** (6), 650–666, doi:10.1175/1520-0469(1995)052;0650:EOPAFS;2.0.CO;2.
- Sigmond, M. J., and P. C. Siegmund, 2000: Stratosphere-troposphere exchange in an extratropical cyclone, calculated with a lagrangian method. *Ann. Geophys.*, **18**, 573–582.
- Silverman, F., 1979: Asthma and respiratory irritants (ozone). *Environmental Health Perspectives*, **29**, 131–136.
- Skamarock, W., and Coauthors, 2008: A Description of the Advanced Research WRF Version 3. *Tech. Note NCAR/TN-475+STR*, 113, doi:10.5065/D6DZ069T.
- Snyder, J. C., A. V. Ryzhkov, M. R. Kumjian, A. P. Khain, and J. Picca, 2015: A  $Z_{DR}$  column detection algorithm to examine convective storm updrafts. *Wea. Forecasting*, **30**, 1819–1844, doi:10.1175/WAF-D-15-0068.1.

- Solomon, D. L., K. P. Bowman, and C. R. Homeyer, 2016: Tropopause-penetrating convection from three-dimensional gridded nexrad data. *Journal of Applied Meteorology and Climatology*, **55** (2), 465–478, doi:10.1175/JAMC-D-15-0190.1.
- Squires, P., 1958: The spatial variation of liquid water and droplet concentration in cumuli. *Tellus*, **10** (3), 372–380, doi:10.1111/j.2153-3490.1958.tb02024.x.
- Srinivasan, A. M., S. V. B. Rao, and R. Suresh, 2014: Investigation of convectively generated gravity wave characteristics and generation mechanisms during the passage of thunderstorm and squall line over Gadanki (13.5 N, 79.2 E). *Ann. Geophys.*, **32** (2007), 57–68, doi:10.5194/angeo-32-57-2014.
- Starzec, M., C. R. Homeyer, and G. L. Mullendore, 2017: Storm labeling in three dimensions (SL3D): A volumetric radar echo and dual-polarization updraft classification algorithm. *Monthly Weather Review*, **145** (3), 1127–1145, doi:10.1175/MWR-D-16-0089.1.
- Starzec, M., G. L. Mullendore, and P. A. Kucera, 2018: Using radar reflectivity to evaluate the vertical structure of forecasted convection. *Journal of Applied Meteorology and Climatology*, Accepted.
- Steiner, M., R. A. Houze, and S. E. Yuter, 1995: Climatological characterization of three-dimensional storm structure from operational radar and rain gauge data. *J. Appl. Meteor.*, **34** (9), 1978–2007, doi:10.1175/1520-0450(1995)034<1978:CCOTDS>2.0.CO;2.
- Steiner, M., and J. A. Smith, 2002: Use of three-dimensional reflectivity structure for automated detection and removal of nonprecipitating echoes in radar data. *Journal of Atmospheric and Oceanic Technology*, **19** (5), 673–686, doi:10.1175/1520-0426(2002)019<0673:UOTDRS>2.0.CO;2.

- Stirling, A. J., and R. A. Stratton, 2011: Entrainment processes in the diurnal cycle of deep convection over land. *Quarterly Journal of the Royal Meteorological Society*, **138 (666)**, 1135–1149, doi:10.1002/qj.1868.
- Stohl, A., and Coauthors, 2003: Stratosphere-troposphere exchange: A review, and what we have learned from staccato. *Journal of Geophysical Research: Atmospheres*, **108 (D12)**, 1–15, doi:10.1029/2002JD002490.
- Straka, J. M., D. S. Zrnić, and A. V. Ryzhkov, 2000: Bulk hydrometeor classification and quantification using polarimetric radar data: Synthesis of relations. *J. App. Met.*, **39**, 1341–1372.
- Ström, J., H. Fischer, J. Lelieveld, and F. Schröder, 1999: In situ measurements of microphysical properties and trace gases in two cumulonimbus anvils over western europe. *Journal of Geophysical Research: Atmospheres*, **104 (D10)**, 12 221–12 226, doi:10.1029/1999JD900188.
- Takahashi, H., and Z. Luo, 2012: Where is the level of neutral buoyancy for deep convection? *Geophys. Res. Lett.*, **39 (15)**, doi:10.1029/2012GL052638.
- Takahashi, H., Z. J. Luo, and G. L. Stephens, 2017: Level of neutral buoyancy, deep convective outflow, and convective core: New perspectives based on 5years of cloudsat data. *Journal of Geophysical Research: Atmospheres*, **122 (5)**, 2958–2969, doi:10.1002/2016JD025969.
- Tang, L., J. Zhang, C. Langston, J. Krause, K. Howard, and V. Lakshmanan, 2014: A Physically Based PrecipitationNonprecipitation Radar Echo Classifier Using Polarimetric and Environmental Data in a Real-Time National System. *Weather and Forecasting*, **29 (5)**, 1106–1119, doi:10.1175/WAF-D-13-00072.1.

- Tao, W.-K., S. Lang, J. Simpson, and R. Adler, 1993: Retrieval algorithms for estimating the vertical profiles of latent heat release: Their applications for TRMM. *J. Meteor. Soc. Japan*, **71**, 685–700.
- Tao, W.-K., and Coauthors, 2001: Retrieved vertical profiles of latent heat release using TRMM rainfall products for February 1988. *J. Appl. Meteor.*, **40**, 957–982.
- Thompson, A. M., W.-K. Tao, K. E. Pickering, J. R. Scala, and J. Simpson, 1997: Tropical deep convection and ozone formation. *Bulletin of the American Meteorological Society*, **78** (6), 1043–1054, doi:10.1175/1520-0477(1997)078<1043:TDCAOF>2.0.CO;2.
- Thompson, A. M., and Coauthors, 1994: Convective transport over the central united states and its role in regional co and ozone budgets. *Journal of Geophysical Research: Atmospheres*, **99** (D9), 18 703–18 711, doi:10.1029/94JD01244.
- Thompson, G., P. R. Field, R. M. Rasmussen, and W. D. Hall, 2008: Explicit Forecasts of Winter Precipitation Using an Improved Bulk Microphysics Scheme. Part II: Implementation of a New Snow Parameterization. *Monthly Weather Review*, **136** (12), 5095–5115, doi:10.1175/2008MWR2387.1, 0402594v3.
- Thompson, G., R. M. Rasmussen, and K. Manning, 2004: Explicit Forecasts of Winter Precipitation Using an Improved Bulk Microphysics Scheme. Part I: Description and Sensitivity Analysis. *Monthly Weather Review*, **132** (2), 519–542, doi: 10.1175/1520-0493(2004)132<0519:EFOWPU>2.0.CO;2, 0402594v3.
- Tost, H., P. Jöckel, and J. Lelieveld, 2006: Influence of different convection parameterisations in a gcm. *Atmospheric Chemistry and Physics*, **6** (12), 5475–5493, doi:10.5194/acp-6-5475-2006.



- Ushio, T., S. J. Heckman, D. J. Boccippio, H. J. Christian, and Z.-I. Kawasaki, 2001: A survey of thunderstorm flash rates compared to cloud top height using TRMM satellite data. *Journal of Geophysical Research: Atmospheres*, **106 (D20)**, 24 089–24 095, doi:10.1029/2001JD900233.
- van Lier-Walqui, M., and Coauthors, 2015: On polarimetric radar signatures of deep convection for model evaluation: Columns of specific differential phase observed during MC3E. *Mon. Wea. Rev.*, In Press, doi:10.1175/MWR-D-15-0100.1.
- Van Weverberg, K., N. P. M. van Lipzig, and L. Delobbe, 2011: Evaluation of moist processes during intense precipitation in km-scale NWP models using remote sensing and in-situ data: Impact of microphysics size distribution assumptions. *Atmospheric Research*, **99 (1)**, 15–38, doi:10.1016/j.atmosres.2010.08.017.
- Varble, A., and Coauthors, 2014: Evaluation of cloud-resolving and limited area model intercomparison simulations using TWP-ICE observations: 1. deep convective updraft properties. *J. Geophys. Res. Atmos.*, **119**, 13,891–13,918, doi:10.1002/2013JD021371.
- Wagner, T. J., D. D. Turner, L. K. Berg, and S. K. Krueger, 2013: Ground-based remote retrievals of cumulus entrainment rates. *Journal of Atmospheric and Oceanic Technology*, **30 (7)**, 1460–1471, doi:10.1175/JTECH-D-12-00187.1.
- Wang, P. K., 2003: Moisture plumes above thunderstorm anvils and their contributions to cross-tropopause transport of water vapor in midlatitudes. *Journal of Geophysical Research: Atmospheres*, **108 (D6)**, doi:10.1029/2002JD002581.
- Waugh, D. W., 1996: Seasonal variation of isentropic transport out of the tropical stratosphere. *Journal of Geophysical Research*, **101**, 4007–4023.

- Weisman, M. L., C. Davis, W. Wang, K. W. Manning, and J. B. Klemp, 2008: Experiences with 036-h Explicit Convective Forecasts with the WRF-ARW Model. *Weather and Forecasting*, **23** (3), 407–437, doi:10.1175/2007WAF2007005.1.
- Williams, C. R., and W. Ecklund, 1995: Classification of precipitating clouds in the tropics using 915-MHz wind profilers. *J. Atmos. Oceanic Technol.*, **12**, 996–1012, doi:10.1175/1520-0426(1995)012<0996:COPCIT>2.0.CO;2.
- Winterrath, T., T. P. Kuros, A. Richter, and J. P. Burrows, 1999: Enhanced  $\text{O}_3$  and  $\text{NO}_2$  in thunderstorm clouds: Convection or production? *Geophysical Research Letters*, **26** (9), 1291–1294, doi:10.1029/1999GL900243.
- Yang, G.-Y., and J. Slingo, 2001: The diurnal cycle in the tropics. *Monthly Weather Review*, **129** (4), 784–801, doi:10.1175/1520-0493(2001)129<0784:TDCITT>2.0.CO;2.
- Yang, Y., X. Chen, and Y. Qi, 2013: Classification of convective/stratiform echoes in radar reflectivity observations using a fuzzy logic algorithm. *J. Geophys. Res.*, **118** (4), 1896–1905, doi:10.1002/jgrd.50214.
- Yang, Y. H., and P. King, 2010: Investigating the Potential of Using Radar Echo Reflectivity to Nowcast Cloud-to-Ground Lightning Initiation over Southern Ontario. *Weather and Forecasting*, **25** (4), 1235–1248, doi:10.1175/2010WAF2222387.1.
- Yeo, K., and D. M. Romps, 2013: Measurement of convective entrainment using lagrangian particles. *Journal of the Atmospheric Sciences*, **70** (1), 266–277, doi:10.1175/JAS-D-12-0144.1.
- Yuter, S. E., and R. A. Houze, 1995: Three-Dimensional Kinematic and Microphysical Evolution of Florida Cumulonimbus. Part II: Frequency Distributions of Vertical

- Velocity, Reflectivity, and Differential Reflectivity. *Monthly Weather Review*, **123**, 1941–1963, doi:10.1175/1520-0493(1995)123;1941:TDKAME;2.0.CO;2.
- Zachariasse, M., H. G. J. Smit, P. F. J. Velthoven, and H. Kelder, 2001: Cross-tropopause and interhemispheric transports into the tropical free troposphere over the indian ocean. *Journal of Geophysical Research: Atmospheres*, **106 (D22)**, 28 441–28 452, doi:10.1029/2001JD900061.
- Zhang, K., H. Wan, M. Zhang, and B. Wang, 2008: Evaluation of the atmospheric transport in a gcm using radon measurements: sensitivity to cumulus convection parameterization. *Atmospheric Chemistry and Physics*, **8 (10)**, 2811–2832, doi:10.5194/acp-8-2811-2008.
- Zhang, M., S. Klein, D. Randall, R. Cederwall, and A. Del Genio, 2005: Introduction to special section on toward reducing cloud-climate uncertainties in atmospheric general circulation models. *Journal of Geophysical Research: Atmospheres*, **110 (D15)**, doi:10.1029/2005JD005923.
- Zhao, M., 2014: An investigation of the connections among convection, clouds, and climate sensitivity in a global climate model. *Journal of Climate*, **27 (5)**, 1845–1862, doi:10.1175/JCLI-D-13-00145.1.
- Zhao, M., and P. H. Austin, 2005: Life cycle of numerically simulated shallow cumulus clouds. part ii: Mixing dynamics. *Journal of the Atmospheric Sciences*, **62 (5)**, 1291–1310, doi:10.1175/JAS3415.1.
- Zrnić, D. S., A. Ryzhkov, J. Straka, Y. Lui, and J. Vivekanandan, 2001: Testing a procedure for automatic classification of hydrometeor types. *J. Atmos. Oceanic Technol.*, **18 (1993)**, 892–913, doi:10.1175/1520-0426(2001)018;0892:TAPFAC;2.0.CO;2.

Zrnić, D. S., and A. V. Ryzhkov, 1999: Polarimetry for weather surveillance radars.  
*Bull. Amer. Meteor. Soc.*, **80**, 389–406.